

MASARYKOVA UNIVERZITA
PŘÍRODOVĚDECKÁ FAKULTA
ÚSTAV TEORETICKÉ FYZIKY A ASTROFYZIKY

Diplomová práce

BRNO 2025

ALENA MRKVIČKOVÁ

MASARYKOVA
UNIVERZITA
PŘÍRODOVĚDECKÁ FAKULTA
ÚSTAV TEORETICKÉ FYZIKY A ASTROFYZIKY

Vyhledávání tranzientů s potenciálním využitím družice QUVIK

Diplomová práce

Alena Mrkvičková

Vedoucí práce: Mgr. Ing. arch. Petr Kurfürst, Ph.D.

Brno 2025

Bibliografický záznam

Autor: Bc. Alena Mrkvičková
Přírodovědecká fakulta, Masarykova univerzita
Ústav teoretické fyziky a astrofyziky

Název práce: Vyhledávání tranzientů s potenciálním využitím družice QUVIK

Studijní program: Fyzika

Studijní obor: Astrofyzika

Vedoucí práce: Mgr. Ing. arch. Petr Kurfürst, Ph.D.

Akademický rok: 2024/2025

Počet stran: xiv + 87

Klíčová slova: Astronomické tranzienty; supernovy; fotometrie; světelná křivka; hydrodynamické modelování.

Bibliographic Entry

Author: Bc. Alena Mrkvičková
Faculty of Science, Masaryk University
Department of Theoretical Physics and Astrophysics

Title of Thesis: Transient search with potential use of the QUVIK satellite

Degree Programme: Physics

Field of Study: Astrophysics

Supervisor: Mgr. Ing. arch. Petr Kurfürst, Ph.D.

Academic Year: 2024/2025

Number of Pages: xiv + 87

Keywords: Astronomical transients; supernovae; photometry; light curve; hydrodynamical modelling.

Abstrakt

Práce se zaměřuje na specifické astronomické tranzienty - výbuchy supernov. Teoretická část se zabývá klasifikací supernov a především rozebírá fotometrická specifika jejich světelných křivek napříč nejznámějšími typy. Teoretická část je zakončena přehledem dvou pozorovatelských nástrojů k pozorování supernov a obecně tranzientů. Jedním nástrojem je současná přehlídka - Zwicky transient facility a druhým je budoucí vesmírný dalekohled QUVIK. Praktická část práce se zabývá světelnými křivkami supernov a je rozdělena do dvou částí - pozorovatelské a modelovací. Výsledkem jsou fotometrická pozorování osmi supernov typu Ia, Iax, Ic a II z přelomu roku 2024 a 2025 a odhad jejich parametrů na základě modelování jejich světelných křivek.

Abstract

The work focuses on the specific astronomical transients - supernova explosions. In the theoretical part we deal with the classification of supernovae and especially discuss the photometric specifics of their light curves across the most known types. The theoretical part concludes with an overview of two observational tools for observing supernovae and transients in general. One instrument is the current survey, the Zwicky transient facility, and the other is the future QUVIK space telescope. The practical part of the thesis deals with supernova light curves and is divided into two parts - observational and modelling. As a result, we present photometric observations of eight supernovae type Ia, Iax, Ic and II from the turn of 2024 and 2025 and estimation of their parameters based on modelling of their light curves.

ZADÁNÍ
DIPLOMOVÉ PRÁCE

Akademický rok: 2024/2025

Ústav: Ústav teoretické fyziky a astrofyziky

Studentka: Bc. Alena Mrkvičková

Program: Fyzika

Specializace: Astrofyzika

Ředitel ústavu PŘF MU Vám ve smyslu Studijního a zkušebního řádu MU určuje diplomovou práci s názvem:

Název práce: Vyhledávání tranzientů s potenciálním využitím družice QUVIK

Název práce anglicky: Transient search with potential use of the QUVIK satellite

Jazyk práce: angličtina**Oficiální zadání:**

Astronomical transients are among the most interesting and spectacular phenomena in the universe, which, moreover, because of their vigor and energy yield, reveal to us an extraordinary amount about its nature, at least in the broader vicinity of the observed event. These phenomena include, in particular (mostly in the deep sky), classical novae, supernovae (SNe), kilonovae (KNe), gamma-ray bursts (GRB), tidal disruption events (TDE), etc. The thesis will identify and evaluate these events using the current state-of-the-art observational data, focusing on the potential observations of such phenomena using the upcoming QUVIK satellite.

Vedoucí práce: Mgr. Ing. arch. Petr Kurfürst, Ph.D.

Konzultant: Mgr. Filip Hroch, Ph.D.
Mgr. Filip Münz, PhD.
prof. Mgr. Norbert Werner, Ph.D.
RNDr. Jakub Řípa, Ph.D.

Datum zadání práce: 16. 12. 2023

V Brně dne: 23. 1. 2025

Zadání bylo schváleno prostřednictvím IS MU.

Bc. Alena Mrkvičková, 16. 12. 2023

Mgr. Ing. arch. Petr Kurfürst, Ph.D., 20. 12. 2023

Mgr. Dušan Hemzal, Ph.D., 21. 12. 2023

Poděkování

V první řadě bych chtěla poděkovat vedoucímu mé diplomové práce, panu Kurfürstovi, za jeho čas, trpělivé konzultace, všechny předané znalosti a schované smajlíky v Overleafu :-). Spolupozorovatelce Veronice děkuji za společnou víru a trpělivost nejen při ostření. Děkuji také Emě, Jitce, Vaškovi, Michalovi, Karolíně, Žofii a oběma Mariím.

V neposlední řadě děkuji crabovi za výpočetní čas. Práci věnuji Rafaelovi, necht' je mu motivací ke správnému převodu jednotek.

Prohlášení

Tímto prohlašuji, že jsem svou diplomovou práci vypracovala samostatně pod vedením vedoucího práce a výhradně s využitím informačních zdrojů, které jsou v práci citovány.

Brno 5. května 2025

.....
Alena Mrkvičková

Contents

Introduction	1
Chapter 1. Astronomical Transients	3
1.1 Classical novae	3
1.2 Supernovae	4
1.3 Gamma-Ray Bursts	5
1.3.1 Short GRBs	5
1.3.2 Long GRBs	6
Chapter 2. Supernovae and their Light Curves	7
2.1 Classification of the Supernovae	7
2.1.1 SN Type Ia	8
2.1.2 Core-collapse SNe	10
2.2 SNe Light Curves	13
2.2.1 Light Curves of SN Type Ia	13
2.2.2 Light Curves of SN Type Ib/c	16
2.2.3 Light Curves of SN Type II	17
Chapter 3. QUVIK satellite	19
Chapter 4. The Zwicky Transient Facility	21
Chapter 5. SEDONA	23
5.1 3D Monte Carlo Radiative Transfer Code	23
5.2 Generating Synthetic Light Curves	24
Chapter 6. Photometric Analysis of Supernovae	27
6.1 Measurement and Post-Processing Overview	27
6.2 Observations of SN Lightcurves	28
6.2.1 SN2024vfo	28
6.2.2 SN2024xqe	29
6.2.3 SN2024vim	30
6.2.4 SN2024aecx	30
6.2.5 SN2024aeec	30
6.2.6 SN2025dr	30

6.2.7 SN2025oq	31
6.2.8 SN2025qe	31
6.3 Distance Modulus and Galactic Extinction	41
Chapter 7. Modelling of Supernova Light Curves	43
7.1 SN Type Ia	43
7.1.1 SN Ia models for examining the effect of model parameters on light curves	44
7.1.2 SN2024vim and SN2024xqe	53
7.1.3 SN2025dr	53
7.1.4 SN2025qe	53
7.2 SNe Type Ic	54
7.2.1 SN2025oq	55
7.2.2 SN2024aecx	55
7.3 SN Type II with circumstellar medium	55
7.3.1 SN2024vfo	58
Chapter 8. Conclusions	73
Chapter 9. Appendix	75
9.0.1 SN Ic model	75
Bibliography	79

Introduction

Astronomical transients are important carriers of sudden changes in the universe. Historically, for example, the discovery of Tycho's supernova in 1572 upset the ancient Aristotelian dogma of the immutability of the realm of fixed stars.

The momentum that a supernova (SN) explosion brings to the surrounding universe is invaluable; SNe, by triggering the star formation process, drive future generations of stars. Moreover, supernova nucleosynthesis chemically enriches their host galaxies with many heavy elements, roughly speaking, from oxygen to rubidium. The top half of the periodic table of elements would not exist without kilonovae (KNe), i.e., the neutron star mergers, which, however, are themselves the products of SNe.

Heavy elements, formed as a result of the transients, are essential for the formation of planets and consequently in the evolution of life.

Observations and subsequent studies of astronomical transients are significant domains of modern astrophysics. The main currently ongoing systematic surveys of transients are Zwicky Transient Facility (ZTF) and All-Sky Automated Surveys for SuperNovae (ASAS-SN).

This thesis focuses mainly on SNe and their light curves. The first practical part demonstrates our own systematic observations of eight selected SNe over a period of six months. Photometry of these SNe results in dozens of light curve points that can complement data from large observational campaigns such as ZTF and ASAS-SN. The second practical half deals with modelling of SN lightcurves in the Monte-Carlo (MC) radiative-transfer (RT) code SEDONA. For the eight SNe, we compared the measured light curves with an appropriate model to estimate the parameters of the SN and its closer or more distant surroundings (interstellar or intergalactic extinction in its direction), including some characteristics of their progenitor stars.

Chapter 1

Astronomical Transients

In astronomy, we understand transients as sudden, powerful, and mostly deep-sky events. They change their brightness in a relatively short time, their duration can range from fractions of a second to months or even years. These events are typically associated with a complete or partial destruction of an astrophysical object. Transient events are a source of significant amounts of energy, emitting radiation across the electromagnetic spectrum and sometimes generating gravitational waves. We can observe them in our Galaxy (most of novae and, rarely, SNe), but most are extragalactic, having occurred in the distant past of faraway galaxies.

To summarize this phenomenon: The events that we classify as astronomical transients include novae, SNe, KNe, hypernovae or collapsars, gamma-ray bursts (GRB), tidal disruption events (TDE), and some others, such as giant irregular bursts associated with galactic core events, giant pre-collapse stellar eruptions or outbursts, and so on. We do not include regular variable stars, our solar-system events like solar activities or comets, and near-Earth phenomena such as bright bolides and other small-scale events.

1.1 Classical novae

The name *nova* comes from Latin, where "*stella nova*" means "*new star*". A nova is the most frequent transient phenomenon in which only the outer envelope of a white dwarf is ejected. The evolution of a nova develops in a close binary star system consisting of a donor star (which may be a main-sequence (MS) star or a red giant (RG), for example) and a white dwarf. White dwarfs are considered to be the final evolutionary state of most stars in the universe. They are dense remnants of a stellar core, composed mostly of electron-degenerate matter. Most of them are carbon-oxygen (CO) white dwarfs [42].

The physical process within the classical nova is in a nutshell as follows: The donor star in the binary system ages and expands, and when it overflows its Roche lobe, it starts to transfer its matter (mostly hydrogen) to the white dwarf. Because the white dwarf consists of electron-degenerate material, the volume of the star, including the envelope of accreted hydrogen, does not increase but decreases with increasing mass, so the temperature of the surface layer grows. When this surface

hydrogen layer reaches a temperature about 2×10^7 K, it initiates the rapid nuclear burning of the complete hydrogen envelope via the CNO cycle. In most cases, this hydrogen burning is thermally unstable. This process releases lots of energy, ejects remaining hydrogen away from the surface of a white dwarf, and produces a bright burst of light [42].

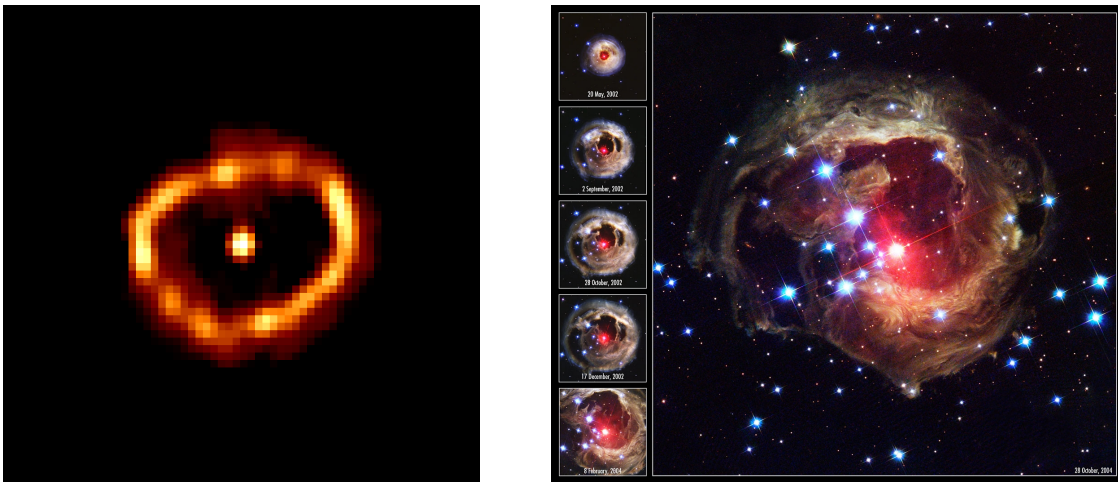


Figure 1.1: (*left*) Nova in the Cygni constellation called V1974 Cyg, captured with HST in 1994 [6]. It was discovered visually on February 1992 by Peter Collins, amateur astronomer. (*right*) V838 Monocerotis, also known as Nova Monocerotis 2002, reached a maximum visual magnitude of 6.75 on February 6, 2002. This nova is referred to as a red nova, which is thought to be caused by the merger of two main sequence stars [57] [58].

Classical novae are the most frequent type of transients seen in a typical galaxy. Observed rates are 26 ± 5 novae per year for the Milky Way. This Galactic nova rate is estimated by analyzing observations from 2019 to 2021 from ASAS-SN [79]. The 20-year period (1995–2016) study [80] estimates a nova rate of 40^{+5}_{-4} novae per year in M31. The spatial distribution analysis indicates that novae in M31 closely follow the galaxy’s bulge light.

1.2 Supernovae

A supernova is a powerful and luminous explosion of a star. SNe are important in two main aspects; they chemically enrich their host galaxies and drive formation of future generations of stars.

There are two basic types of supernova according to the physical nature of the process; thermonuclear SN and core-collapse SN. Historic, observational spectral classification follows presence of spectral lines of mainly hydrogen, helium and silicon, while especially the hydrogen presence defines the classification of SNe as types I (no hydrogen lines in spectra) and II (hydrogen lines are present) [40].

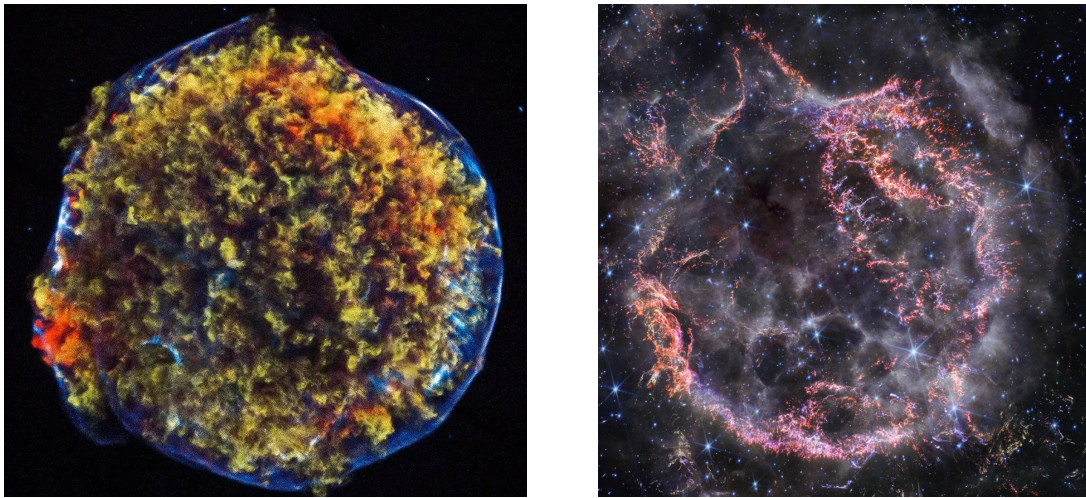


Figure 1.2: (*left*) Tycho's supernova (SN 1572) remnant in Cassiopeia constellation. X-rays observations from Chandra satellite [55]. (*right*) The remnant of the Cassiopeia A supernova explosion in the infrared. The image was obtained by the James Webb Space Telescope [56].

1.3 Gamma-Ray Bursts

Gamma-ray bursts (GRBs) were first detected in 1967 by the VELA satellite, which was designed to monitor compliance with a nuclear test ban treaty concluded in 1963 between the USA and the Soviet Union that prohibited atomic bomb tests underwater, in the atmosphere, and in space. GRBs are the brightest explosions since the Big Bang, generating approximately 10^{51} ergs of energy, or even more, in just a few seconds, which is at least comparable to the energy released in a "standard" supernova explosion.

The duration of GRBs is measured by a metric called T_{90} parameter, which represents the time it takes for the total recorded signal to rise from 5% to 95%, covering 90% of the total observed energy. Proper investigation has shown that the duration distribution of GRBs displays a bimodal pattern. Generally, shorter bursts tend to be more intense than longer ones, indicating that this distinction is likely due to a physical cause rather than just a bias in observation [41].

Due to their extreme brightness, GRBs are visible from even very distant galaxies, but they are very rare events in individual galaxies. The paper [81] conclude that the mean rate in the Milky Way is approximately 5.5×10^{-7} per year, or one GRB every 1.8 million years.

1.3.1 Short GRBs

Short GRBs ($T_{90} < 2s$) are predominantly associated with neutron star mergers. The result of mergers of binary neutron stars (BNS) is the ejection of a substantial amount of neutron-rich material, in which heavy elements with $Z > 26$ are synthesised via the process of rapid neutron capture nucleosynthesis, otherwise known

as the r-process. The radioactive decay of the newly produced material results in a transient source known as a *kilonova* [64].

1.3.2 Long GRBs

Long GRBs ($T_{90} > 2s$) are linked to the collapse of massive stars directly into a black hole, a phenomenon that is also referred to as *hypernovae* or *collapsars*. Connection between long GRBs and SNe is described in Figure 2.5.

The theory of the physical nature of short and long GRBs is significantly observationally supported by the fact that long GRBs almost entirely occur in the star-forming galaxies where the existence of young massive stars is expected, whereas short GRBs occur in all types of galaxies, including the oldest elliptical ones.

Chapter 2

Supernovae and their Light Curves

2.1 Classification of the Supernovae

The main categorisation of SNe from 1941 by Rudolph Minkowski [32] relies on the characteristics of their optical spectra near the maximum luminosity when the ejecta are optically thick. These spectra exhibit Doppler-broadened features generated above the photosphere, with velocities generally around $10\,000\text{ km s}^{-1}$. Spectral features often display P Cygni profiles, which are characterised by emission near the rest wavelengths of the lines, accompanied by blue-shifted absorption that indicates the formation of the lines within an expanding medium.

The occurrence of the Balmer hydrogen spectral lines is the essential distinguishing feature between two major spectroscopic types of SNe. Supernovae Type II show evidence of hydrogen and supernovae Type I do not. The SNe Type I are further sub-categorised to Type Ia, if their spectra show singly-ionized silicon absorption lines (Si II), Type Ib, if they show strong neutral helium lines (He I) and no or weak silicon lines, and finally Type Ic, if they have absent or weak hydrogen, helium, and silicon lines but strong absorption of oxygen (O I) [35].

From the point of view of the physical nature, two model types of SNe can be distinguished, corresponding to two types of stellar death: Thermonuclear SN (Type Ia), thought to be the thermonuclear explosions of accreting white dwarf stars; and core-collapse SN (Types Ib, Ic, II), which occur when the iron core of a massive star collapses to form a neutron star or a black hole.

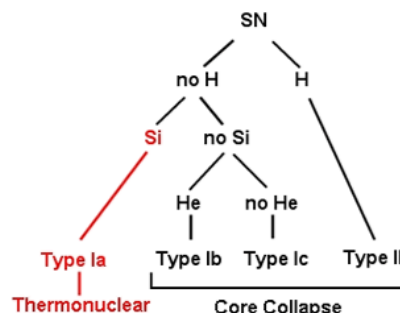


Figure 2.1: Spectral classification tree of the main types of SNe [31].

Among Type II SNe, Barbon et al. (1979) [33] classified these into two photometric subclasses characterized by their light curves: those that exhibit prominent plateaus (Type II-P) and those that decline linearly (Type II-L). Later, two additional spectroscopic subclasses of Type II supernovae were introduced: Type IIb SNe, which transition from hydrogen-rich early spectra to helium-dominated SN Ib-like spectra near their peak [34], and Type IIn SNe, which show strong and relatively narrow emission lines of hydrogen, indicating a dense circumstellar medium (CSM), surrounding the progenitor star before the SN event [36].

Type Ia SNe also show prominent sulphur (S II) absorption lines that are not seen in other SN classes. They have also been sub-divided into more special classes, e.g. Type Ia regular, Iax, Ia-CSM, "super-Chandrasekhar" Ia (mergers of two white dwarfs), and others.

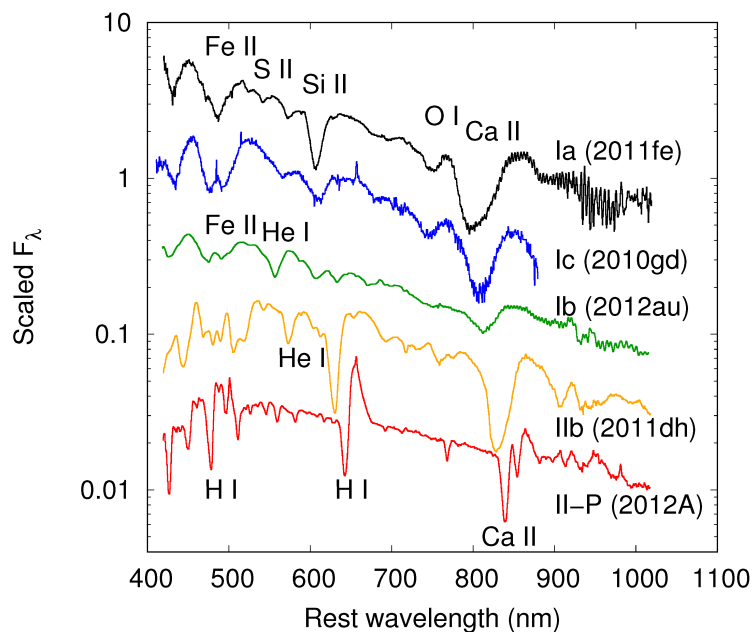


Figure 2.2: Optical spectra of different types of SNe close to maximum light. Prominent spectral features are labeled with their contributing ions. Data were collected at McDonald Observatory, Texas [30].

2.1.1 SN Type Ia

It is theorised that Type Ia SNe are the result of the thermonuclear disruption of a white dwarf that has accreted sufficient amount of matter from a companion star to approach the Chandrasekhar limit of $1.44 M_{\odot}$. During the process of accretion, the white dwarf experiences a contraction to a radius of $\sim 10^8$ cm. The central density increases to $\rho_c \gtrsim 10^9 \text{ g cm}^{-3}$, and the central temperature to $T_c \gtrsim 10^8$ K. At this point, unstable carbon fusion ignites and a nuclear burning front propagates through the white dwarf in approximately 1 second. This releases nuclear energy while synthesising heavier elements, raises the temperature to $T \gtrsim 10^9$ K, and drives the white dwarf into expansion [35].

SNe Ia occur in both spiral and elliptical galaxies. After the thermonuclear explosion, they leave no bound remnant (at least in absolutely most cases, except for some rare events of Type Iax such as the "Parker star" [39]), the white dwarf is completely disintegrated. Their event rate is \sim one in 300 yr in our Galaxy and they produce $\sim 2/3$ of iron in Galaxy [40].

In the proposed progenitor model for Type Ia supernovae, the exploding white dwarf can have either a non-degenerate companion star (known as the single degenerate scenario) or another white dwarf (referred to as the double degenerate scenario). In the single-degenerate model, the white dwarf can accumulate matter from a red giant, sub-giant/main sequence, or a helium star. In contrast, the double degenerate scenario involves the violent merger of two white dwarfs of similar mass (typically $\sim 0.9 M_{\odot}$), which has been demonstrated to result in sub-luminous Type Ia supernova explosions. However, white dwarfs that are more massive, owing to their higher density, will generate larger amount of ^{56}Ni and iron group elements, leading to brighter SNe Ia [44].

Type Ia SNe are employed as standardised candles due to the (almost) identical physical nature and, therefore, expected identical luminosity; they also meet an empirical relationship linking their intrinsic luminosity to their rate of dimming. The dimming behaviour is quantified by the decline in brightness, measured in the B-band, occurring 15 days after peak luminosity. This B-band decline is denoted as $\Delta m_{15}(B)$. The so-called *Phillips relation* [45] reveals that SNe exhibiting smaller values of $\Delta m_{15}(B)$ are intrinsically more luminous than those with larger values. The empirical form of this relation specifies the absolute magnitude at maximum brightness in the B-band as

$$M_{\text{max}}(B) = -21.726 + 2.698 \Delta m_{15}(B). \quad (2.1)$$

This relationship facilitates the determination of an absolute magnitude of an SN once $\Delta m_{15}(B)$ has been measured. In normal Type Ia SNe, the decline rate typically falls within the range $0.85 < \Delta m_{15}(B) < 1.70$ magnitudes [44].

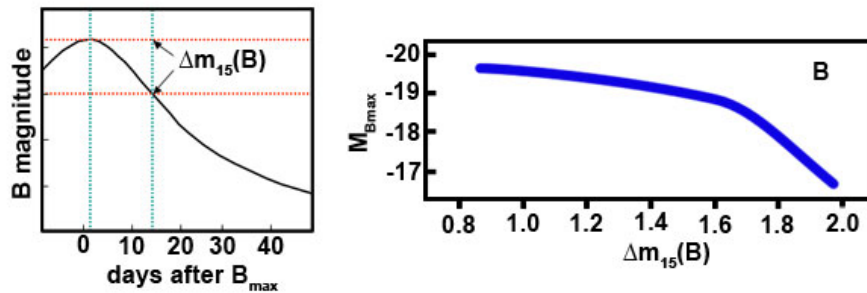


Figure 2.3: The maximum in the B-band is associated with the rate at which the light curve decreases in the 15 days, referred to as $\Delta m_{15}(B)$. Supernovae that are brighter tend to have a slower decline, while those that are fainter decline more quickly. This relationship is recognized as the luminosity-decline rate connection (*Phillips relation*) [47].

By comparing the inferred absolute magnitude with the observed apparent magnitude at peak brightness, it is possible to calculate the distance to the SN. Owing to their exceptional luminosity, we use Type Ia SNe as distance indicators on cosmological scales, beyond the reach of other standard distance measurement techniques [40].

Although the majority of Type Ia SNe follow the luminosity–decline rate relation, it is crucial to recognise that a significant subset of thermonuclear SNe deviate from this trend. The over-luminous (super-Chandrasekhar SNe Ia) occupy the extreme end of the $\Delta m_{15}(B)–M_B$ relation, characterised by their slow decline. In contrast, SNe Iax represent a peculiar subclass of thermonuclear explosions, distinguished by their relatively low luminosities and reduced kinetic energies in comparison to standard SNe Ia [44].

SN Type Iax

Type Iax supernovae (SN Iax), commonly also referred to as SN 2002cx-like SNe, represent a subclass of peculiar white dwarf SNe distinguished by their relatively lower ejecta velocities and luminosities compared to normal type Ia SNe. With over fifty known examples, SN Iax predominantly occur in late-type host galaxies, suggesting a younger stellar population. The only SN Iax for which a pre-explosion progenitor has been identified is SN Iax 2012Z, supporting the prevailing hypothesis that these events may result from an explosion of a carbon-oxygen white dwarf, instigated by helium accretion up to the Chandrasekhar mass. Despite their spectral similarities to normal SN Ia, particularly the “hot” variants, SN Iax are characterised by their expansion velocities, which range from 2 000 to 7 000 km s^{−1}. The possibility of misclassifying SN Iax as normal SN Ia increases with uncertainties in velocity measurements and host galaxy redshifts [37].

2.1.2 Core-collapse SNe

A core-collapse SN explosion occurs when a star rapidly collapses onto a neutron star or a black hole. In very massive stars ($M_\star \gtrsim 8 - 9 M_\odot$), nuclear processes go more rapidly than the removal of their outer layers. This allows the star’s core to evolve to the stage where it synthesizes elements in the iron group (this stage occurs predominantly in stars initially more massive than $\sim 10 M_\odot$, while stars with initial masses in range $\sim 8 - 10 M_\odot$ end their “lives” as the so-called electron-capture (EC) SNe, synthesising only O-Ne-Mg elements [50]). Once the star begins to synthesise iron, it ceases to produce additional nuclear energy within a short period of time. The exhaustion of exothermic reactions within the iron core leads to a rapid contraction of the star. When the mass of the iron core exceeds the Chandrasekhar mass limit ($1.44 M_\odot$), the pressure exerted by the electron-degenerate material is no longer able to resist its own gravity, resulting thus in further gravitational collapse [49].

This process continues until the neutron gas degenerates at densities $\sim 10^{14} - 10^{15}$ g cm^{−3}, resulting in the formation of an extremely dense neutron star. How-

ever, in rare instances where the initial mass of a star exceeds $40 - 50 M_{\odot}$, even neutron-degenerate matter may be unable to resist the gravitational force, resulting in a direct collapse onto a black hole [50] [51] [52].

Core-collapse SNe are found in spiral or irregular galaxies, which, in contrast to elliptical galaxies, are still actively forming new stars. After explosive processes, their cores collapse to compact remnants, that is, neutron stars or black holes. Their event rate is ~ 2 in 100 yr in our Galaxy and they produce $\sim 1/3$ of all the iron and oxygen in Galaxy [40] (this does not mean that all of them were observed in history; many of them exploded in dust-shielded Galactic plane or near the Galactic centre).

The current consensus is that Type Ib/c SNe are associated with the evolution of close binaries or very massive helium or Wolf-Rayet stars. Type II SNe are mostly connected with explosions of red supergiants, sometimes even yellow or blue supergiants. The large hydrogen envelope of red supergiants and the reversely propagating recombination wave within it is the reason for the (aforementioned) plateau in the SNe Type II-P. Table 2.1 shows the simplified connection between progenitor properties and core-collapse SN types [50].

SN Type	Pre-SN Stellar Structure
IIP	$\gtrsim 2 M_{\odot}$ hydrogen envelope
IIL/b	$\lesssim 2 M_{\odot}$ hydrogen envelope
Ib/c	no hydrogen envelope

Table 2.1: Progenitor properties for different core-collapse SNe [50].

The paper by Heger et al. [50] shows clear distribution of SNe types (demonstrated in Figure 2.4) as a function of metallicity and progenitor initial mass. The thick green line indicates where stars retain their hydrogen envelope, while the dashed blue line marks the boundary for direct black hole formation. Type II-P SNe (green hatching) occur in the lower left region; potentially weak and faint SNe due to ^{56}Ni fallback, especially at low metallicity, are then on the right side of the SN II-P region. Near the hydrogen envelope loss edge are Type II-L/b SNe (purple hatching). Above both lines, Type Ib/c SNe occur; they may also be weak due to fallback. In the direct black hole infall regime, normal SNe do not exist, except for the pulsational pair-instability SNe (brown hatching) that explode due to the $\gamma\gamma \rightarrow e^-e^+$ reaction, that is, two gamma photons create at extreme conditions (that are in cores of very massive stars above $\sim 80 - 100 M_{\odot}$) an electron-positron pair that is insufficient to resist gravitational contraction of the star. Unlike the yet more massive non-pulsational pair-instability SNe (red hatching), they are not disintegrated completely; some fraction of the star survives which may later again undergo the SN phase. Another domain forming black holes at low metallicities and high masses (white), where no SNe are produced, is at the lower right corner of the graph, however, so massive stars have to be so rare that these cases are almost hypothetical.

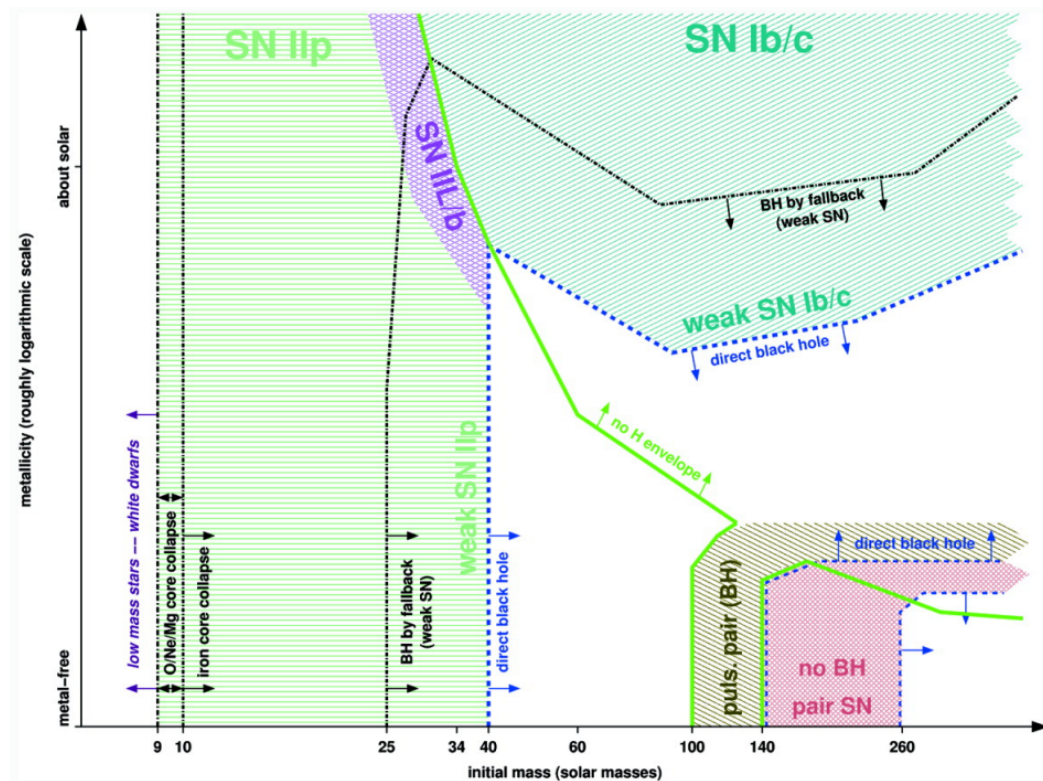


Figure 2.4: SNe types of nonrotating massive single stars as a function of initial mass and initial metallicity. Obviously, both these parameters have significant effect on the various SN-types creation. Adapted from [50].

The additional graphical subdivision in Figure 2.5 shows how different types of collapsars arise from single massive stars, depending on their initial mass and metallicity. The key distinction is between Type II collapsars, which form after fallback (indicated in red; the fallback means the subsequent fall of SN into the black hole after early expansion; we may regard it as an intermediate category between "normal" SNe and direct black hole collapsars), and Type I collapsars, which form directly (shown in violet). They are further categorised into those with a hydrogen envelope (indicated by cross-hatching) that can create jet-powered supernovae (JetSNe), and hydrogen-free collapsars (diagonal cross-hatching) that could lead to either JetSNe or gamma-ray bursts (GRBs). The hydrogen envelope is lost below a certain threshold (thick green line), while direct formation of very massive black holes (Type III collapsars) occurs at high mass and low metallicity. Notably, no collapsars occur in regions of low mass, high metallicity, or the pair-instability SNe zone (shown in white) [50].

Jet-driven supernovae (JetSNe) are highly asymmetric explosions fuelled by bipolar outflows from a central object, making them potentially more energetic than regular SNe and a precursor to hypernovae. Although JetSNe can occur alongside GRBs, not all will generate the highly relativistic ejecta needed for a strongly gamma-radiating burst event [50].

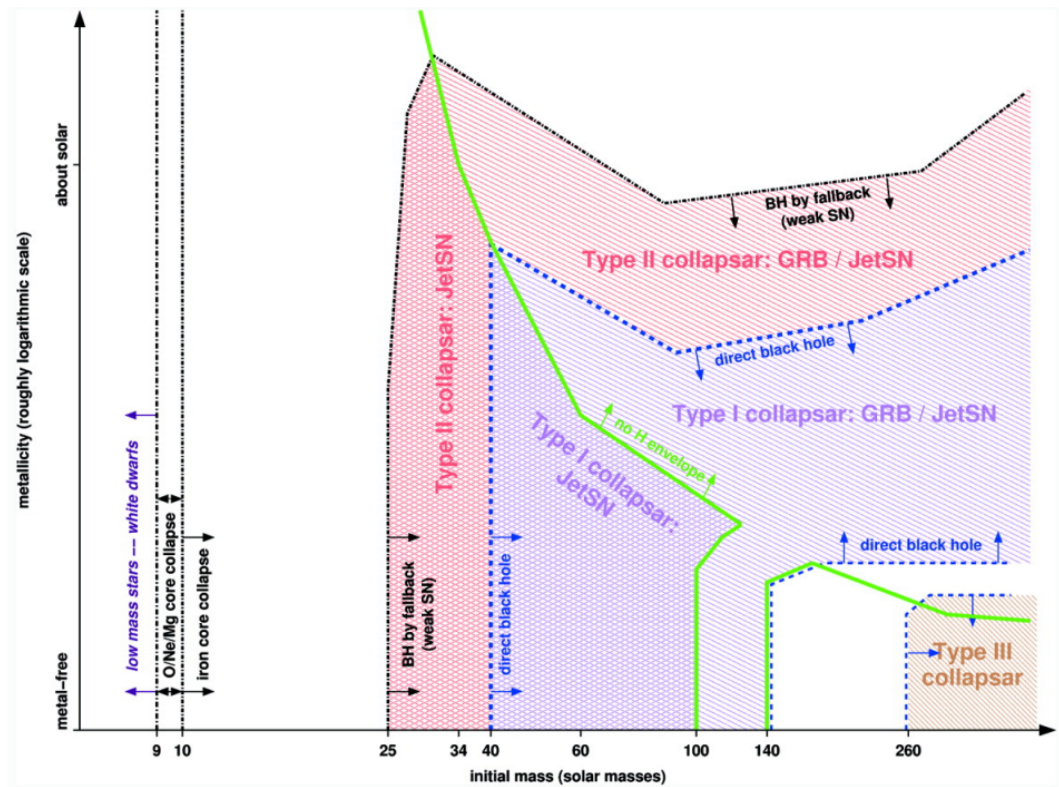


Figure 2.5: Collapsar types resulting from single massive stars as a function of initial mass and metallicity [50].

2.2 SNe Light Curves

Light curves are utilised to constrain fundamental physical quantities, including the total ejected mass, the mass of synthesised unstable ^{56}Ni , the kinetic energy of the ejecta, and the radius of the progenitor star. A bolometric light curve tracks the total luminosity of an SN and is closely linked to the physics of explosion. 'Bolometric' typically refers to integration over all wavelengths, but in the context of SNe, it often means UVOIR, encompassing near-UV, optical, and near-IR, sometimes called "quasi-bolometric". The apparent magnitude at peak brightness can be converted to absolute magnitude by estimating distance and interstellar extinction [35].

Typically, Type Ia and Type II SNe have a $B - V$ colour index around 0.0 near maximum light, which is similar to the colour of a blackbody with a temperature of about 10^4 K. In contrast, Type Ib/c SNe are somewhat redder because their photospheres are cooler. After reaching maximum light, the colors of SNe tend to become redder over time as the ejected matter cools down [35].

2.2.1 Light Curves of SN Type Ia

For a standard SN Ia, one energy source is dominantly responsible for powering the light curve after maximum, that is the radioactive decay of nickel that is pro-

duced at the moment of the $2^{12}\text{C} + 2^{16}\text{O} \rightarrow {}^{56}\text{Ni}$ thermonuclear reaction during the SN explosion. Therefore, the luminosity increases as more ${}^{56}\text{Ni}$ is produced.

The first phase of the light curve is powered by the inverse- β decay of ${}^{56}\text{Ni}$,



with a half-life $\tau_{\text{Ni}} = 6.1$ days. The product ${}^{56}\text{Co}^*$ is an excited state of cobalt that decays down to its ground state by emitting γ -rays that eventually transfer their energy to the stellar plasma. The produced isotope ${}^{56}\text{Co}$ is unstable again and decays with another electron capture to iron,



with a half-life $\tau_{\text{Co}} = 77.7$ days [40].

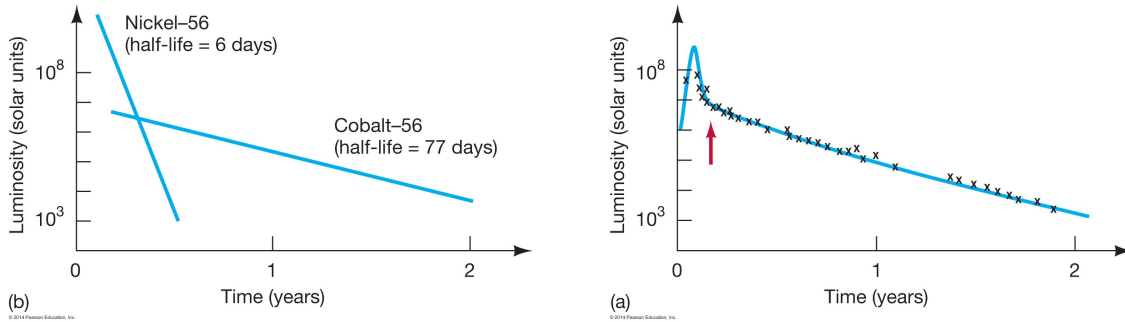


Figure 2.6: Radioactive decay of nickel as the source of the SN Ia light curve [43].

The initial phase of the light curve is characterized by the following physical assumptions: homological expansion and spherical symmetry, the dominance of radiation pressure, a significant presence of the radioactive isotope ${}^{56}\text{Ni}$ in the expanding material, a small initial radius and constant opacity. The well-known *Arnett's law* [48] (Equation 2.6) quantifies this feature; it shows that the peak of the light curve must be close to the instantaneous decay power at that time,

$$L(t) = L(0) \varphi(t) \sim \frac{fE}{\tau_0} \varphi(t), \quad (2.4)$$

where f is numerical factor (ratio of the initial thermal energy $E_{\text{th}}(0)$ to the total energy E ; typically, $f = 0.5$). The dimensionless function $\varphi(t)$ is [48]

$$\varphi(t) \approx e^{-(t/\tau_0 + t^2/\tau_m^2)} \int_0^t \frac{\dot{Q}(t')}{L(0)} e^{(t'/\tau_0 + t'^2/\tau_m^2)} \left(\frac{\tau_h + 2t'}{\tau_m^2} \right) dt', \quad (2.5)$$

where the various timescales τ_0 , τ_h , and τ_m mean the diffusion timescale ($\tau_0 \propto \kappa M/R$ where κ is the opacity), hydrodynamical timescale ($\tau_h = R_*/\langle v \rangle$ where $\langle v \rangle$ is the averaged expansion speed of SN), and their combination ($\tau_m = \sqrt{2\tau_0\tau_h}$), respectively. The quantity \dot{Q} in Equation 2.5 is the heating power; we may in this case regard it as a heating power from radioactive decay.

We may also use the simplified Equation 2.5 for "early time" in the form [48]

$$\frac{d(\ln L)}{dt} = -\frac{4cR}{\kappa M} + \frac{\epsilon_0}{E} \exp\left(-\frac{t}{\tau_{\text{Ni}}}\right) \quad (2.6)$$

to find the time of maximum luminosity. If we approximate $E = \epsilon_0 t$ (where E and ϵ_0 are the energy and the SN power, both per unit mass), then Equation 2.6 is zero at $t \approx 1.25 \tau_{\text{Ni}}$ for the asymptotic velocity of SN $v_* = 10^9 \text{ cm s}^{-1}$, $\kappa = 0.2 \text{ cm}^2 \text{ g}^{-1}$, and $M = 1 M_\odot$. The maximum thus occurs at $t_1 \approx 9.5 \times 10^5 \text{ s} \approx 11 \text{ d}$, when the radius is $R = t_1 v_* \approx 9.5 \times 10^{14} \text{ cm}$.

From the observations, the maximum luminosity $L_{\text{UVOIR}} \gtrsim 10^{43} \text{ erg s}^{-1}$ occurs approximately 20 days after the explosion. Inferred from the blueshift and width of the spectral lines, the velocity at the photosphere (in the early time, we may identify the outer SN expansion front with the photosphere) is estimated to be $v \sim 10\,000 \text{ km s}^{-1}$. The radius of the photosphere when it reaches maximum brightness is calculated from velocity and time to maximum light as $R = vt = 10^{15} \text{ cm}$. To determine the luminosity, we use the formula $\sigma T_{\text{ph}}^4 = L/(4\pi R^2)$, which yields a photosphere temperature of approximately $T_{\text{ph}} \approx 10^4 \text{ K}$ [35].

Light Curves of SN Type Iax

The optical light curves of SN Iax show a general similarity to those of SN Ia but exhibit greater diversity. SN Iax typically experience faster growth (10 to 20 days) in all bands, with notable variations in the pre-maximum light curves [72]. Their decline rates in the B and V bands tend to be faster in general than regular SNe Ia [73]. The optical colour evolution of SN Iax, such as in the $B - V$ colour index, is roughly similar to that of normal SN Ia [71], although SN Iax show significantly slower declines in redder bands [72].

Generally, faster-rising SN Iax also fade more quickly, with some exceptions, such as SN 2007qd [77]. Unlike SN Ia, SN Iax do not show a prominent second peak in the redder and near-infrared bands [76] (red bump). This peak is especially enhanced in slowly declining SNe Ia, which means that those most spectroscopically similar to SNe Iax exhibit different photometric behaviour. Despite this, weeks after maximum brightness, SNe Iax show modest colour evolution, allowing late-time colours to serve as indicators of host-galaxy reddening [71].

The late-time light curves of typical SN Iax decline more slowly than those of regular SN Ia up to about 300 to 400 days after maximum light, after which both types show similar decline rates around 0.01 to 0.02 mag day⁻¹ [75]. The peak optical luminosity of SN Iax ranges significantly from $M_V \approx -19$ for the brightest to $M_V \approx -13$ for the faintest, falling below the Phillips relation 2.1 by 0.5 to several magnitudes [71].

Magee et al. (2016) [72] suggest that peak luminosity may correlate more strongly with rise time than decline rate. In the NIR, SN 2005hk shows a broad peak delayed by about 10 to 15 days relative to the B band. In the near-ultraviolet (NUV) range, SNe Iax evolve more quickly in near-UV than regular SNe Ia, initially appearing bluer but becoming redder (by 1.5 to 2 mag in Swift UVW1) approximately ten days post maximum [78] [37].

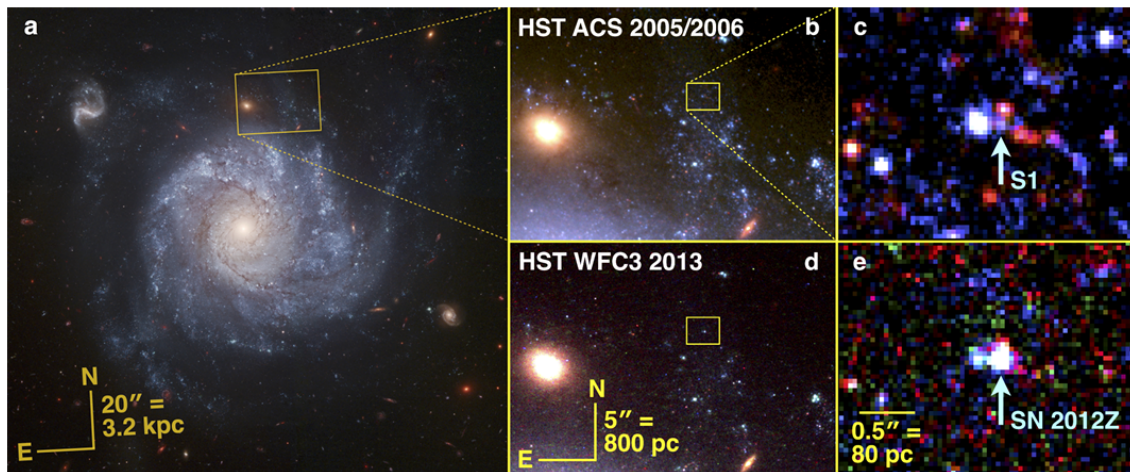


Figure 2.7: A major breakthrough in understanding SNe Iax occurred with the discovery of the progenitor system of SN 2012Z [74], which exploded in the nearby galaxy NGC 1309. This galaxy had extensive deep, multi-epoch HST imaging that covered SN 2012Z’s pre-explosion location. The high-resolution imaging revealed a luminous and blue source identified as a helium-star companion of the exploding white dwarf; this was the first detection of progenitor of a thermonuclear supernova. The left panel of the associated figure shows the deep Hubble Heritage image of NGC1309, while the upper and lower panels depict the progenitor system and its post-explosion position, respectively (adapted from [74] [38] and [37]).

2.2.2 Light Curves of SN Type Ib/c

Massive stars that are the progenitors of core-collapse SNe, which have shed their hydrogen layers (stripped stars) produce these types of SNe. The radii of the stripped envelopes themselves are estimated within the range $0.1 - 1 R_{\odot}$. After a core collapse, a shock wave emerges at the base of the envelope, leading to the heating and ejection of material. Within minutes, the shock wave reaches the progenitor’s photosphere, resulting in an X-ray flash during the breakout phase.

Subsequently to the fireball phase, in the absence of circumstellar interactions, the light curve is supported by the radioactive decay of ^{56}Ni and ^{56}Co , which is analogous to the behaviour of a Type Ia supernova. Although fundamental physical processes are comparable, the light curves of SN Ib/c differ because of variations in ejected masses, kinetic energies, elemental compositions, opacities, and asymmetries. Typically, SN Ib/c exhibit greater asymmetry than SN Ia and have lower metallicities; however, in some cases, SN Ic-BL (broad lines), which are sometimes linked to GRBs, can exhibit higher M_{Ni} and kinetic energies than SNe Ia.

One noteworthy distinction compared to SN Ia is, that over many years, the decay of the long-lived isotope ^{44}Ti (which has a half-life of 60 years) could become important. The decay process of ^{44}Ti leads to the release of hard X-rays and gamma-rays [35].

2.2.3 Light Curves of SN Type II

The question of whether SNe II-P and SNe II-L are physically different or merely two extremes of the same process remains a subject of debate. However, other SNe II, notably SNe IIn, exhibit a more gradual decline. Most SNe II eventually undergo a linear tail phase in magnitude, which typically corresponds closely to the 77-day half-life of $^{56}\text{Co}^*$. In the context of core-collapse SNe, the interaction of SN with the circumstellar medium has been shown to be a significant source of radiation in the UVOIR range [53], also constituting a major source of non-UVOIR radiation.

Light Curves of SN Type IIP

SNe IIP progenitors are believed to be red supergiants, which have massive hydrogen envelopes with mass $\sim 10 M_{\odot}$ and large radii $\sim 100 - 1000 R_{\odot}$. The fireball phase of a SN II-P light curve persists for several weeks until the outer layers cool sufficiently (below 10^4 K) for hydrogen to undergo recombination. As the ejecta expand, the photosphere moves inward with respect to mass, while keeping a nearly constant radius. The temperature stabilizes around the hydrogen recombination temperature, ~ 5500 K, at the relevant electron densities. Consequently, the luminosity remains relatively steady, leading to the formation of a plateau in the light curve. The duration of this plateau, typically around ~ 100 days, is influenced by the mass of the hydrogen envelope, the kinetic energy of the explosion, and the degree of mixing of radioactive ^{56}Ni with respect to the surface. When the recombination front reaches the base of the hydrogen envelope, it enters the inner, metal-rich core material, resulting in a sharp decline in luminosity and signalling the end of the plateau phase.

SNe II-P eject radioactive ^{56}Ni , typically around $0.1 M_{\odot}$, although this can vary widely. During the initial plateau phase, the luminosity from radioactivity is significantly lower than the shock-deposited thermal energy released by the hydrogen recombination front. Following the plateau and plateau-tail phases, the initial shock energy becomes exhausted, but the decay of ^{56}Co continues [35].

Light Curves of SN Type IIb

SNe IIb refer to the explosions of massive stars that have shed the majority of their hydrogen layers, either through stellar winds or interactions in binary systems. SN IIb is considered an intermediate type between SN Type I and Type II. Even a small remaining hydrogen envelope (around 1 solar mass) can result in a considerable radius of the progenitor, allowing the fireball phase to be long enough for observation. Following this initial fireball phase, similar to the case of SNe Ib/c, there is a drop in luminosity that is succeeded by a rise to a secondary peak and a subsequent tail phase. Both the secondary maximum and the tail phase are driven by the decay of $^{56}\text{Co}^*$, much like in SN Ia and SN Ib/c [35].

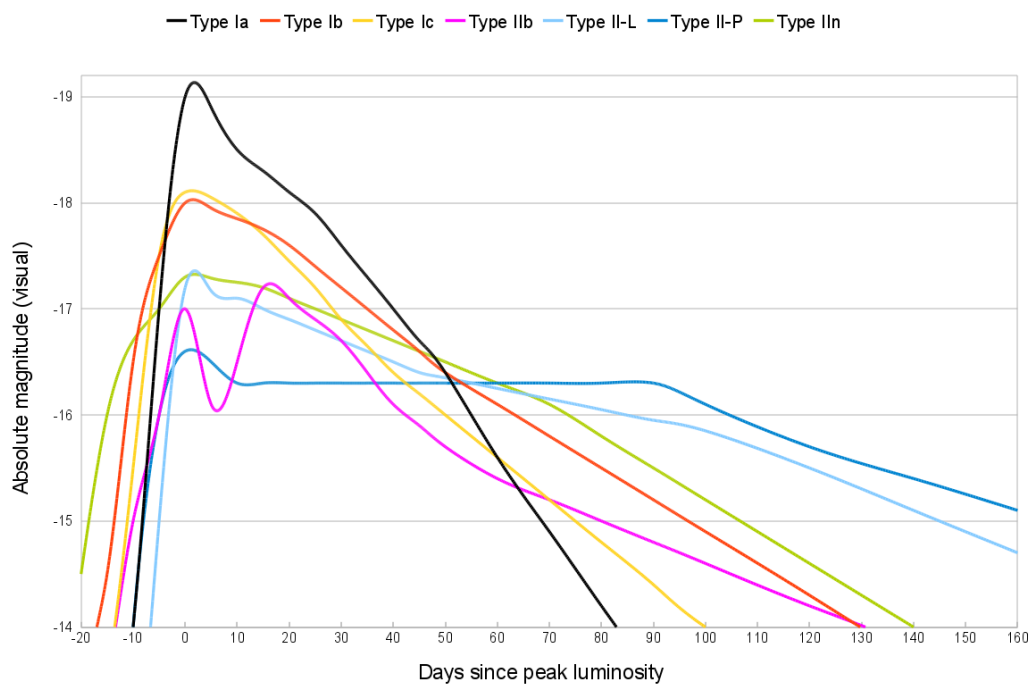


Figure 2.8: Idealised early-to-intermediate phase of light curves of the main "classical" types of SNe [46]. Some more recently classified types, such as the superluminous SNe (SLSNe), are missing.

Chapter 3

QUVIK satellite

The Quick Ultra-Violet Kilonovae Surveyor will be the first Czech space telescope scheduled to be launched in 2027 [59] [60] [61]; its basic orbit is planned to be a sun-synchronous (SSO) low-Earth orbit, with an altitude of 550 km. The basic duration of the QUVIK mission is expected to be 3 years. The telescope will be equipped with an ultraviolet (UV) space telescope and will be attached to a small satellite of approximately 100 kg. The satellite will have a moderately fast re-pointing capability and a real-time alert communication system. Its main goals include monitoring the UV-brightness evolution of KNe as quickly as possible after receiving the gravitational wave signal by one of their detectors (LIGO, VIRGO, and possibly others, if will be already in operation) to distinguish between different models of a KN explosion.

The close coordination of the FUV-capable QUVIK with the alertive support of the Israeli Ultraviolet Transient Astronomy Satellite (ULTRASAT) will therefore lead to a multiplicity of scientific results of both missions [59].

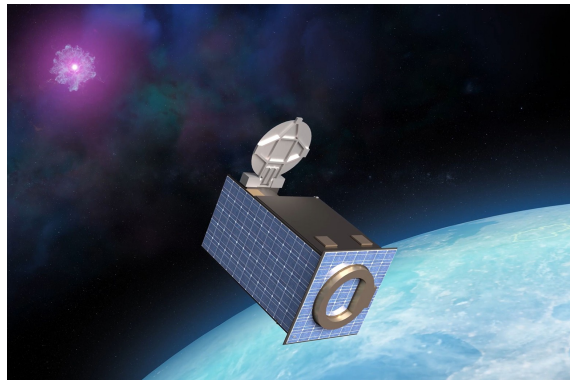


Figure 3.1: Mission logo and artwork of the QUVIK satellite [62] [59].

The instrument will also provide unique follow-up capabilities in both the near- and far-UV bands for other transients, including GRBs, SNe, outbursts in active galactic nuclei, and tidal disruption of stars by supermassive black holes. The field of GRB science stands to benefit significantly from the integration of an onboard GRB detector with the capacity for localisation. In addition to the ob-

servation of transients, the satellite will be directed towards other objects, namely stars and stellar systems, as well as galactic nuclei.

The UV-telescope and detectors

The primary science payloads will consist of a modified Cassegrain telescope with a primary mirror measuring $D = 33$ cm in diameter. This will be imaged by a $4k \times 4k$ complementary metal–oxide–semiconductor (CMOS) sensor. The field-of-views (FoV) of UV light channels will be at least $\text{FoV (NUV)} = 1^\circ \times 1^\circ$ and $\text{FoV (FUV)} = 0.25^\circ \times 0.25^\circ$. As described in [59], the effective area of the UV telescope and detectors is adequate to detect a $m_{AB} = 22$ object with a signal-to-noise ratio 5, using an 18-minute exposure image composed of individual 20-second exposures (m_{AB} is the so-called *effective magnitude*, where the frequency dependent absolute magnitude is defined as $AB_\nu = -2.5 \log f_\nu - 48.60$, where f_ν is the photometric radiative flux per unit frequency [52]).

The image presented in Figure 3.2 is a simulated NUV band QUVIK image of a KN with $m_{AB} = 21$ at an angular distance from its host galaxy of 1.5 effective radii (radius containing half the luminosity of a given galaxy) at a distance of 200 Mpc. QUVIK’s angular resolution will facilitate the clear detection of a KN on the background of its host, unless it occurs in the galaxy’s bright central region.

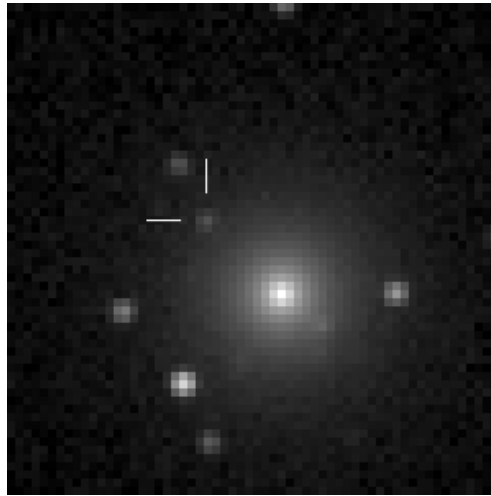


Figure 3.2: A simulated NUV band QUVIK image of an $m_{AB} = 21$ KN (pixel resolution of $1.75 \text{ arcsec px}^{-1}$, FoV cutout of $1.75 \text{ arcmin} \times 1.75 \text{ arcmin}$), assuming the star field and the host galaxy of the famous KN AT2017gfo [59]. This transient resulted from the iconic binary neutron star merger that produced the gravitational wave source GW170817. It was the first simultaneous detection (and unfortunately the last one so far) of gravitational waves and electromagnetic radiation in history [65].

Chapter 4

The Zwicky Transient Facility

The Zwicky Transient Facility (ZTF) is a wide-field optical survey project based at the Palomar Observatory in California, United States [67]. Commissioned in 2018, ZTF is a successor to the Intermediate Palomar Transient Factory (iPTF), which operated from 2009 to 2017. The facility is named after the Swiss astronomer Fritz Zwicky, a pioneer in the study of SNe and dark matter. The primary instrument of ZTF is a novel 600-megapixel camera mounted on the 48-inch Samuel Oschin Schmidt Telescope with a 72-inch (1.8-metre) mirror, designed to rapidly survey the sky for transient and variable phenomena [66].

The ZTF camera contains 16 CCD detectors, each with a resolution of 6144×6160 pixels, resulting in a total field of view of approximately 47 square degrees per exposure. This configuration enables ZTF to image the entire northern sky every two nights and to scan the plane of the Milky Way twice a night. The facility observes in both the visible and near-infrared wavelengths, which allows for the detection of a wide variety of transient events, including dust-obscured and high-redshift phenomena [67].

The survey reaches a limiting magnitude of $r \approx 20.5$ (5σ), making it sensitive to a broad range of astrophysical transients, such as SNe, GRBs, tidal disruption events, and the electromagnetic counterparts of neutron star mergers. ZTF performs a systematic study of the northern sky, enabling not only discovery but also time-domain analysis of transient and variable sources [67]. ZTF produces



Figure 4.1: The 48-inch (1.2-meter) Samuel Oschin Telescope [66].

a significantly larger volume of data compared to its predecessor, generating approximately ten times more detections. This vast data output makes ZTF also a valuable prototype for next-generation facilities such as the Vera C. Rubin Observatory, formerly known as the Large Synoptic Survey Telescope (LSST)[66]. In addition to the 48-inch discovery telescope, ZTF employs the 60-inch telescope at Palomar for rapid spectroscopic follow-up. This telescope is robotically controlled and equipped to deliver low-resolution optical spectra of newly discovered transients, facilitating prompt classification and enabling rapid-response science [66].

ZTF operates with three custom-designed optical filters: ZTF-*g*, ZTF-*r*, and ZTF-*i*. These filters were optimised for high signal-to-noise ratio performance rather than strict conformity with standard photometric systems (e.g. SDSS, PS1, Gaia). This decision was motivated by the goal of maximising the detection efficiency of transient phenomena while avoiding major spectral features that could reduce photometric sensitivity [67].

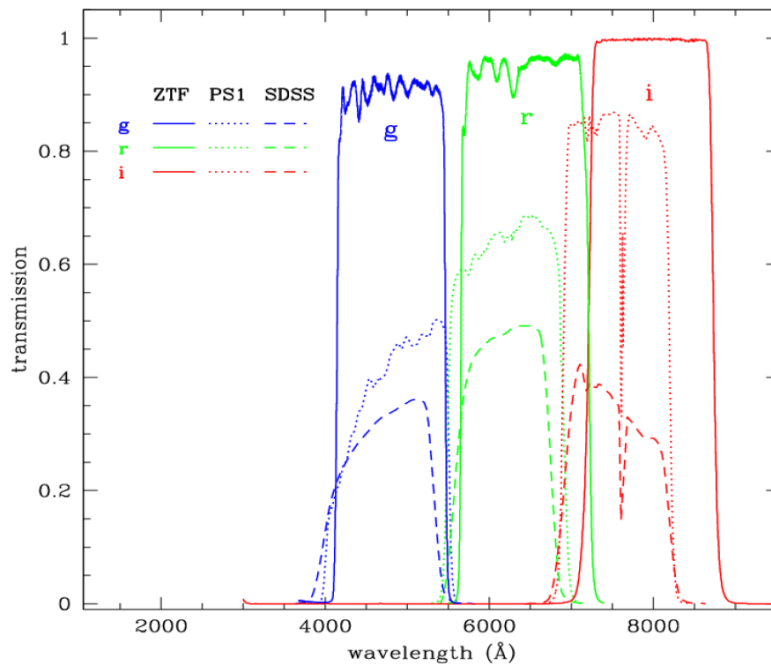


Figure 4.2: A comparison of ZTF *g*, *r*, and *i*-band filters transmission with data from different observational campaigns, the Pan-STARRS1 (PS1) and Sloan Digital Sky Survey (SDSS). Adapted from [26].

Chapter 5

SEDONA

5.1 3D Monte Carlo Radiative Transfer Code

SNe explosions, crucial for understanding the evolution of the universe, emit observable light curves, spectra, and polarisation, offering insights into explosion physics and progenitor stars. Standard and traditional 1D models, although useful, cannot capture the complexity of asymmetric ejecta observed through polarisation and unusual flux features. SEDONA code is able to calculate time-dependent, 3D radiative transfer in SN atmospheres, including detailed treatment of gamma-ray transfer and temperature structure. Either by directly linking or by data input from different multidimensional hydrodynamic models, SEDONA eliminates the need to adjust free parameters in radiative transfer calculations. This approach enables proper modeling of emerging spectra, light curves, and polarization across various viewing angles, which is crucial for validation of theoretical predictions against observational data [7].

Monte Carlo method used in SEDONA follows individual packets of radiative energy - representing photons - as they propagate through the expanding SN ejecta. These photon packets undergo random interactions, such as absorption, scattering, and re-emission, until they eventually escape the SN ejecta or the whole computational domain. Each packet carries information about its wavelength, polarisation state, and energy, which are updated during the simulation process. By tracking a large number of photon packets, SEDONA reconstructs the emergent spectrum and other observable properties of the SN. Unlike traditional numerical radiative transfer methods, Monte Carlo techniques offer greater flexibility in handling complex, multidimensional structures and are less prone to numerical instabilities [7].

One of the strengths of SEDONA is its ability to handle multi-dimensional SN ejecta in the three basic geometries, Cartesian, cylindrical, and spherical. The



Figure 5.1: SEDONA logo [9].

code accepts input from either self-calculated or different hydrodynamic explosion models that describe the density, velocity components, temperature, radiative energy, and chemical composition of the ejected material. It then computes the time evolution of radiative transfer, including non-local thermodynamic equilibrium (NLTE) effects and detailed atomic processes including, e.g. the line fluorescence. Furthermore, SEDONA incorporates a comprehensive treatment of gamma-ray transfer, which plays a crucial role in shaping the observed spectra of SNe due to ejecta heating by radioactive decay chains [10].

In addition to its scientific accuracy, SEDONA is computationally efficient. The Monte Carlo approach allows for straightforward parallelisation, making the code suitable for high-performance computing environments. Despite the inherent statistical noise in Monte Carlo simulations, SEDONA achieves rapid convergence even in highly asymmetric configurations, enabling reliable predictions for a wide range of SN models. The code has been extensively tested against existing radiative transfer codes and observational data, demonstrating its capability to model realistic SN spectra, light curves, and polarisation signatures [10].

By providing a direct and parameter-free connection between multidimensional explosion models and observed SN properties, SEDONA represents significant progress in radiative transfer modelling. Its ability to capture the complexity of SN ejecta makes it an excellent tool for interpreting observational data and improving theoretical models of stellar explosions [7].

SEDONA enables to calculate opacities in various modes, including the grey, Thomson scattering, bound-free, bound-bound, and free-free opacities, for LTE or NLTE regimes. SEDONA includes various atomic data linelists, including, e.g. the Kurucz & Bell database [27] which contains over 40 million spectral lines.

5.2 Generating Synthetic Light Curves

Besides the detailed spectra calculations, SEDONA also outputs a file that provides the time series of the light curve $L(t)$ at frequencies ν and output times t [9]. The bolometric luminosity is simply given as

$$L_{\text{bol}}(t) = \int L(\nu, t) d\nu.$$

Similarly, the absolute bolometric magnitude is given as

$$M_{\text{bol}} = -25 \log_{10} L_{\text{bol}} + 88.697425.$$

In order to obtain light curves in certain filters, you have to convolve the luminosity with a given transmission curve. If $T_b(\nu)$ is the transmission for a given filter band at frequency ν , then the luminosity convolved with the filter is expressed as

$$\mathcal{L}(b) = \frac{\int T_b(\nu) L(\nu, t) d \ln \nu}{\int T_b(\nu) d \ln \nu}.$$

The formula to convert this to an AB magnitude is

$$M_{\text{AB}}(b) = -2.5 \log_{10} \left(\frac{\mathcal{L}(b)}{4\pi d^2} \right) - 48.600,$$

where $d = 10$ pc is the standardized distance to convert to a flux [9].

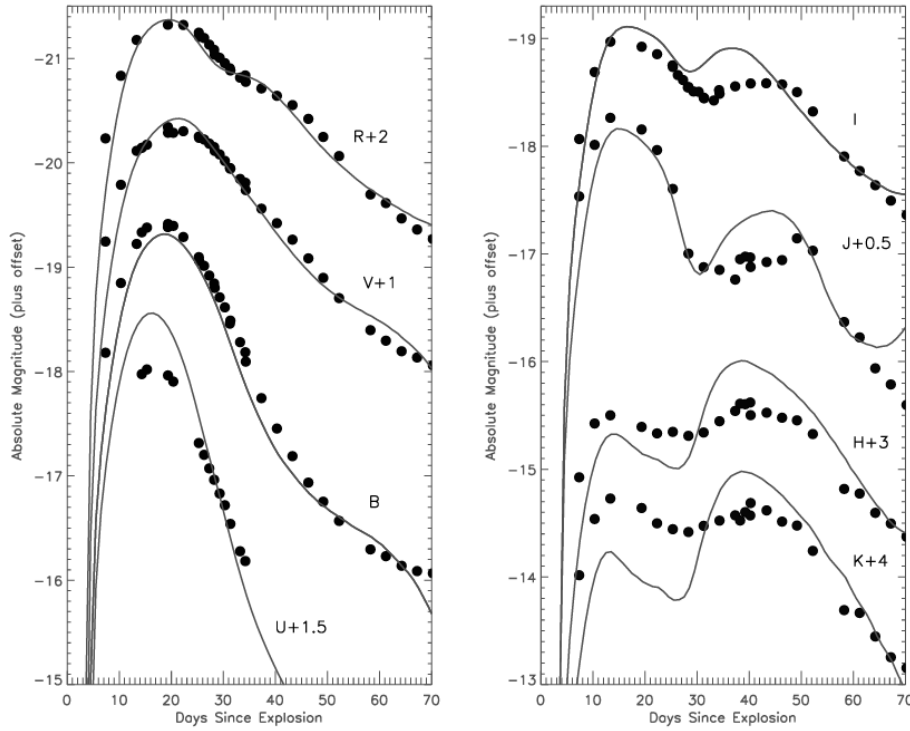


Figure 5.2: Example of the SEDONA calculation of the synthetic UBVRIJHK light curves of the w7 Type Ia SN explosion model from [7]. Overplotted are the Krisciunas et al. 2003 [11] observations of SN 2001el, assuming a distance modulus $m - M = 31.45$ and correcting for an extinction of $A_V = 0.5$ and $R_V = 2.88$. The model seems to match well in terms of rise times, decline rates, and peak magnitudes. However, there is a significant secondary peak in the near-infrared bands (IJHK), which appears stronger in the model than in the actual observations [7].

The plot of absolute magnitudes M calculated in various bands of the Type Ia SN explosion model, is shown in Figure 5.2, adapted from [7]. The extinction corrections A_V and R_V mean the absolute interstellar extinction and the scaled extinction, respectively, where $R_V = A_V/E(B - V)$ is the total extinction divided by the $B - V$ colour excess. For this adjustment, SEDONA includes additional routines to calculate the AB magnitudes in different photometric bands (it stores complete parameters for 175 different bands).

Chapter 6

Photometric Analysis of Supernovae

6.1 Measurement and Post-Processing Overview

We measured eight SNe in total over ten observing nights, from November 2024 to April 2025. The observation itself was preceded by the selection of suitable SN candidates using the latest SN database [2]. The parameters for selecting suitable SNe were: brightness measurable at short exposure (< 19 mag), recent maximum and position in the sky (circumpolar or winter constellation in the northern sky). We have not constrained the SN candidates on the basis of the distance of the SN from the centre of the host galaxy, in order to find the observational limits and the performance of post-processing tools.

SN name	Host galaxy	Discovery date	Discoverer	Type	Max mag
2024vfo	UGC 690	2024/09/11.582	K. Itagaki	II	18.0
2024vim	UGC 4108	2024/09/13.454	Fink	Ia	15.9
2024xqe	LEDA 2078778	2024/10/09.466	PS1	Ia	16.4
2024aecx	NGC 3521	2024/12/16.557	ATLAS	Ic	13.9
2024aeee	NGC 2523	2024/12/17.645	S. Ono	II	15.3
2025dr	UGC 670	2025/01/06.267	ATLAS	Ia	16.1
2025oq	NGC 2744	2025/01/17.024	ATLAS	Ic	14.7
2025qe	IC 529	2025/01/18.262	ATLAS	Iax	15.7

Table 6.1: List of observed SNe with their properties. The discovery date column is in format year/month/day, which contains the fractions of the day. Adapted from [2].

We collected photons using the Vyškov Observatory telescope with a half-meter diameter. The average exposure time in each filter was twenty minutes. We used a CCD camera with three broad-band Johnson filters: B , V , and R . Our observation setup has a resulting FoV of $0.45^\circ \times 0.45^\circ$ and a pixel resolution of $0.786 \text{ arcsec px}^{-1}$. For image post-processing, we use the Munipack [4], which includes photometric correction with biases, dark frames, and flat fields, as well as

astrometric calibration and frame composition in each filter.

The preliminary results of the photometry are given in Table 6.3. These magnitudes include the brightnesses not only of SNe but also of their host galaxies. The next important step will be subtracting the host galaxies using the Galfit programme or other sophisticated methods. It will be essential to convert the measured magnitudes to AB magnitudes in order to properly combine our light curves with data from other observatories. A more detailed analysis of the photometric part of our work will be discussed in the bachelor thesis in progress, *V. Kolaříková: Photometric study of supernovae*.

The images included in this chapter are zoomed in at $500 \text{ px} \times 500 \text{ px}$, which corresponds to the $6.5' \times 6.5'$ angular size of the frames. The length of the blue focus line (to compare the distance of the SN from the centre of the host galaxy) is 90 px , which corresponds to the angular size $71''$.

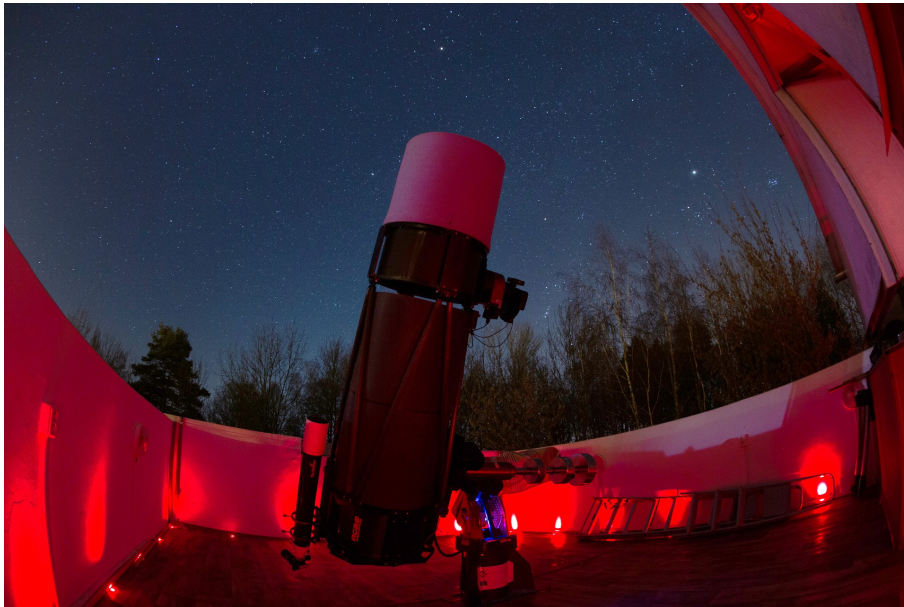


Figure 6.1: Half-meter diameter Newton telescope in Vyškov observatory under the winter starry sky. Photo is taken by V. Kolaříková during our supernova observations.

6.2 Observations of SN Lightcurves

6.2.1 SN2024vfo

The SN2024vfo (also referred to as GOTO24fwv, ZTF24abhbrcs, or ATLAS24oen) was discovered on 2024 September 11.582 by Koichi Itagaki (the date is expressed as the decimal fraction of the day). It is located in galaxy UGC 690 at $RA = 1^h 07^m 27.385^s$ and $Dec = +39^\circ 24' 13.60''$ in the Andromeda constellation, positioned $62.7''$ west and $11.9''$ north (25 kpc) of the center of UGC 690. The SN is classified as Type II [1]. The classification of AT 2024vfo as an SN is confirmed

Date	SN name	Filters	Date	SN name	Filters
2024/11/05	2024vim	B,V	2025/02/10	2025dr	B,V,R
	2024xqe	B,V		2025qe	B,V,R
2024/11/07	2024vfo	B,V,R		2024aecx	B,V,R
	2024xqe	B,V,R	2025/02/18	2024aecx	B,V,R
2024/12/05	2024vfo	B,V,R		2025oq	B,V,R
	2024vim	B,V,R		2025qe	B,V,R
	2024xqe	R	2025/02/20	2024aeer	B,V,R
2025/01/31	2024vim	B,V,R		2025dr	B,V,R
	2024xqe	B,V,R	2025/03/07	2024aeer	B,V,R
	2025oq	B,V,R		2025oq	B,V,R
	2024aecx	B,V,R		2025dr	B,V,R
	2024aeer	B,V,R		2025qe	B,V,R
2024aeer	B,V,R	2024aecx		B,V,R	
2025/02/04	2024aeer	B,V,R	2025/03/18	2024aeer	B,V,R
	2025oq	B,V,R		2025oq	B,V,R
	2025dr	B,V,R		2025dr	B,V,R
	2025qe	B,V,R		2025qe	B,V,R
	2024aecx	B,V,R			

Table 6.2: List of observation nights and measured SNe.

based on early spectral observations from [18]. The early spectrum showed an almost featureless blue continuum with possible broad hydrogen lines at the host redshift (UGC 690: $z_{\text{host}} = 0.019577$, $d = 85.6$ Mpc). The spectrum peak was below observed wavelength range (~ 3000 Å), indicating a temperature higher than 10 000 K [18].

Further classification of SN 2024vfo as a Type II SN is supported by a follow-up spectrum obtained in September 2024 with NOT/ALFOSC (Nordic Optical Telescope, Alhambra Faint Object Spectrograph and Camera). The spectrum revealed a blue continuum with broad P-Cygni Balmer features ($H\alpha$, $H\beta$, $H\gamma$) and an absorption dip at approximately $13\,000$ km s $^{-1}$, as well as a feature of He II at the similar velocity [24].

6.2.2 SN2024xqe

The SN2024xqe (also referred to as PS24jlp or ZTF24ablssfw) was discovered on 2024 October 9.466 at RA = $2^h 21^m 11.941^s$ and Dec = $+36^\circ 19' 48''.69$ in the Triangulum constellation. The SN is classified as a Type Ia [14], with redshift of $z = 0.034$ and the host galaxy is identified as LEDA 2078778 ($z_{\text{host}} = 0.048560$). The SN is located $5.21''$ north and $2.00''$ west of the center of the host galaxy. Additional photometry of the SN on 2024 October 13.436 showed a g-band magnitude of 16.94 (0.01) and a g-r color index of +0.44 (0.02) [1].

6.2.3 SN2024vim

The supernova 2024vim (also referred to as ZTF24abgvscf or Gaia24cpg) was discovered on 2024 September 13.454 by the Fink survey. It is located in UGC 4108 at $RA = 7^h 57^m 32.03^s$ and $Dec = +59^\circ 05' 07''.98$ (Ursa Major constellation), positioned 4.2" west and 5.7" north (2.5 kpc) of the centre of UGC 4108. The SN is classified as Type Ia ($z_{\text{host}} = 0.018946$) [13].

6.2.4 SN2024aecx

The SN2024aecx (also referred to as ZTF24abyaspl, ATLAS24rkq or PS24-msg) was discovered on 2024 December 16.557 by the ATLAS survey. It is located in NGC 3521 ($z_{\text{host}} = 0.002665$) at $RA = 1^h 05^m 49.552^s$ and $Dec = -0^\circ 02' 05.44''$ in the Leo constellation, positioned 14.5" east and 3.7" north (0.8 kpc) from the center of NGC 3521. The SN is classified as Type Ic. Although the light curve and comparisons with SNID [82] and GELATO software suggested that SN was most likely Type IIb, other types of stripped-envelope SN were not excluded [18].

Further spectroscopy from Gemini-N/GMOS (Gemini Multi-Object Spectrographs) was used to classify this event as a Type Ic SN, when it was near its maximum brightness. Both GELATO and SNID indicated that the SN is very similar to the famous SN 1994I [18].

6.2.5 SN2024aeee

The transient 2024aeee (also known as GOTO24jbu, Gaia24dth, and ZTF24abyatjx) was discovered on 2024 December 17.645 by Shinichi Ono. It was found in the galaxy NGC 2523 at coordinates $RA = 8^h 14^m 50.929^s$ and $Dec = +73^\circ 34' 43.94''$ in the Camelopardalis constellation, approximately 37.7" west and 2" north of the center of the galaxy (corresponding to a projected distance of 6.4 kpc). The distance of the host galaxy NGC 2523 is 33.9 Mpc ($z_{\text{host}} = 0.011578$). The observed magnitude was 15.3 on December 29, and the object was classified as a Type II SN [15], with a redshift $z = 0.0116$ (host redshift).

The near maximum spectrum exhibited narrow hydrogen emission lines as well as a blend of He II and N III/C III features around 4650 Å, characteristic of a flash-ionized spectrum of a young hydrogen-rich SN. The event is classified as Type II SN; however, the exact subtype should be determined once the features of the ejecta become clearly visible [15].

6.2.6 SN2025dr

The SN2025dr (also known as ATLAS25agc and ZTF25aabnwba) was discovered on 2025 January 6.267 by the ATLAS survey. It was found in the galaxy UGC 670 at coordinates $RA = 1^h 06^m 46.083^s$ and $Dec = +75^\circ 36' 12.11''$ in the Cassiopeia constellation, located approximately 15.7" west and 10.8" north (corresponding to a projected distance of 6.2 kpc) of the center of UGC 670. The observed magnitude

was 17.0 on February 18 (previously 16.1 on January 20), and it was classified as a Type Ia SN with a host galaxy redshift of $z = 0.015948$. A spectrum recorded approximately seven days after maximum light confirmed the Type Ia SN classification [20].

6.2.7 SN2025oq

The SN2025oq (also known as GOTO25io, ZTF25aacmjq, and ATLAS25als) transient was discovered on 2025 January 17.024 by the ATLAS survey. It was found in the galaxy NGC 2744 at coordinates $RA = 9^h 04^m 38.432^s$ and $Dec = +18^\circ 28' 00.03''$ in the Cancer constellation, located approximately 10.6" west and 10.6" north of the center of NGC2744 (corresponding to a projected distance of 2.7 kpc). The redshift of the host galaxy is $z_{\text{host}} = 0.011$. The matching of the templates suggested good agreement with some young Type Ic SNe, at the known host redshift [21]. The near-peak spectrum was consistent with broad-lined Type Ic SNe [22].

6.2.8 SN2025qe

The transient SN2025qe (also known as ZTF25aacerkv) was discovered on 2025 January 18.262 by the ATLAS survey. It was located in the galaxy IC 529 at coordinates $RA = 9^h 18^m 28.190^s$ and $Dec = +73^\circ 45' 44.89''$ in the Camelopardalis constellation, approximately 19.1" west and 11.3" north of the center of IC529 (corresponding to a projected distance of 3.2 kpc). The first observed magnitude was 15.7 on 28 January 2025, and the object was classified as a Type Ia-02cx SN with redshift $z = 0.0075$ (host redshift $z_{\text{host}} = 0.007532$) [1]. Subsequently, the object was classified as a Type Ia SN [17]. The follow-up observations of the spectrum exhibited strong C,II and weak Si,II characteristics and were generally consistent with Type Iax (02cx-like) SNe [16].

SN	Date	Filter	Magnitude
2024vfo	2024/11/07	B	19.7 ± 0.2
	2024/12/05	R	18.5 ± 0.1
2024vim	2024/11/05	B	17.09 ± 0.03
		V	15.98 ± 0.03
2024xqe	2024/11/05	B	16.70 ± 0.2
		V	15.86 ± 0.01
	2024/11/07	B	16.74 ± 0.02
		V	16.14 ± 0.01
R	15.5 ± 0.3		
2024aecx	2024/01/31	V	15.5 ± 0.2
		R	15.0 ± 0.2
	2024/11/07	V	16.2 ± 0.2
R	15.4 ± 0.2		
2024aeec	2025/01/31	B	17.1 ± 0.02
		V	16.3 ± 0.02
		R	15.9 ± 0.02
	2025/02/04	B	17.1 ± 0.04
		V	16.4 ± 0.03
		R	16.0 ± 0.01
	2025/02/10	V	16.6 ± 0.04
		R	16.1 ± 0.04
	2025/02/20	B	17.9 ± 0.06
		V	16.9 ± 0.04
		R	16.3 ± 0.03
	2025/03/07	V	17.61 ± 0.11
R		17.04 ± 0.07	
2025/03/18	B	18.54 ± 0.12	
	V	17.95 ± 0.12	
	R	17.5 ± 0.1	

SN	Date	Filter	Magnitude
2025dr	2025/02/04	B	17.6 ± 0.06
		V	16.7 ± 0.04
		R	16.48 ± 0.04
	2025/02/10	V	17.2 ± 0.1
		R	16.57 ± 0.08
	2025/02/20	B	19.56 ± 0.37
		V	17.67 ± 0.11
		R	16.86 ± 0.08
	2025/03/07	V	19.18 ± 0.61
R		17.85 ± 0.24	
2025/03/18	V	18.65 ± 0.29	
	R	17.9 ± 0.2	
2025oq	2025/01/31	B	16.11 ± 0.01
		V	15.465 ± 0.009
		R	15.22 ± 0.01
	2025/02/04	B	16.50 ± 0.02
		V	16.696 ± 0.001
		R	15.36 ± 0.01
	2025/02/18	B	16.98 ± 0.03
		V	16.22 ± 0.02
		R	15.82 ± 0.02
2025/03/07	B	17.16 ± 0.05	
	V	16.46 ± 0.04	
	R	16.16 ± 0.04	
2025/03/18	B	17.17 ± 0.04	
	V	16.58 ± 0.03	
	R	16.58 ± 0.03	
2025qe	2025/02/04	B	17.23 ± 0.04
		V	16.38 ± 0.03
		R	16.01 ± 0.03
	2025/02/10	B	18.4 ± 0.4
		V	16.95 ± 0.08
		R	16.29 ± 0.07
	2025/02/18	B	18.85 ± 0.17
		V	17.43 ± 0.07
		R	16.66 ± 0.06
2025/03/07	V	17.73 ± 0.15	
	R	17.1 ± 0.1	
2025/03/18	V	17.97 ± 0.13	
	R	17.4 ± 0.1	

Table 6.3: Estimated magnitudes of measured SNe without subtraction of host galaxies by V. Kolaříková (whose bachelor thesis on a related topic is currently in progress), with the use of Munipack [4].

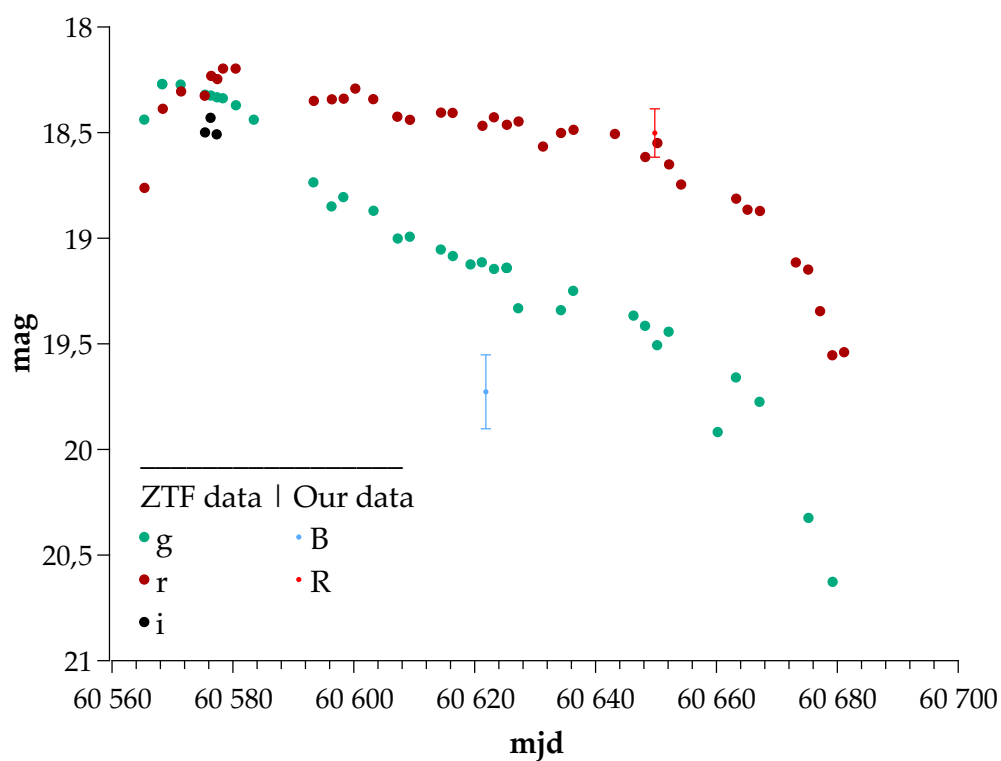
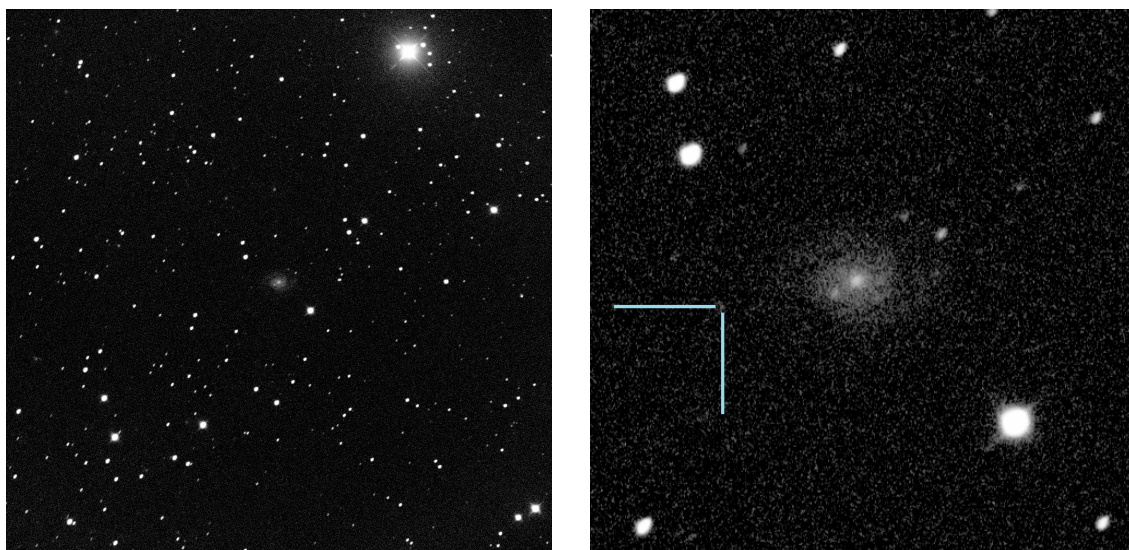


Figure 6.2: Image of the **SN2024vfo** (SN type II) in the host galaxy UGC 690. Image is taken in the V filter with 20 minutes exposure time during the night of 2024/11/07. Light curve is a combination of our (B , V , R) and ZTF (g , r , i) data from ALerCE ZTF [1].

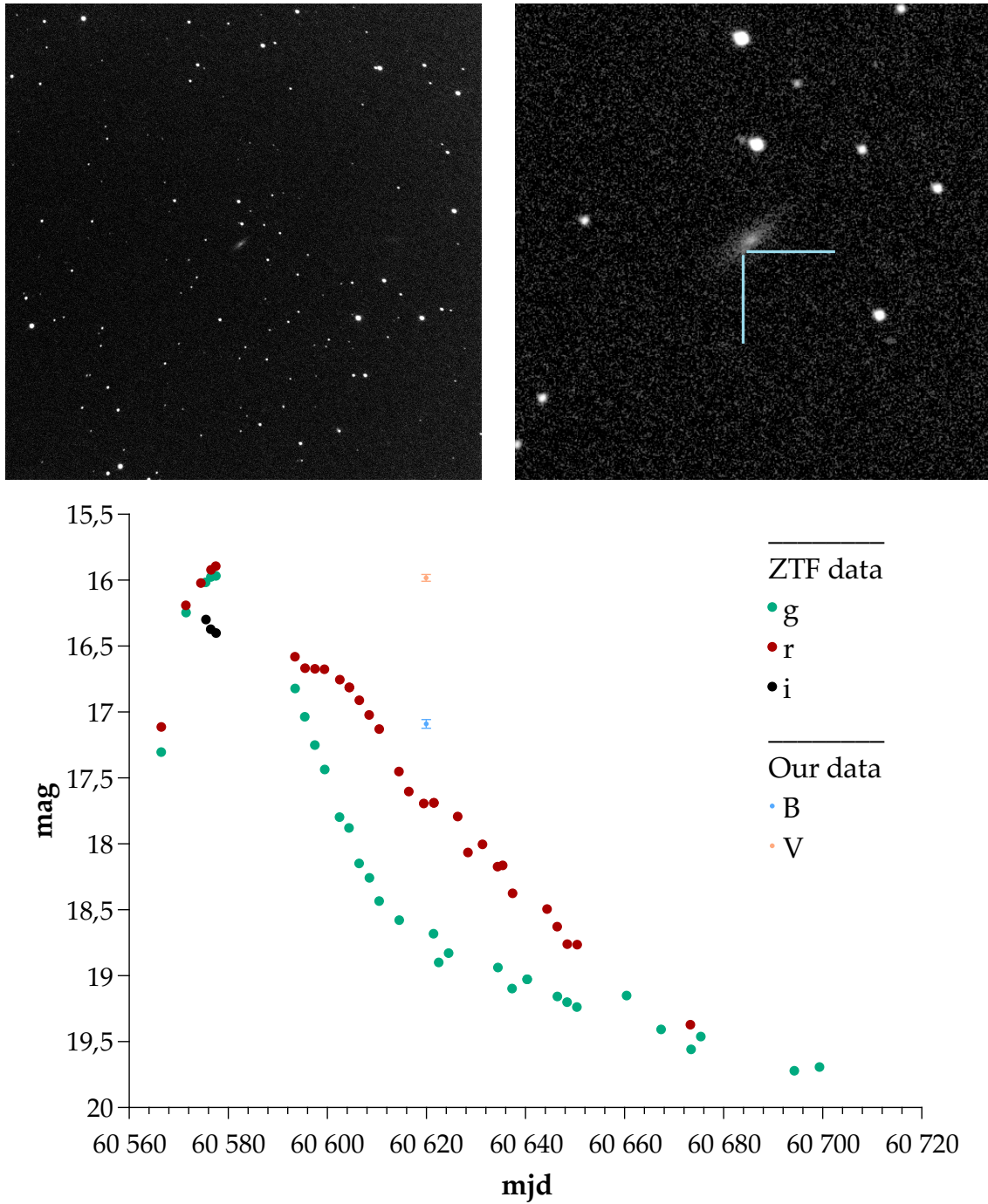


Figure 6.3: Image of the **SN2024vim** (SN type Ia) in the host galaxy UGC 4108. Image is taken in the B filter with 20 minutes exposure time during the night of 2024/11/07. Light curve is a combination of our (B , V , R) and ZTF (g , r , i) data from ALeRCE ZTF [1].

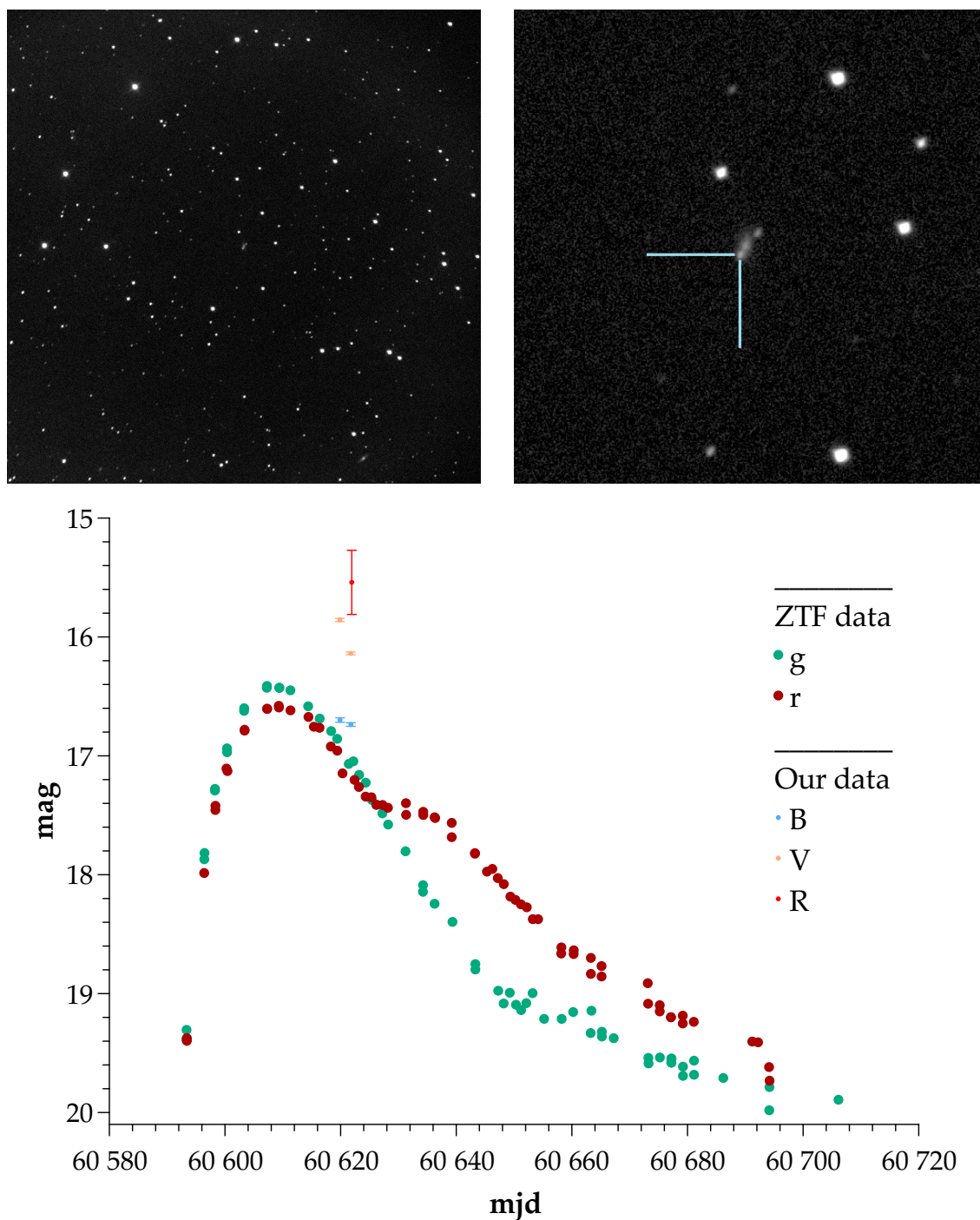


Figure 6.4: Image of the **SN2024xqe** (SN type Ia) in the host galaxy LEDA 2078778. Image is taken in the V filter with 20 minutes exposure time during the night of 2024/11/07. Light curve is a combination of our (B , V , R) and ZTF (g , r , i) data from ALerCE ZTF [1].

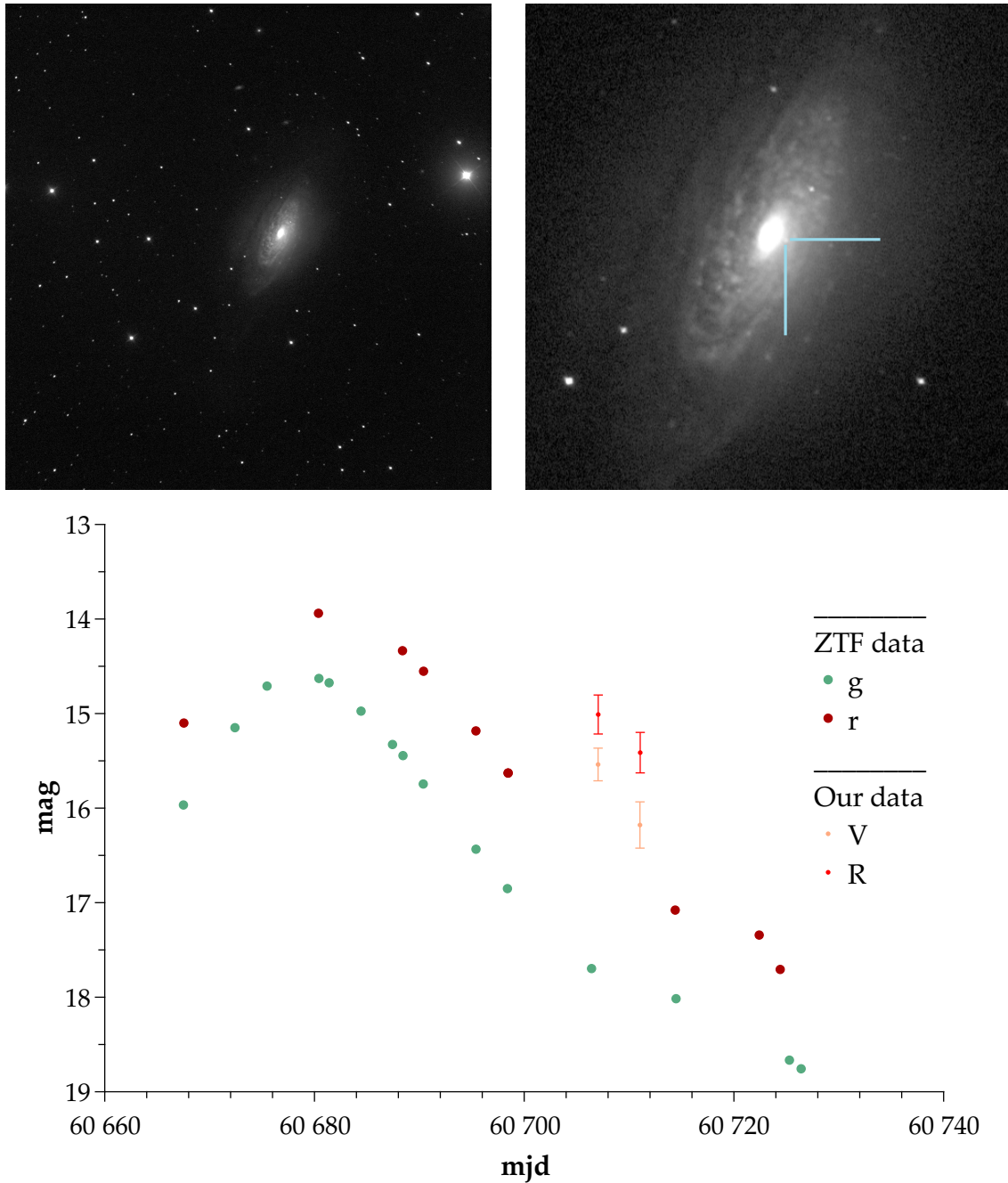


Figure 6.5: Image of the **SN2024aecx** (SN type Ic) in the host galaxy NGC 3521. Image is taken in the V filter 20 minutes exposure time during the night of 2025/02/04. Light curve is a combination of our (B , V , R) and ZTF (g , r , i) data from ALeRCE ZTF [1].

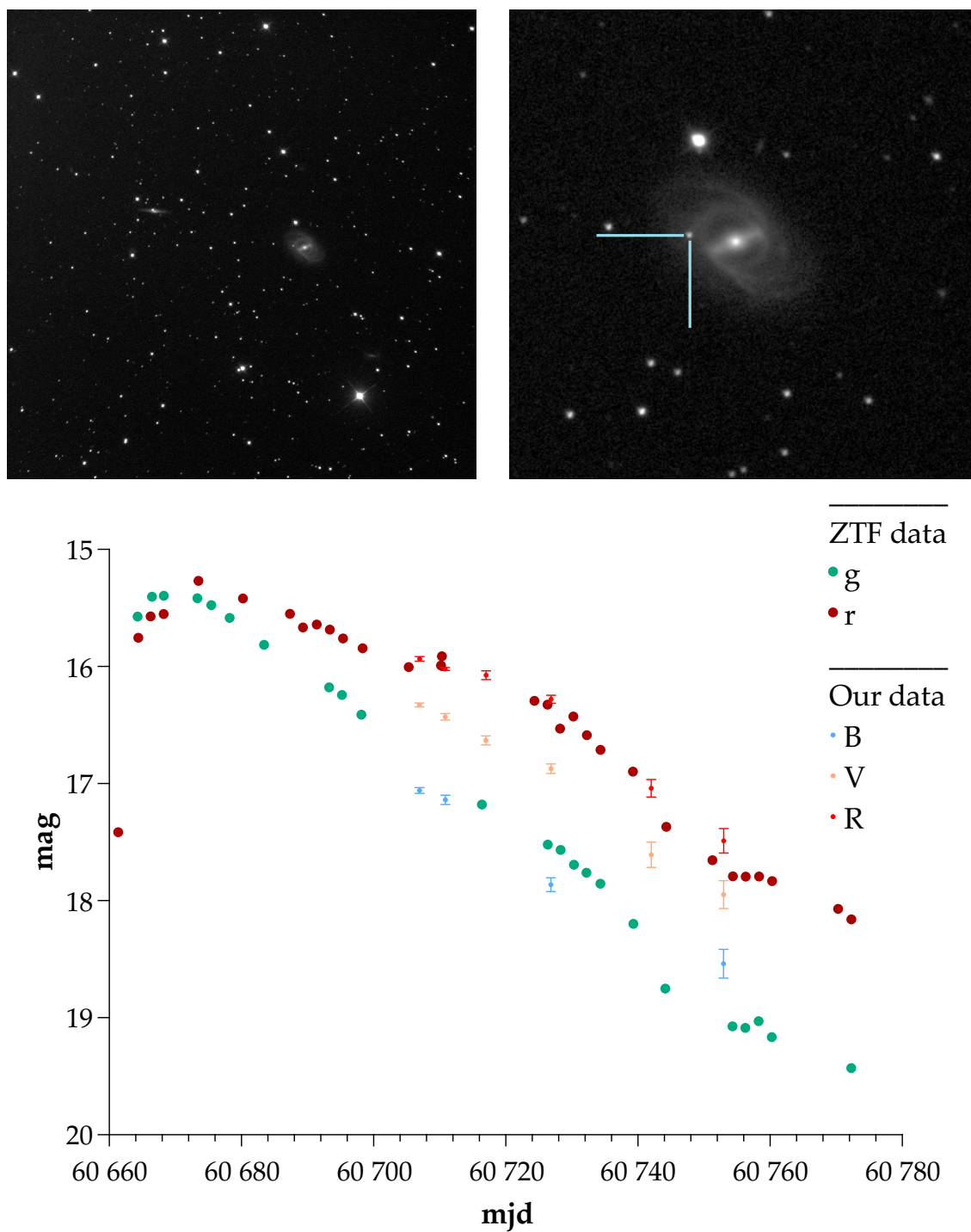


Figure 6.6: Image of the **SN2024aeae** (SN type II) in the host galaxy NGC 2523. Image is taken in the R filter 20 minutes exposure time during the night of 2025/02/04. Light curve is a combination of our (B , V , R) and ZTF (g , r , i) data from ALerCE ZTF [1].

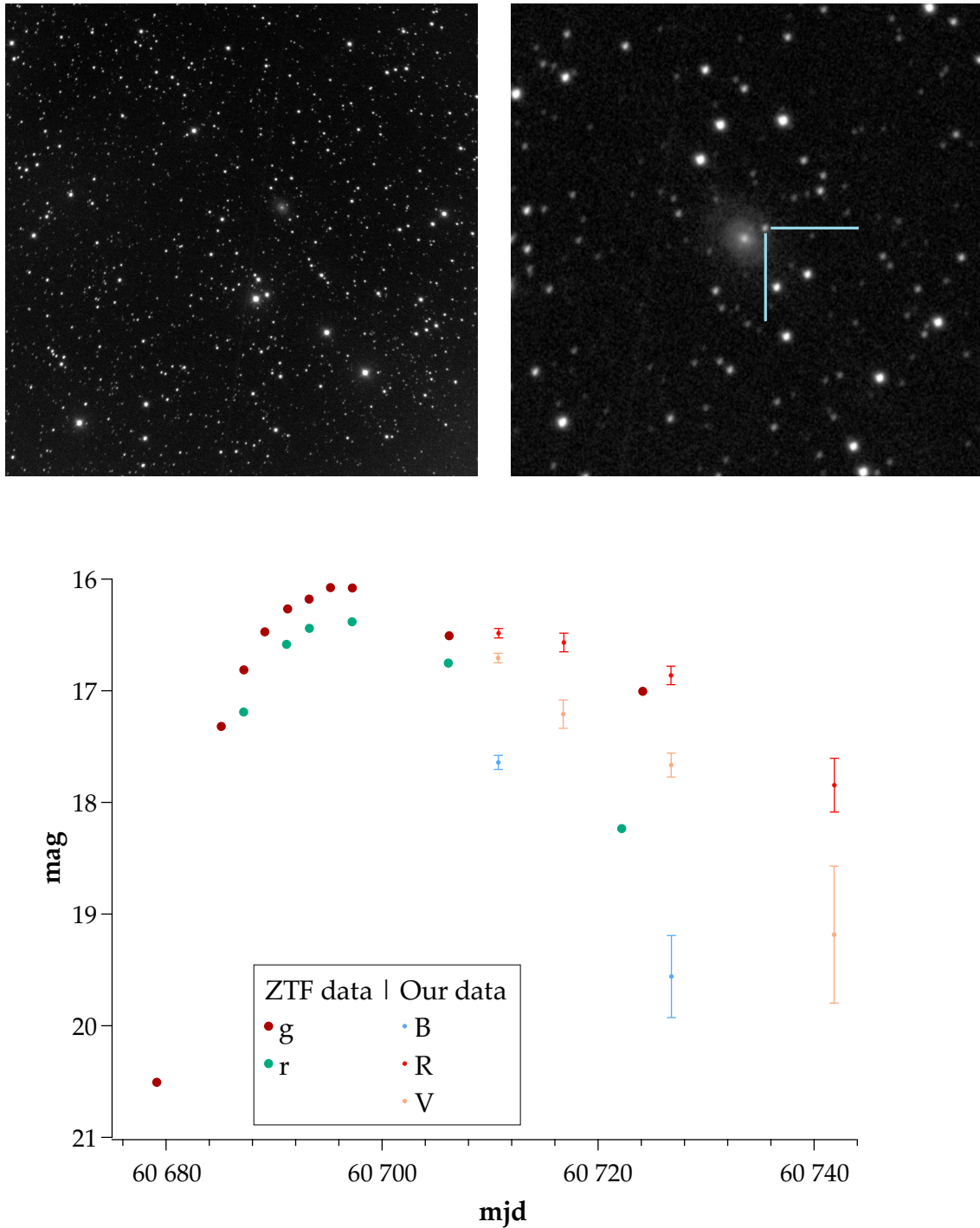


Figure 6.7: Image of the **SN2025dr** (SN type Ia) in the host galaxy UGC 670. Image is taken in the V filter 20 minutes exposure time during the night of 2025/02/04. Light curve is a combination of our (B , V , R) and ZTF (g , r , i) data from ALerCE ZTF [1].

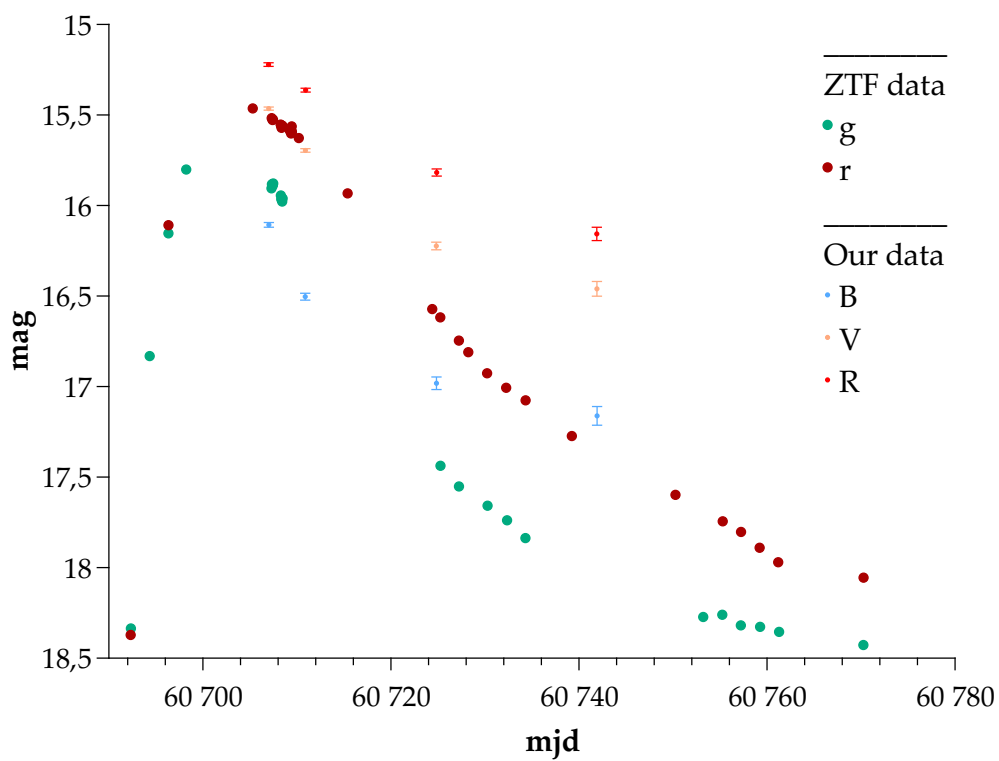
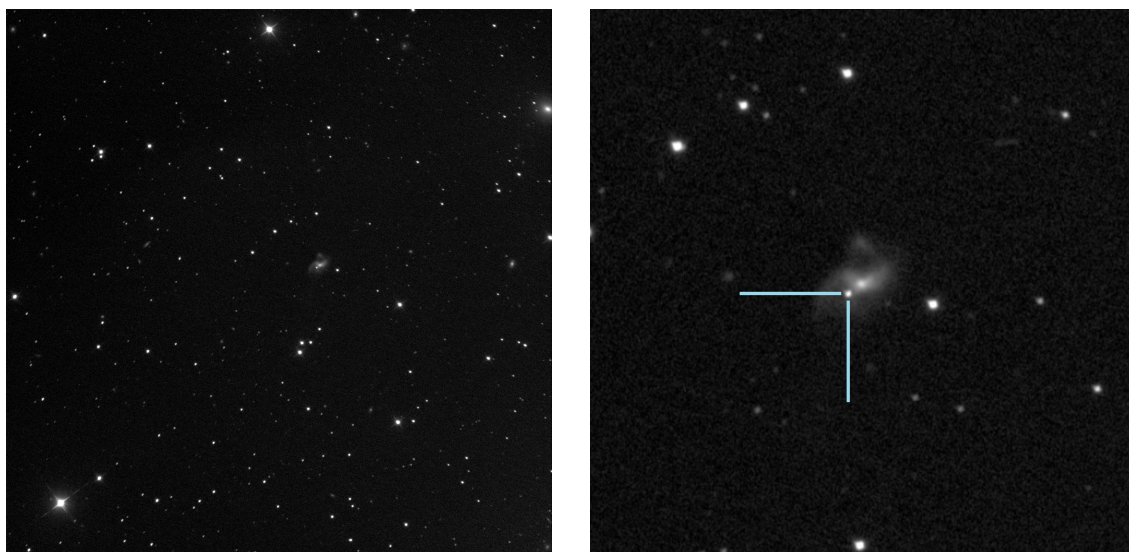


Figure 6.8: Image of the **SN2025oq** (SN type Ic) in the host galaxy NGC 2744. Image is taken in the R filter 20 minutes exposure time during the night of 2025/02/04. Light curve is a combination of our (B, V, R) and ZTF (g, r, i) data from ALerCE ZTF [1].

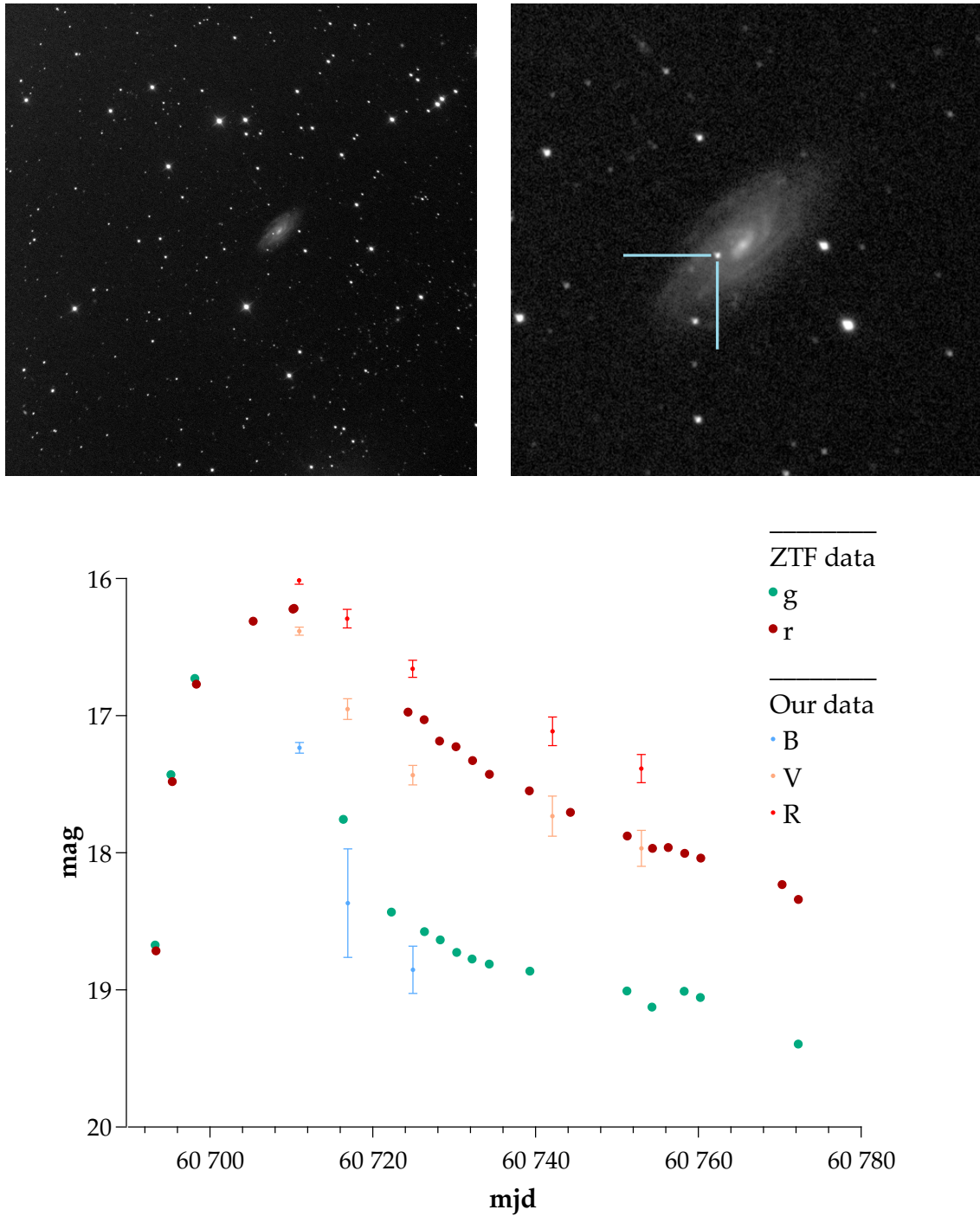


Figure 6.9: Image of the SN2025qe (SN type Iax) in the host galaxy C 529. Image is taken in the R filter 20 minutes exposure time during the night of 2025/02/04. Light curve is a combination of our (B , V , R) and ZTF (g , r , i) data from ALerCE ZTF [1].

6.3 Distance Modulus and Galactic Extinction

Model light curves in following Chapter 7 are calculated in absolute magnitudes. For specific SNe, we converted the absolute magnitudes to apparent magnitudes using the Pogson equation, including the extinction and reddening caused by the dust and gas in the Milky Way. The redshifts z are taken from the spectral observations reported in [2], and the luminosity distances are calculated using the cosmology calculator from [29], assuming a flat universe with $H_0 = 67.74 \text{ km s}^{-1} \text{ Mpc}^{-1}$, $\Omega_{M_0} = 0.31$ and $\Omega_{\Lambda_0} = 0.69$. Here, H_0 denotes the Hubble constant, Ω_{M_0} the matter density parameter and Ω_{Λ_0} the vacuum energy density parameter, both relative to the critical density. These cosmological parameters are adopted from the Planck Collaboration 2015 results [68].

We calculated the Galactic extinction factors A in the SDSS g , r , i filters in the direction of each SN with the use of [28]. The used extinction law, assuming the ratio $R_V = A_V/E(B-V) = 3.1$, is adopted from [69] and [70]. All these parameters are listed in Table 6.4. The formula of the resulting conversion is

$$m = M + 2.5 \log D_L - 5 + A. \quad (6.1)$$

SN name	z	D_L [Mpc]	μ [mag]	A_g [mag]	A_r [mag]	A_i [mag]
2024vim	0.01895	85.1	34.6084	0.208	0.151	0.114
2024xqe	0.03400	154.4	35.8703	0.254	0.185	0.140
2024vfo	0.01958	87.9	34.6775	0.183	0.133	0.101
2025oq	0.01133	50.6	33.4949	0.117	0.085	0.064
2024aeee	0.01160	51.8	33.5463	0.115	0.083	0.063
2025dr	0.01595	71.4	34.2348	1.420	1.030	0.781
2024aecx	0.00267	11.8	30.3594	0.218	0.158	0.120
2025qe	0.00750	33.4	32.5991	0.089	0.064	0.049

Table 6.4: List of SNe with their redshifts, luminosity distances, distance moduli and galactic extinction in SDSS g , r , and i filters.

Chapter 7

Modelling of Supernova Light Curves

7.1 SN Type Ia

The SEDONA SN type Ia model consists of SN ejecta moving in homologous expansion (that means, that velocity is proportional to radius) with a density profile of the power law. The parameters of the model are the mass of the ejecta $M [M_{\odot}]$, the kinetic energy $E_k [\text{erg}]$, the maximum velocity at the outer edge of the ejecta $v_{\text{max}} [\text{cm s}^{-1}]$, the initial temperature $T [\text{K}]$ and the number of radial zones n_x . The compositional structure is composed of 3 layers: the inner $M_{\text{Ni}} [M_{\odot}]$ of the ejecta is pure radioactive ^{56}Ni the surrounding $M_{\text{ime}} [M_{\odot}]$ is a mixture of intermediate-mass elements (Si, S, Ca) and the remaining mass in the outer layers is a 1:1 mixture of carbon and oxygen. The radioactive ^{56}Ni will be the energy source of the radiation that is then observed in the final spectrum. The SN Type Ia models include the following elements: ^{12}C , ^{16}O , ^{28}Si , ^{32}S , ^{40}Ca , ^{56}Fe , ^{56}Co , and ^{56}Ni [8].

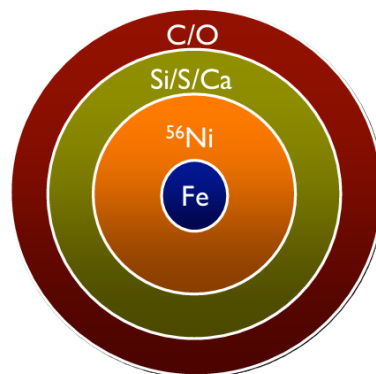


Figure 7.1: Example of compositional structure of SN Type Ia model. Adapted from [25].

The parametric setup used for the initial density calculation is given as

$$M_{\odot} = 1,99 \times 10^{33} \text{ g}, \quad (7.1)$$

$$t_{\text{exp}} = 2 \text{ days}, \quad (7.2)$$

$$r_{\text{max}} = v_{\text{max}} t_{\text{exp}}, \quad (7.3)$$

$$v_e = \sqrt{\frac{E_k}{6 M M_{\odot}}}, \quad (7.4)$$

$$\rho_0 = \frac{M M_{\odot}}{8\pi(v_e t_{\text{exp}})^3}. \quad (7.5)$$

where v_e is the characteristic velocity of the ejecta derived from the kinetic energy E_k and the mass of the ejecta M , t_{exp} is the SN explosion time used as an initial time in the SEDONA hydrodynamic models, and r_{max} is the radius of the outer SN ejecta that propagates homologously. The calculations use LTE atomic line data taken from the Kurucz list ("fuzz"), with 2×10^4 radioactive particles (photon packets) emitted in each time step. The frequency grid for the opacity calculations ranges from $\nu_1 = 10^{14}$ Hz to $\nu_2 = 10^{16}$ Hz, and the maximum time step for the calculation of the spectrum in the "time grid" is set to 1 day.

7.1.1 SN Ia models for examining the effect of model parameters on light curves

Before modelling the light curves of real SNe, observed by us and ZTF, we tested the SEDONA built-in model of SN Ia by changing its parameters and plotting synthetic light curves in ZTF filters g , r , and i . All synthetic light curves were calculated with $n_x = 100$ radial zones and 1 day time step.

Effect of the Nickel Mass M_{Ni}

First synthetic light curves (Figure 7.2) of SN type Ia show dependence of g , r , i absolute magnitudes on the mass of ^{56}Ni . The estimated range of ^{56}Ni mass for normal SNe Ia from [12] is $0.09 - 0.87 M_{\odot}$. The light curves were plotted in the range $M_{\text{Ni}} = 0.1 - 0.8 M_{\odot}$ and for the total mass $M = 1.0 M_{\odot}$. Other parameters remained fixed at the following values, $M_{\text{ime}} = 0.3 M_{\odot}$, $E_k = 1 \times 10^{51}$ erg, $v_{\text{max}} = 1 \times 10^9 \text{ cm s}^{-1}$, $T = 10^4 \text{ K}$.

In the first graphs 7.2, we can already see a strong correlation between ^{56}Ni mass and absolute magnitude in all filters. In filters r and i , the amount of nickel strongly increases the second maximum. As the total mass remained fixed at $M = 1.0 M_{\odot}$, the last two light curves with $M_{\text{Ni}} = 0.7 M_{\odot}$ and $M_{\text{Ni}} = 0.7 M_{\odot}$ are models for ejecta without an outer carbon-oxygen layer.

In the second set of light curves (Figure 7.3), the ratio between M_{Ni} and M_{ime} varies from 4:5 to 8:1, while the total mass is fixed at $M = 1.0 M_{\odot}$. These light curves are more physical than the previous ones, as the carbon-oxygen layer remains fixed at $M_{\text{CO}} = 1.0 M_{\odot}$. Other fixed parameters are $E_k = 1 \times 10^{51}$ erg,

$v_{\max} = 1 \times 10^9 \text{ cm s}^{-1}$, $T = 10^4 \text{ K}$. The light curves of the models with the most nickel have the highest magnitudes. The change in the $M_{\text{Ni}}/M_{\text{ime}}$ ratio affects the relative heights of the first and second maxima in the r and i filters.

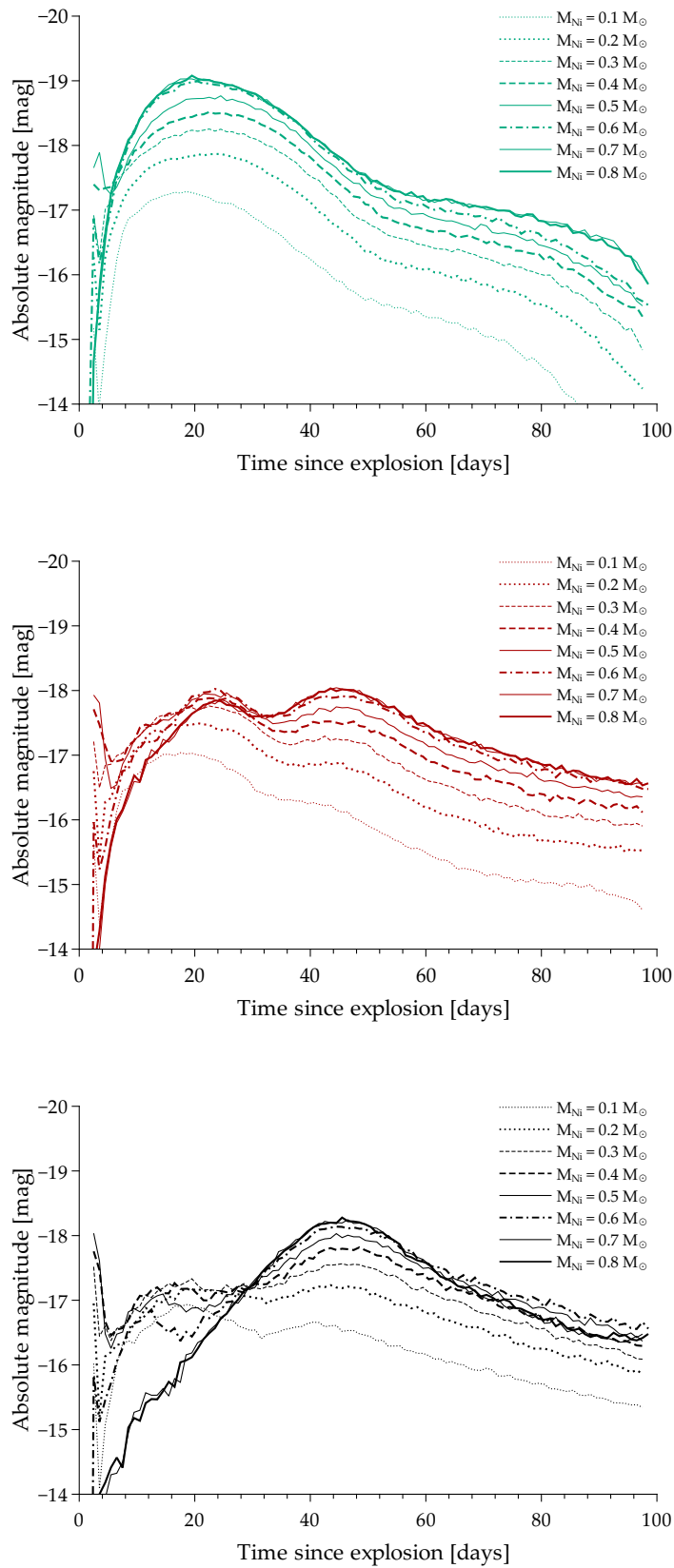


Figure 7.2: SN Type Ia model light curves in ZTF *g*, *r*, *i* filters with variable ^{56}Ni mass.

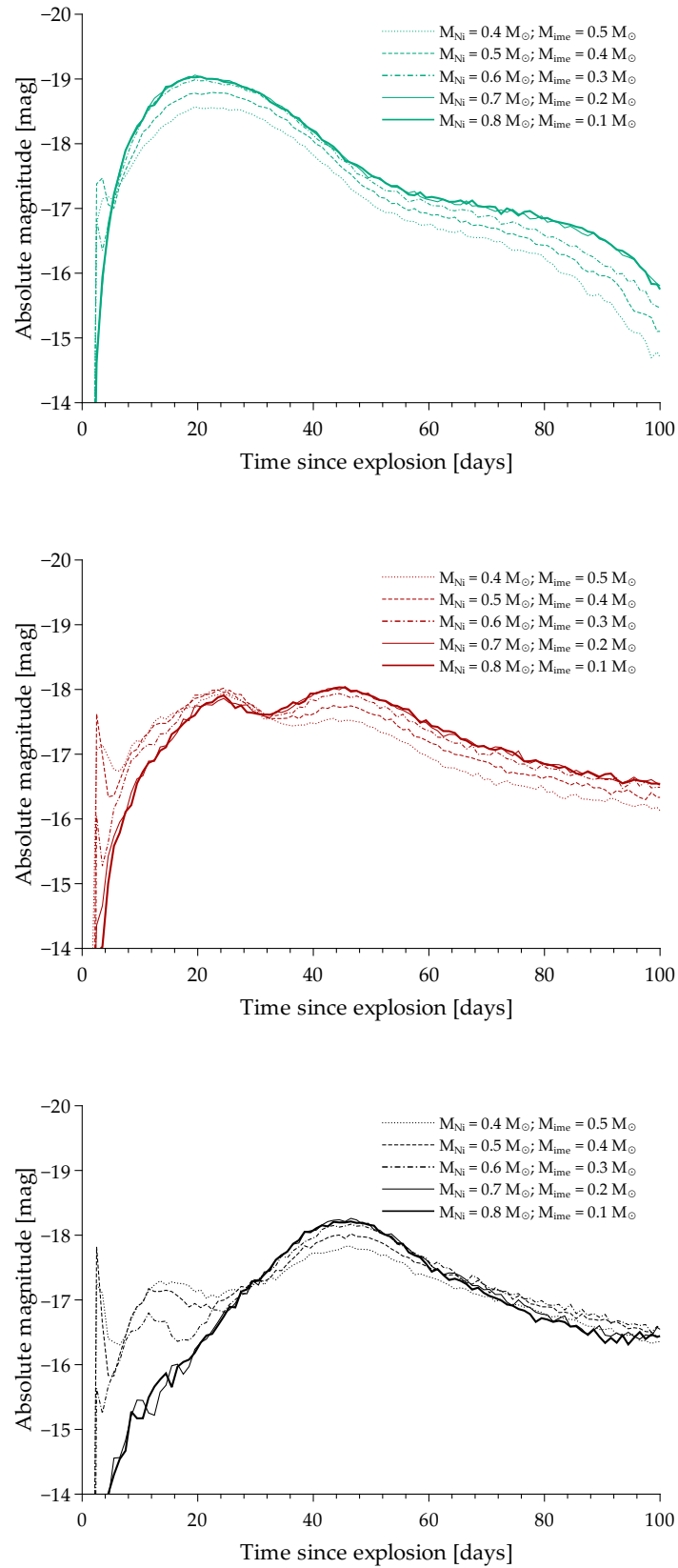


Figure 7.3: SN Type Ia model light curves in ZTF *g*, *r*, *i* filters with variable ratio of M_{Ni} and M_{ime} .

Effect of the Mass of the Intermediate-Mass Elements M_{ime}

Figure 7.4 shows that the light curves are only minimally affected by the change in M_{ime} . The fixed parameters are $M = 1 M_{\odot}$, $M_{\text{Ni}} = 0.3 M_{\odot}$, $E_k = 1 \times 10^{51}$ erg, $v_{\text{max}} = 1 \times 10^9$ cm s $^{-1}$, $T = 10^4$ K.

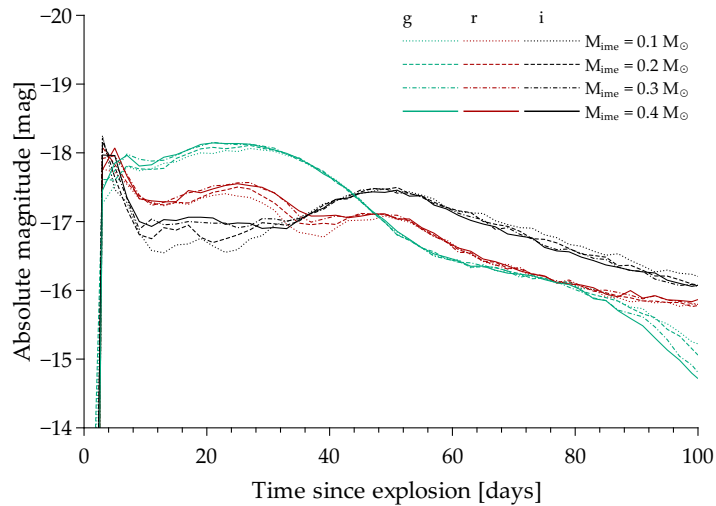


Figure 7.4: SN Type Ia model light curves in ZTF g , r , i filters with variable mass of the intermediate-mass elements.

Effect of the Mass of the Ejecta M

The third observed influencing parameter is the total ejected mass M . In Figure 7.5 M_{Ni} and M_{ime} remain fixed ($M_{\text{Ni}} = 0.3 M_{\odot}$, $M_{\text{ime}} = 0.3 M_{\odot}$), which means that with increasing M , we actually increase M_{CO} . The other parameters remain unchanged, $v_{\text{max}} = 1 \times 10^9$ cm s $^{-1}$, $T = 10^4$ K.

Figure 7.6 compares the light curves of regular Type Ia SNe and the super-Chandrasekhar Type Ia SNe (originating from double white dwarf binaries) that exceed the Chandrasekhar mass limit ($1.4 M_{\odot}$). For these light curves, the ratio $M_{\text{Ni}}/M_{\text{ime}}$ remains 2 : 1. The exact values of the parameters are listed in Table 7.1.

	$M [M_{\odot}]$	$M_{\text{Ni}} [M_{\odot}]$	$M_{\text{ime}} [M_{\odot}]$	E_k [erg]	v_{max} [cm s $^{-1}$]	T [K]
model 1	0.5	0.3	0.15	1×10^{51}	1×10^9	10^4
model 2	1.0	0.6	0.3	1×10^{51}	1×10^9	10^4
model 3	1.5	0.9	0.45	1×10^{51}	1×10^9	10^4
model 4	2.0	1.2	0.6	1×10^{51}	1×10^9	10^4
model 5	2.5	1.5	0.75	1×10^{51}	1×10^9	10^4

Table 7.1: Parameters for light curves in Figure 7.6, with variable mass of the ejecta

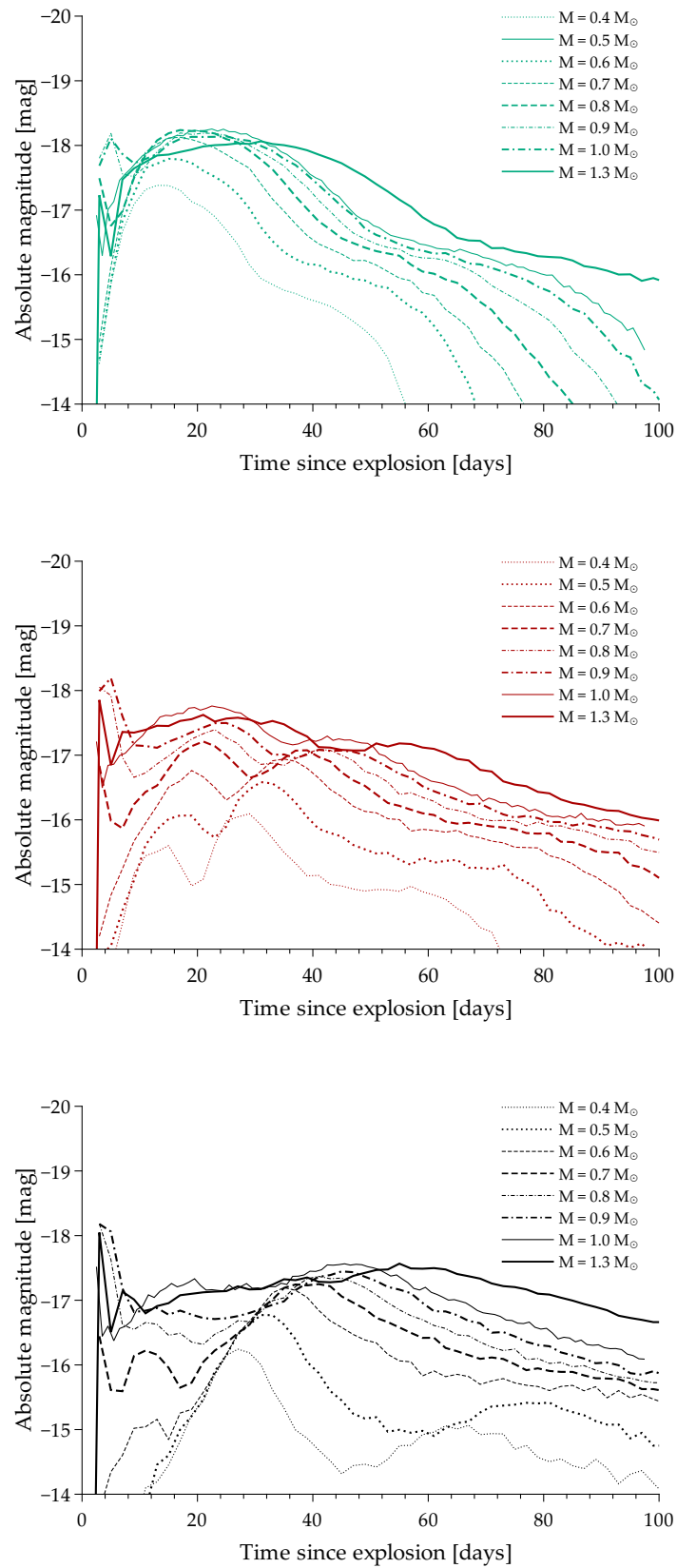


Figure 7.5: SN Type Ia model light curves in ZTF *g*, *r*, *i* filters with variable ejected mass.

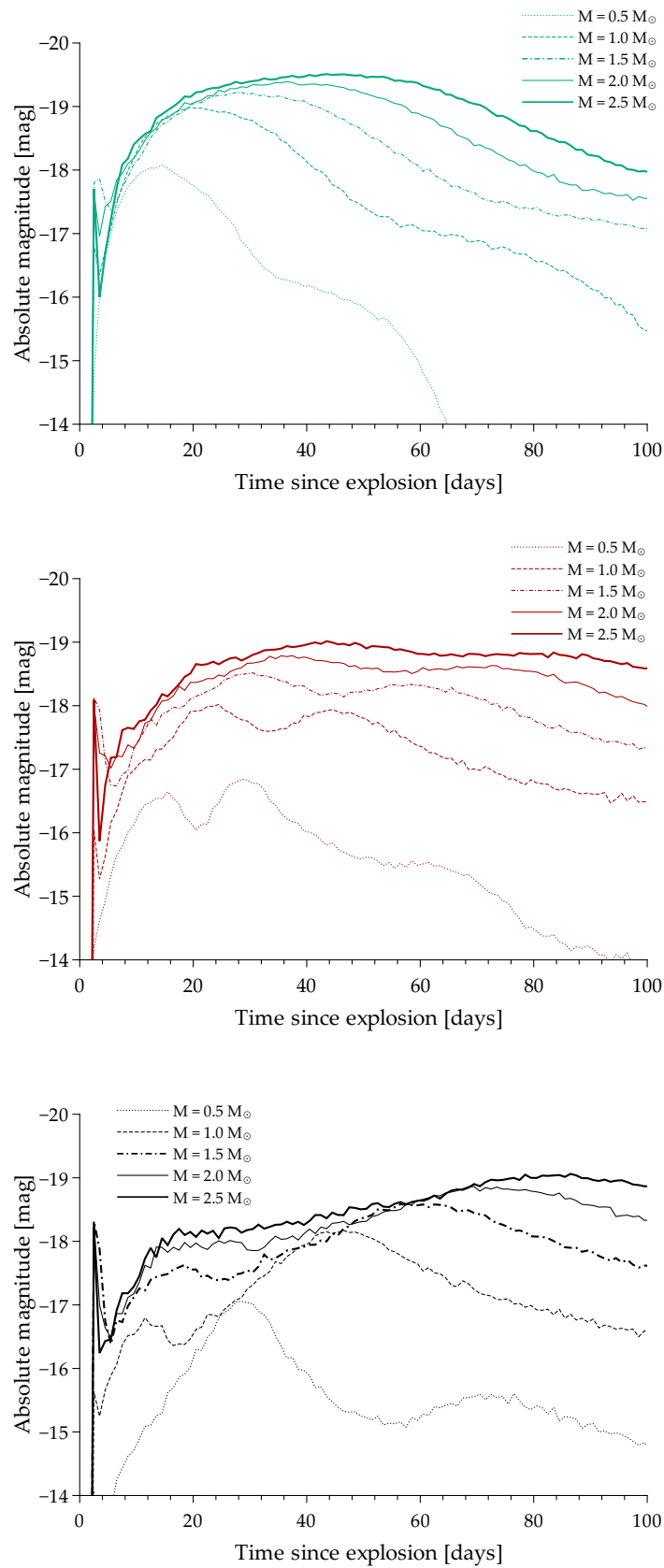


Figure 7.6: SN Type Ia model light curves in ZTF *g*, *r*, *i* filters with variable ejected mass.

Effect of the Velocity v_{\max}

The maximum of the outer velocity v_{\max} affects the heights of first maxima in all filters (Figure 7.7). The invariable parameters are $M = 1 M_{\odot}$, $M_{\text{Ni}} = 0.2 M_{\odot}$, $M_{\text{ime}} = 0.1 M_{\odot}$, $E_k = 1 \times 10^{51}$ erg, $T = 10^4$ K.

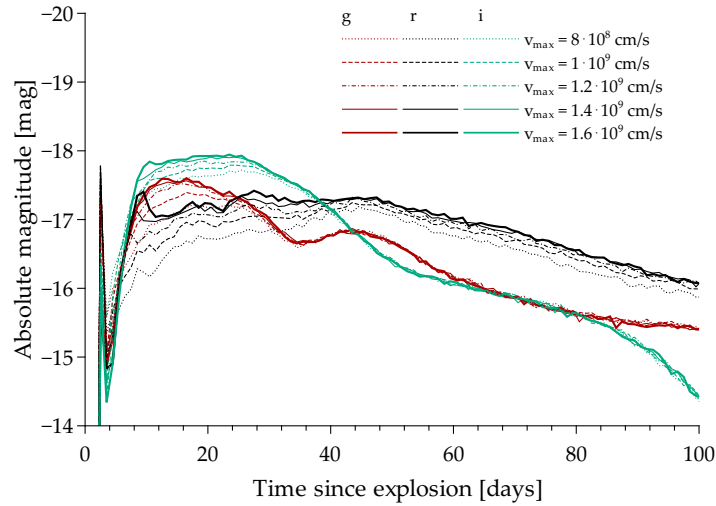


Figure 7.7: SN Type Ia model light curves in ZTF g , r , i filters with variable velocity.

Effect of the Temperature T

The temperature has almost no effect on the shape of the light curves (Figure 7.8). The values of the unchanging parameters are $M = 1 M_{\odot}$; $M_{\text{Ni}} = 0.3 M_{\odot}$, $M_{\text{ime}} = 0.1 M_{\odot}$, $E_k = 1 \times 10^{51}$ erg, $v_{\max} = 1 \times 10^9$ cm s $^{-1}$.

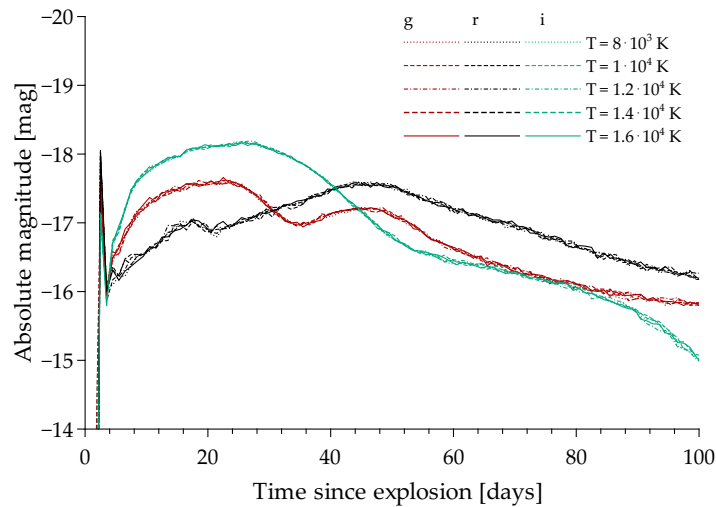


Figure 7.8: SN Type Ia model light curves in ZTF g , r , i filters with variable T .

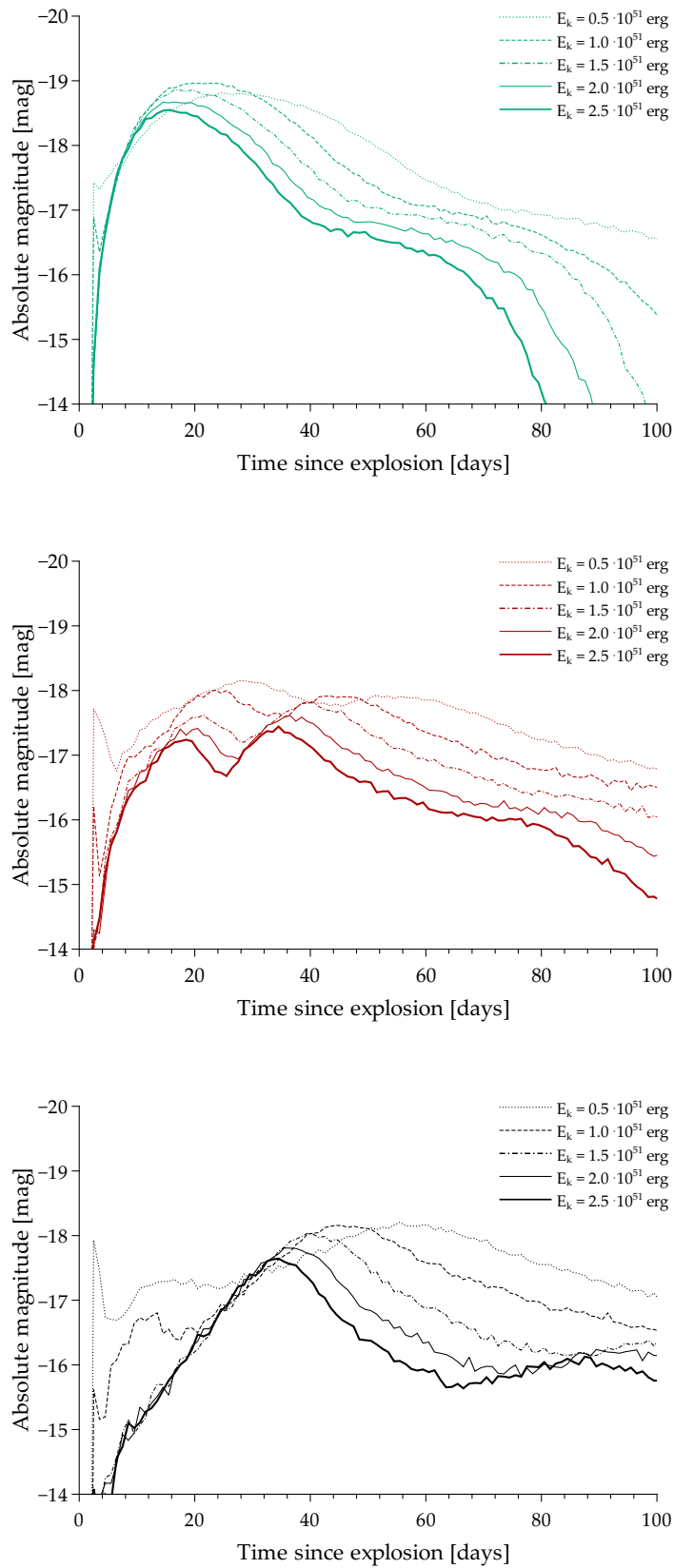


Figure 7.9: SN Type Ia model light curves in ZTF g, r, i filters with variable kinetic energy.

Effect of the Kinetic Energy E_k

As the kinetic energy increases, the overall brightness in all filters decreases (Figure 7.9). Other model parameters are fixed at $M = 1 M_\odot$, $M_{\text{Ni}} = 0.6 M_\odot$, $M_{\text{ime}} = 0.3 M_\odot$, $v_{\text{max}} = 1 \times 10^9 \text{ cm s}^{-1}$, $T = 10^4 \text{ K}$.

7.1.2 SN2024vim and SN2024xqe

SNe SN2024vim and SN2024xqe have a very similar shape of their light curves with prominent r -bump in 40 days. We confronted their measured data with the same models from Table 7.2. These synthetic light curves are plotted in Figure 7.10. The graphs of the bolometric quantities M_{bol} and L_{bol} are also plotted for the corresponding models in Figure 7.11.

The result graphs with the observed and synthetic light curves are in Figures 7.12 and 7.13. The graphs indicate that model 3 (in Table 7.2) is the most appropriate model to describe the shape of the light curves in all filters. The only discrepancy is the difference in the absolute displacement of the light curves. For SN2024vim is the vertical displacement $\sim 1 \text{ mag}$, in the case of SN2024xqe, the difference is greater than $\sim 1.5 \text{ mag}$. This shift is most likely explained by the presence of interstellar matter in the vicinity of the SN or by the effect of interstellar extinction, which would increase the apparent magnitude.

	$M [M_\odot]$	$M_{\text{Ni}} [M_\odot]$	$M_{\text{ime}} [M_\odot]$	$E_k [\text{erg}]$	$v_{\text{max}} [\text{cm s}^{-1}]$	$T [\text{K}]$
model 1	0.5	0.1	0.2	1×10^{51}	1.8×10^9	10^4
model 2	0.5	0.2	0.4	1×10^{51}	1.8×10^9	10^4
model 3	1.0	0.2	0.7	1×10^{51}	1.8×10^9	10^4
model 4	1.3	0.3	0.9	0.8×10^{51}	1.8×10^9	10^4
model 5	1.1	0.3	0.7	1×10^{51}	1.8×10^9	10^4

Table 7.2: List of parameters of SN Ia models, used for SN2024vim and SN2024xqe.

7.1.3 SN2025dr

It is evident that the observed light curve of SN2025dr contains only a limited number of measured data points near the maximum. Possible models (Table 7.3) that could fit this SN are shown in 7.14, together with the measured data. The graphs of M_{bol} and L_{bol} for these three models are plotted in Figure 7.15.

7.1.4 SN2025qe

Table 7.4 shows parameters of tested models for this SN type Ia. Figure 7.17 shows the best of tested models for this SN type Ia (Table 7.4) that could correspond to

	$M [M_{\odot}]$	$M_{\text{Ni}} [M_{\odot}]$	$M_{\text{ime}} [M_{\odot}]$	$E_k [\text{erg}]$	$v_{\text{max}} [\text{cm s}^{-1}]$	$T [\text{K}]$
model 1	1.0	0.2	0.7	1×10^{51}	1.8×10^9	10^4
model 2	1.0	0.4	0.5	0.8×10^{51}	1×10^9	10^4
model 3	1.1	0.8	0.2	1×10^{51}	1×10^9	10^4

Table 7.3: List of Type Ia SN2025dr models and their parameters.

this SN are shown, in combination with the measured data. The graphs of M_{bol} and L_{bol} for these three models are plotted in Figure 7.18.

	$M [M_{\odot}]$	$M_{\text{Ni}} [M_{\odot}]$	$M_{\text{ime}} [M_{\odot}]$	$E_k [\text{erg}]$	$v_{\text{max}} [\text{cm s}^{-1}]$	$T [\text{K}]$
model 1	0.8	0.3	0.4	1.5×10^{51}	1×10^9	10^4
model 2	0.6	0.25	0.3	1.5×10^{51}	1×10^9	10^4
model 3	0.5	0.15	0.3	1.5×10^{51}	1×10^9	10^4
model 4	1.0	0.4	0.5	0.8×10^{51}	1×10^9	10^4
model 5	1.0	0.4	0.5	1×10^{51}	1×10^9	10^4
model 6	0.6	0.1	0.3	1×10^{51}	0.5×10^9	10^4

Table 7.4: List of Type Ia SN2025qe models and their parameters.

7.2 SNe Type Ic

We modeled the Type Ic SNe in a way quite similar to the previous Type Ia SNe, the major difficulty in this case was the significant change of the stellar parameters that led for some time to poor conversion of the calculation. However, after some effort, we could find the proper tuning of the initial state model, whose parameters are listed in Table 7.5. We finally made two models with difference only in the initial mass, $10 M_{\odot}$ and $25 M_{\odot}$, while the other parameters remain identical.

We demonstrate the synthetic light curves in a broader set of colours than in the previous models, including the UV bands Swift-UVW1, Swift-UVW2, and GALEX-NUV, which we calculated for this SN Type (and also for the following SN Type II model), in Figure 7.19. We also show the bolometric luminosity and bolometric absolute magnitude light curves for both stellar masses' models in Figure 7.20.

	$M [M_{\odot}]$	$M_{\text{Ni}} [M_{\odot}]$	$R_0 [\text{cm}]$	$E_k [\text{erg}]$	$v_{\text{max}} [\text{cm s}^{-1}]$	$T_{\text{amb}} [\text{K}]$
model 1	10	0.02	7×10^{11}	1×10^{51}	1×10^9	10^3
model 2	25	0.02	7×10^{11}	1×10^{51}	1×10^9	10^3

Table 7.5: List of SN type Ic models and their parameters.

7.2.1 SN2025oq

Figure 7.21 shows the comparison of the observed data with the two described models. Obviously, the model with the lower initial stellar mass $M = 10 M_{\odot}$ shows better agreement with observation; unless near the maximum light, where the models exhibit higher luminosity in the ZTF g -band than in the r -band. The other discrepancy occurs in the later phase, where the observed g curve does not drop as fast as the modelled one. The reason may be the remaining outer layers of helium (or even hydrogen) that produce a quasi-plateau due to some recombination wave, or, more likely, the higher amount of initially synthesized nickel.

7.2.2 SN2024aecx

The comparison plot of the observed data with synthetic light curves for this SN is shown in Figure 7.13. The modelled apparent magnitudes are in this case about 1 mag higher on average than the observed ones. The reason would again need to be carefully investigated by performing a much larger sequence of models, including various structures of the star-surrounding circumstellar medium and interstellar or intergalactic extinction.

7.3 SN Type II with circumstellar medium

SN2024vfo light curve (Figure 6.2) shows an almost constant r -magnitude for a considerable time, which could be a sign of a non-negligible amount of interstellar environment. The radiation hydrodynamic model with nonzero density of circumstellar surrounding matter had to be created in CASTRO [63] (since the SEDONA code is not capable of including the surrounding material) and then remap its results to SEDONA (see [53] for the equations and parameters related to this model).

The model parameters are set to the values of a typical red supergiant with $M_{\star} = 15 M_{\odot}$ and $R_{\star} \approx 1000 R_{\odot}$. The SN progenitor star was initially surrounded by a spherically symmetric stationary stellar wind whose parameters were determined by the expected stellar mass loss rate

$$\dot{M}_w = 10^{-6} M_{\odot} \text{ yr}^{-1}. \quad (7.6)$$

This gives the density profile of the stellar wind structure as

$$\rho_w = \frac{\dot{M}}{4\pi r^2 v_w} = \rho_{0,w} \left(\frac{R_{\star}}{r} \right)^2, \quad (7.7)$$

where r is the spherical radial distance, $\rho_w = 15 \text{ km s}^{-1}$ is the typical wind velocity of for red supergiants, and R_{\star} is the radius of the star. This implies the density of the wind at the base (at the stellar surface) as $\rho_{0,w} \approx 6.5 \times 10^{-16} \text{ g cm}^{-3}$. We also set

the initial stellar wind temperature as the radially decreasing power-law profile, $T_w = T_\star (R_\star/r)^{0.2}$, where $T_\star \approx 3300$ K is the effective temperature of the star.

We let the initial state evolve in the widely used astrophysical code CASTRO as the radiation hydrodynamical simulation, up to the ultimate time of approximately 120 days. Figures 7.23 - 7.25 demonstrate the characteristic snapshots of density, temperature, and radial velocity, respectively. The density picture at initial time of 4 days shows the surrounding profile of the stellar wind. The evolved structure at later times of 50 and 100 days shows the radiative instabilities developed around the cold dense shell of the SN expanding envelope (roughly speaking, the ring with the highest density). The use of the radiation hydrodynamical simulation (not only purely adiabatic hydrodynamics) with the result in the form of the radiation energy and its variations is necessary for the subsequent implementation of this calculation into SEDONA (otherwise the latter code would be able to calculate only the blackbody radiation solution). The resulting data from this model were subsequently remapped using the post-processing procedure built within the CASTRO code to SEDONA. Based on this model, we continued to calculate light curves for this SN Type, following the already described SEDONA procedures used for the previous models.

We will not describe here in detail the CASTRO code and its functions, since this is actually beyond the scope of this work. We only implemented the initial-state equations used for similar calculations, e.g. in [53], which we have modified to fit this model. Detailed descriptions of the physics and other implementations necessary for advanced CASTRO simulations are also provided in the paper [54].

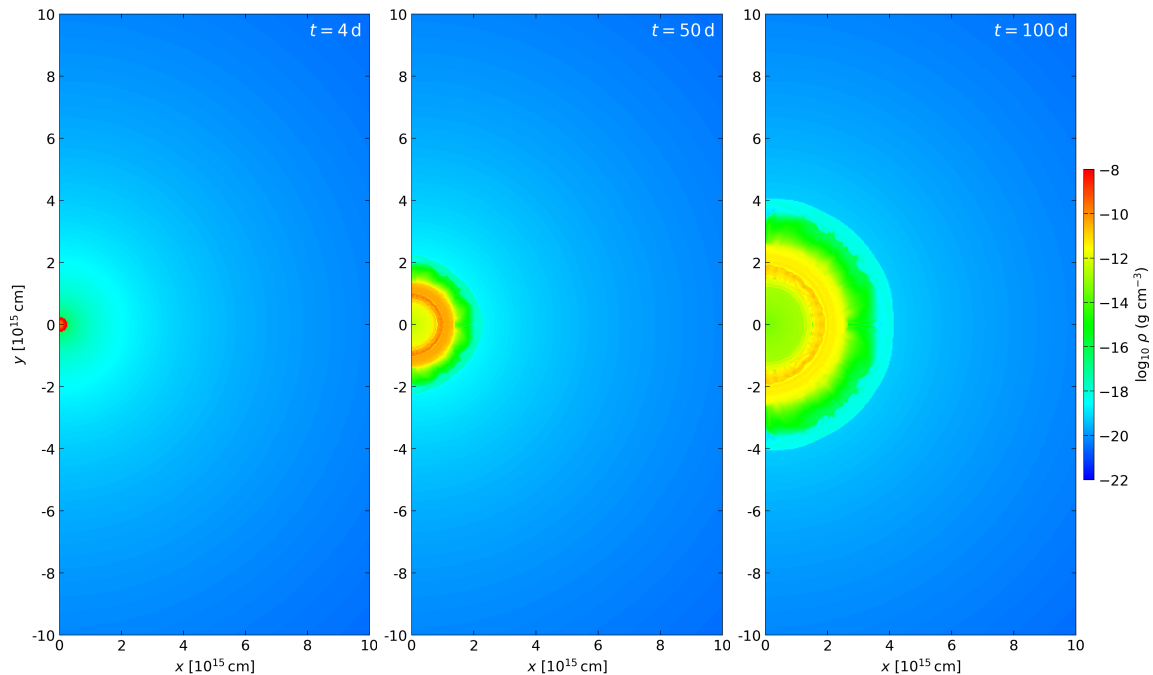


Figure 7.23: Density evolution for the SN Type II model with circumstellar medium.

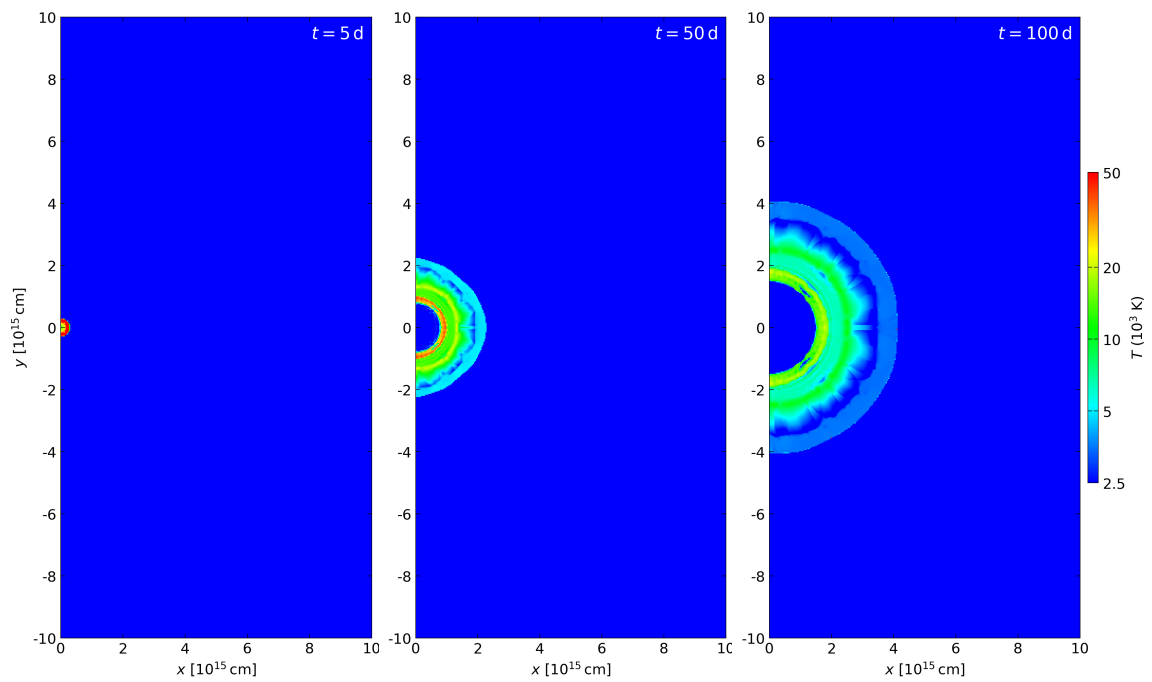


Figure 7.24: Temperature evolution for the SN Type II model with circumstellar medium.

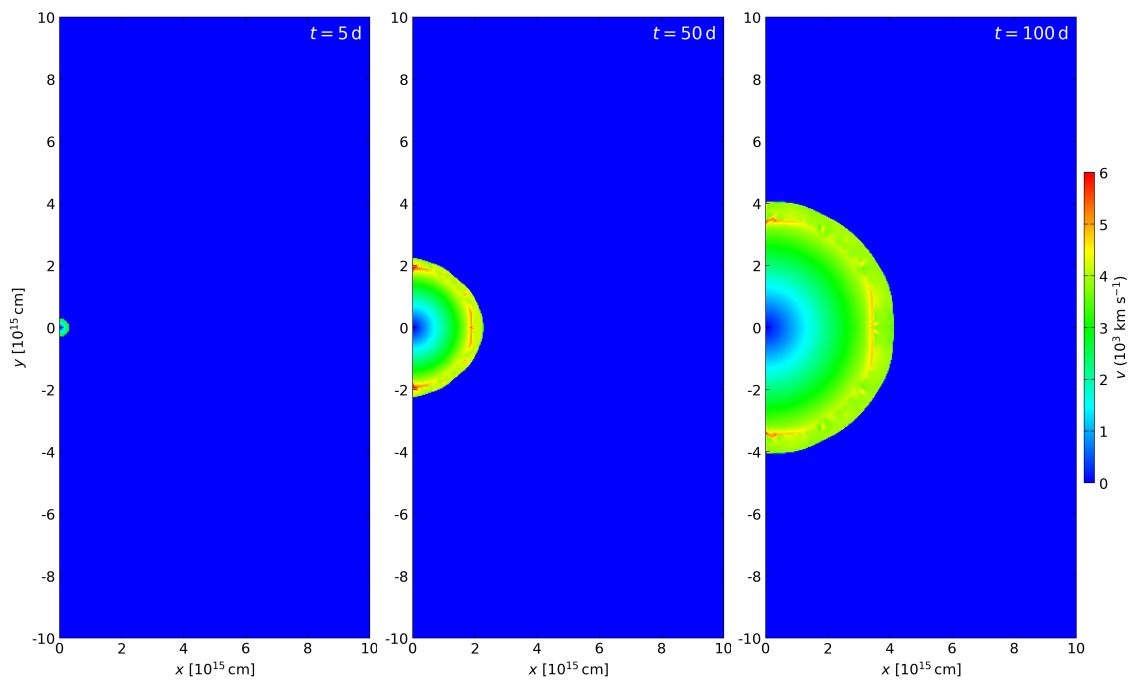


Figure 7.25: Velocity evolution for the SN Type II model with circumstellar medium.

7.3.1 SN2024vfo

We first demonstrate the results of calculation of synthetic light curves in ZTF g , r , i , Swift UVW1, Swift UVW2, and GALEX FUV bands of the SN II model with surrounding CSM in Figure 7.26. The line "shaking" is here not physical; it is due to the statistical noise associated with fewer emitted photon packets $\sim 10^4$ which is not enough for radiation transfer calculations where the radiating zone is somehow embedded in surrounding material. The reason is that the relatively optically thick surroundings transmit relatively few photons, so the resulting light curves or spectra suffer from high statistical noise. Figure 7.27 shows the bolometric luminosity and absolute bolometric magnitude calculated from the same model.

Figure 7.26 compares the observed data with the synthetic light curves calculated in SEDONA using the CASTRO model. The resulting profiles show remarkably good agreement in slopes of the g and r magnitudes; however, a frequent shift in brightness, probably due to extinctions on the way, also appears here.

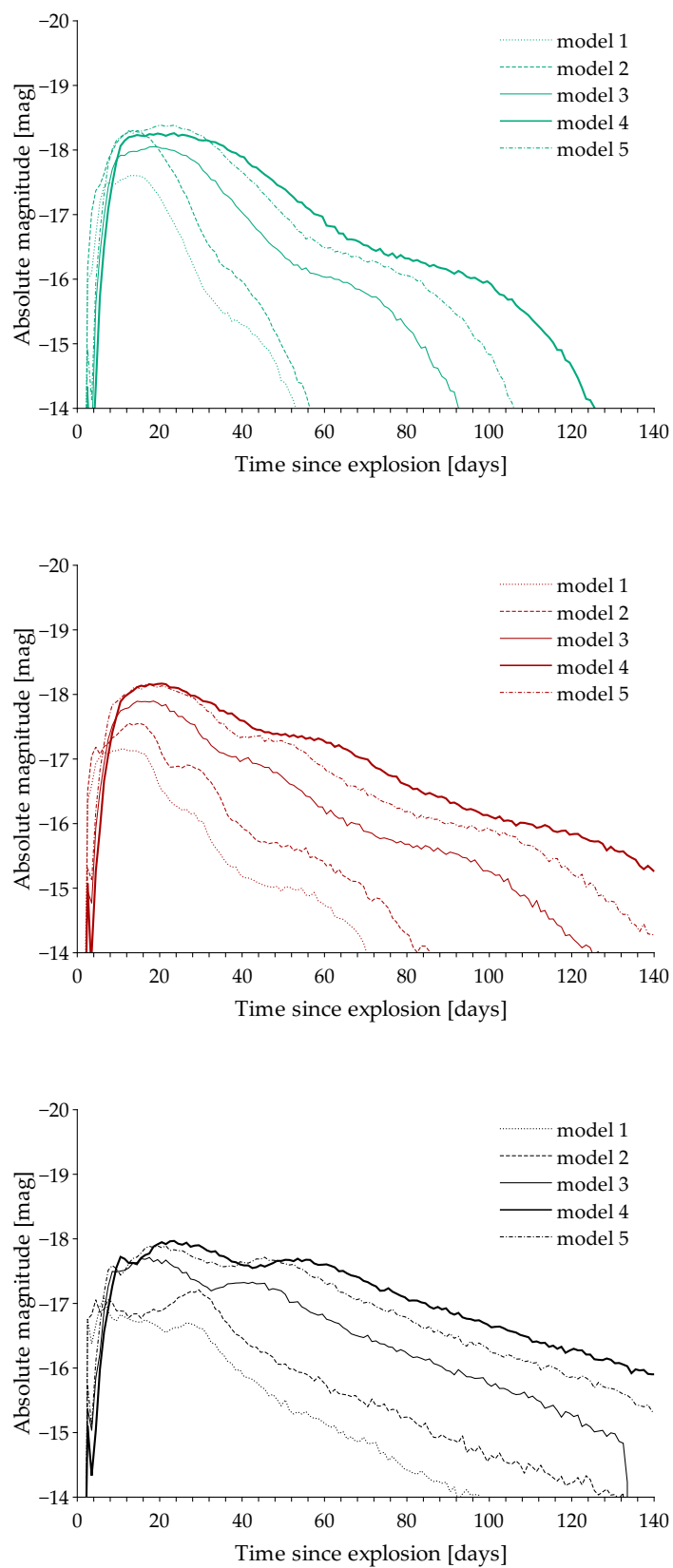


Figure 7.10: SN Type Ia model light curves in ZTF *g*, *r*, *i* filters. Model parameters are in table 7.2.

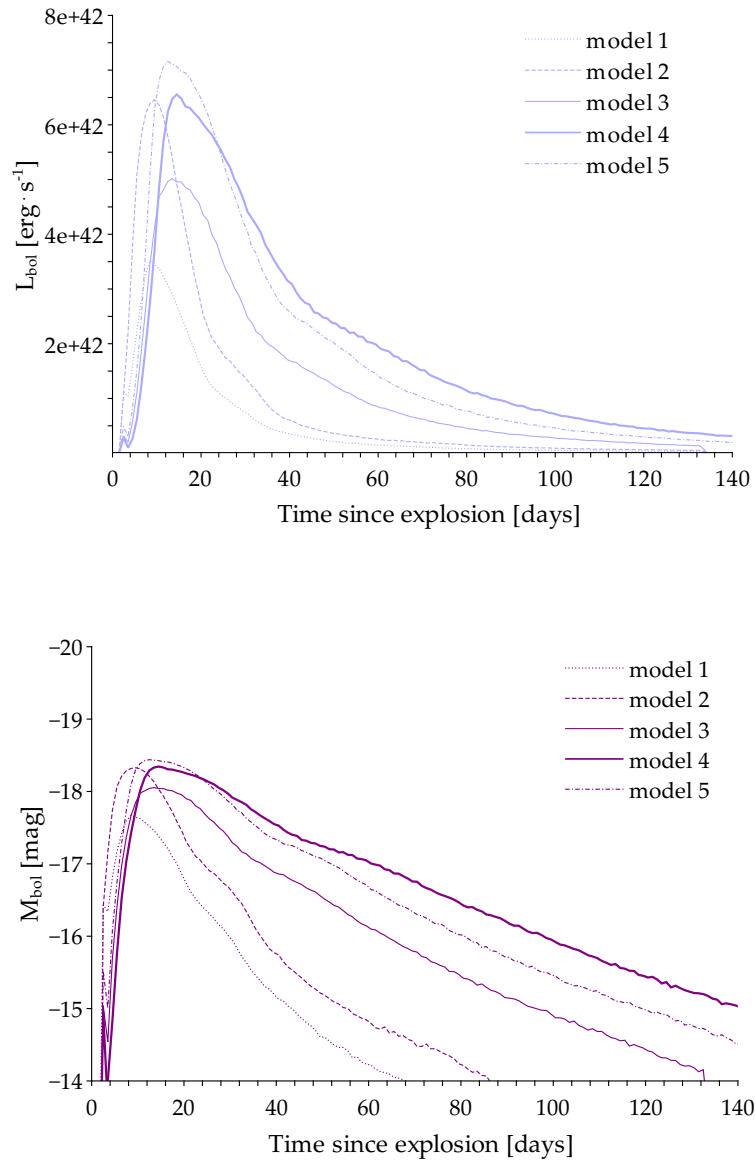


Figure 7.11: SN Type Ia model bolometric light curves. Model parameters are in the table 7.2.

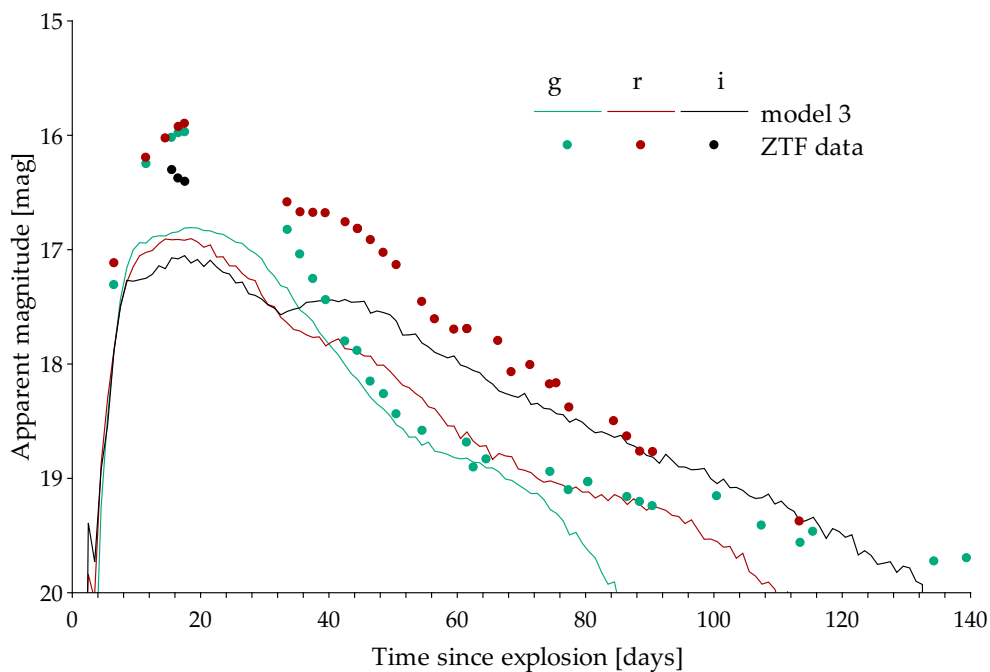


Figure 7.12: Observed data and the best model light curve for SN2024vim.

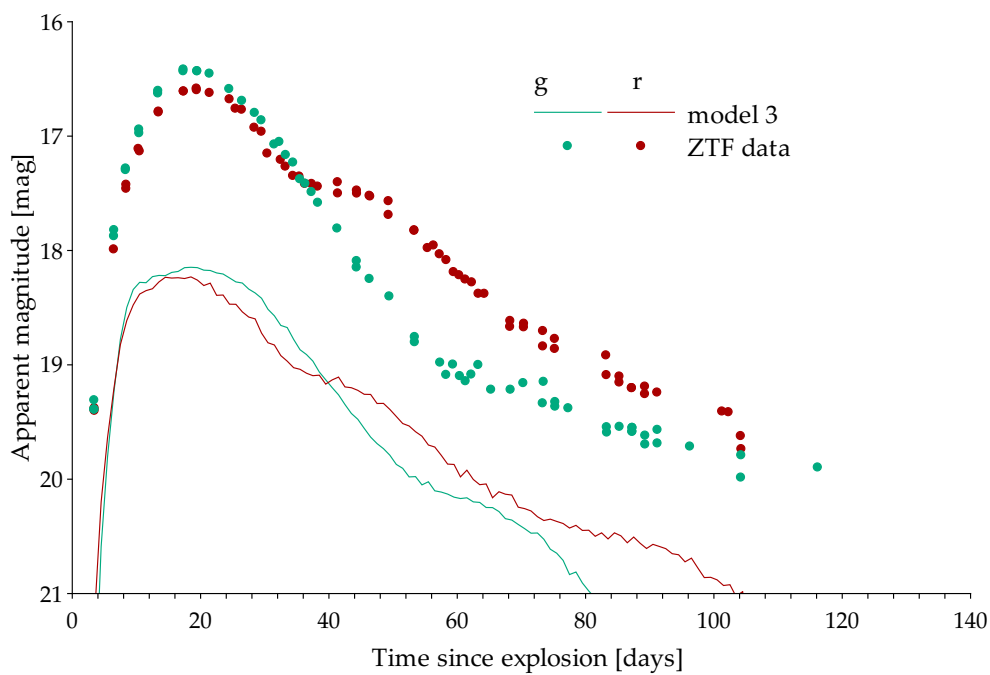


Figure 7.13: Observed data and the best model light curve for SN2024xqe.

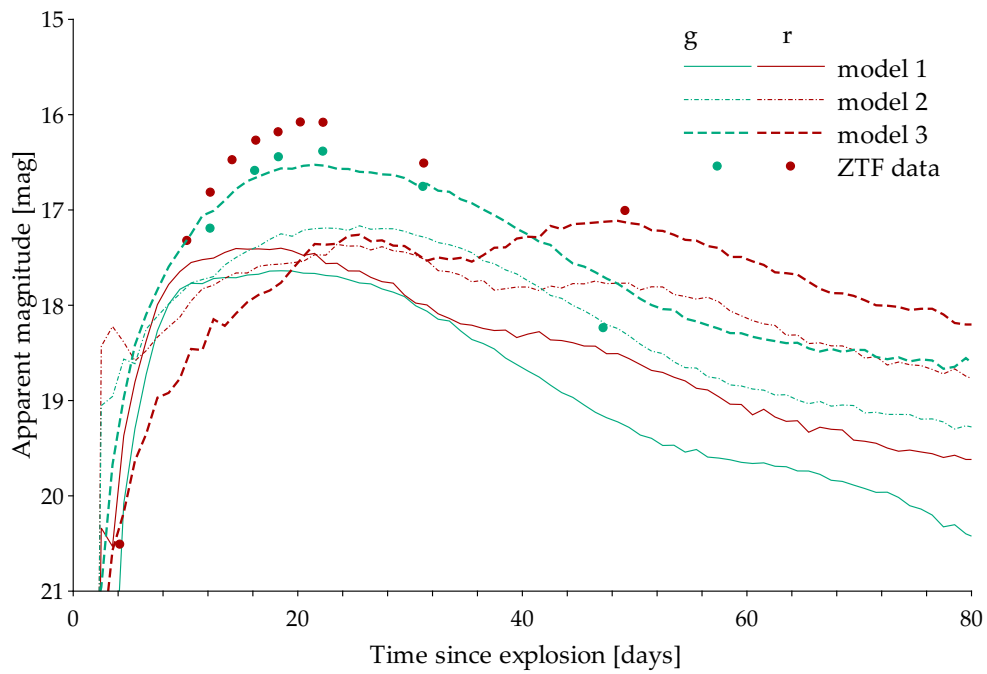


Figure 7.14: Observed and model light curves for SN2025dr.

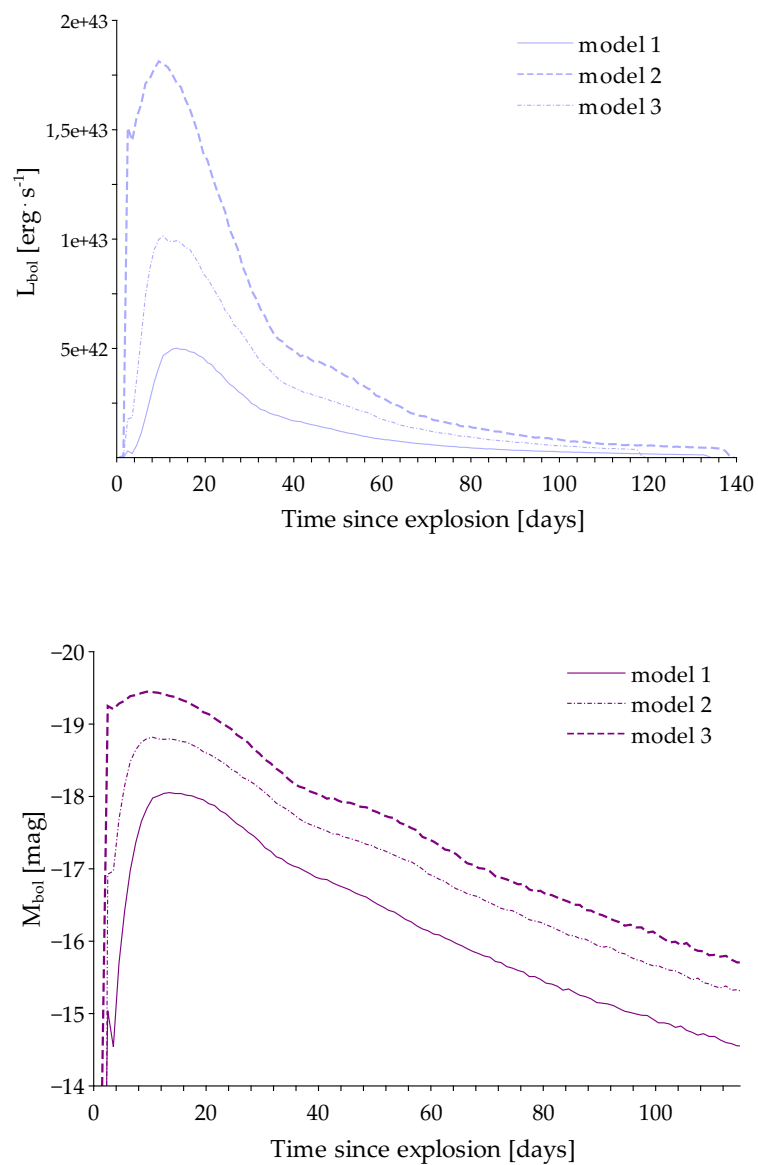


Figure 7.15: SN Type Ia model bolometric light curves for SN2025dr. Parameters are in the table 7.3.

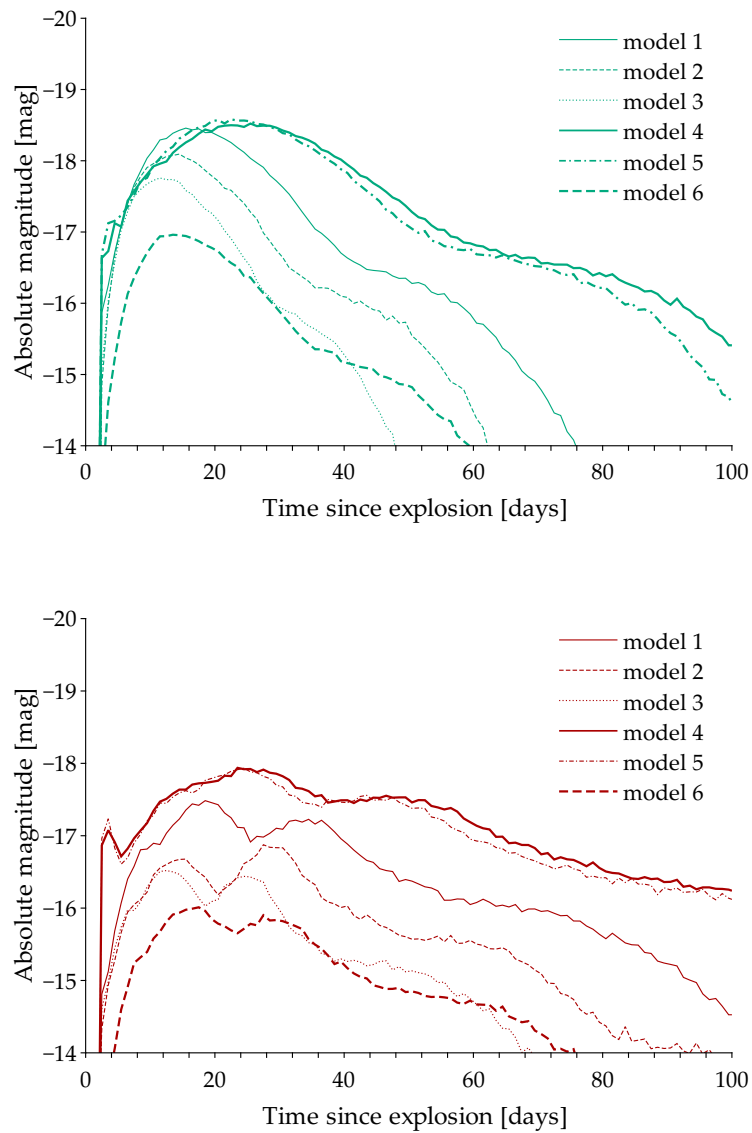


Figure 7.16: SN Type Ia model light curves in ZTF *g* and *r* filters for SN2025qe. Model parameters are in table 7.4.

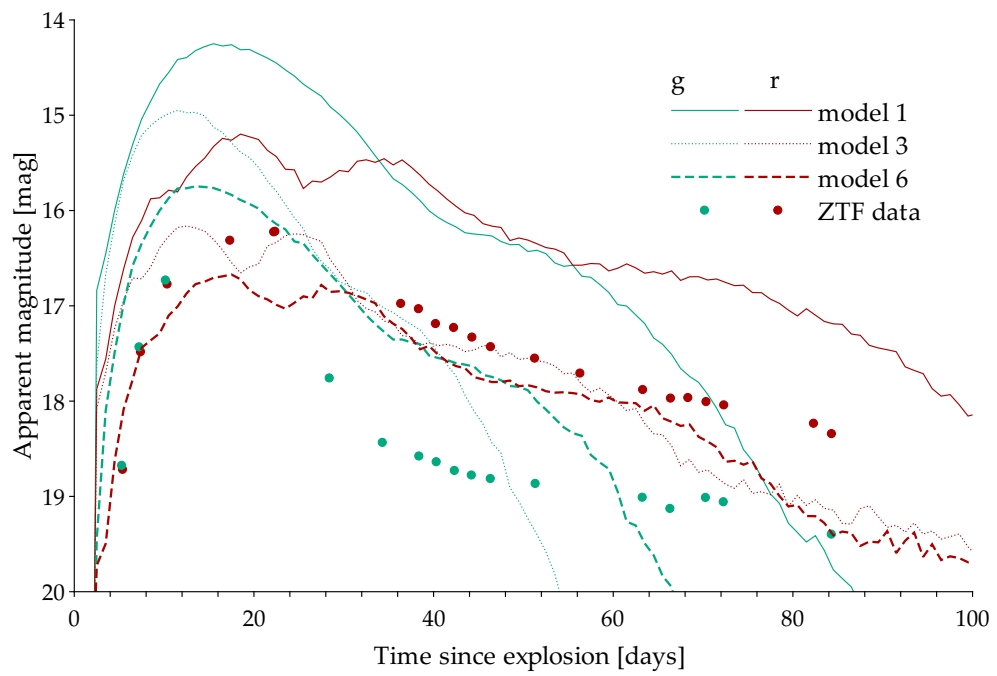


Figure 7.17: Observed and model light curves for SN2025qe.

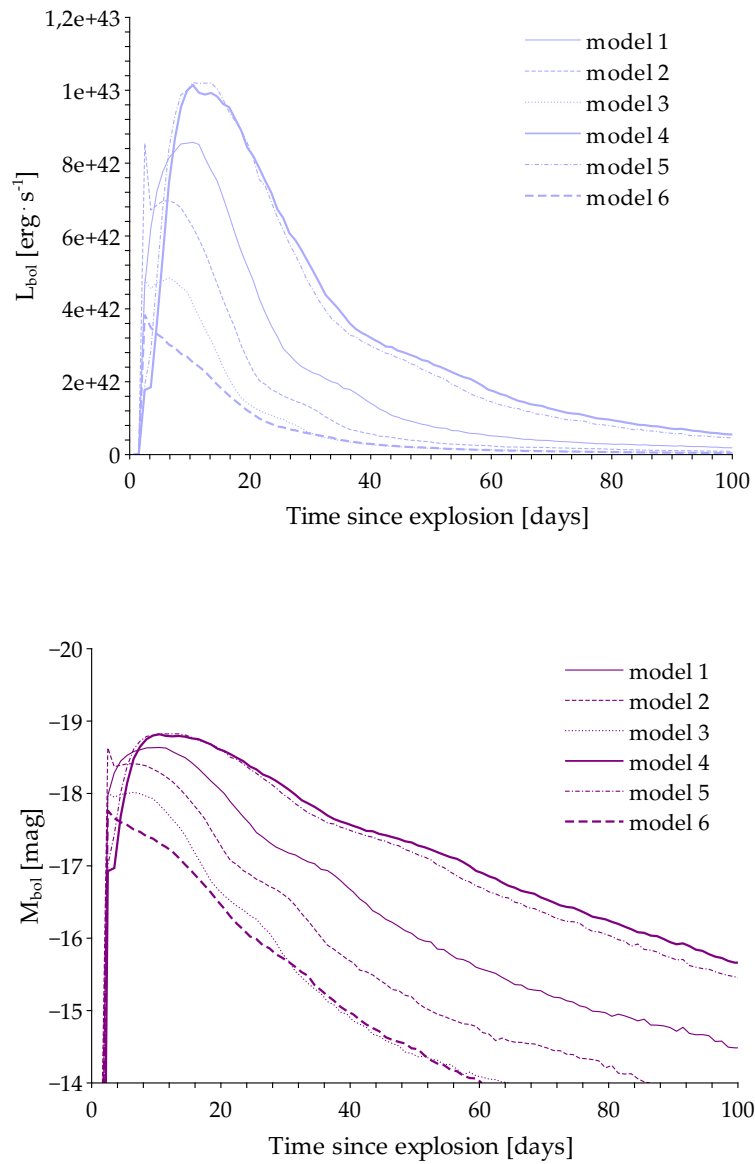


Figure 7.18: SN Type Ia model bolometric light curves for SN2025qe. Parameters are in the table 7.4.

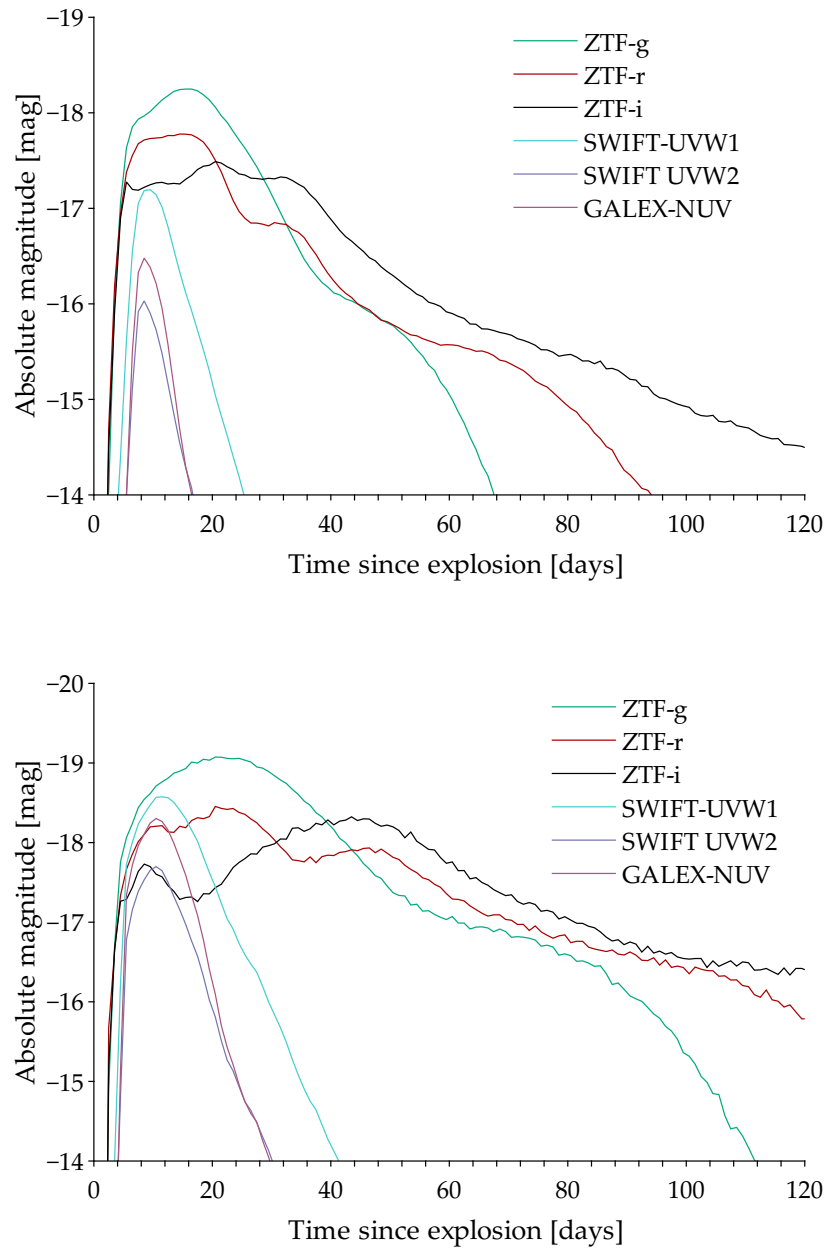


Figure 7.19: SN Type Ic model light curves in ZTF g , r , i filters and SWIFT and GALEX UV filters. Model parameters are in table 7.5.

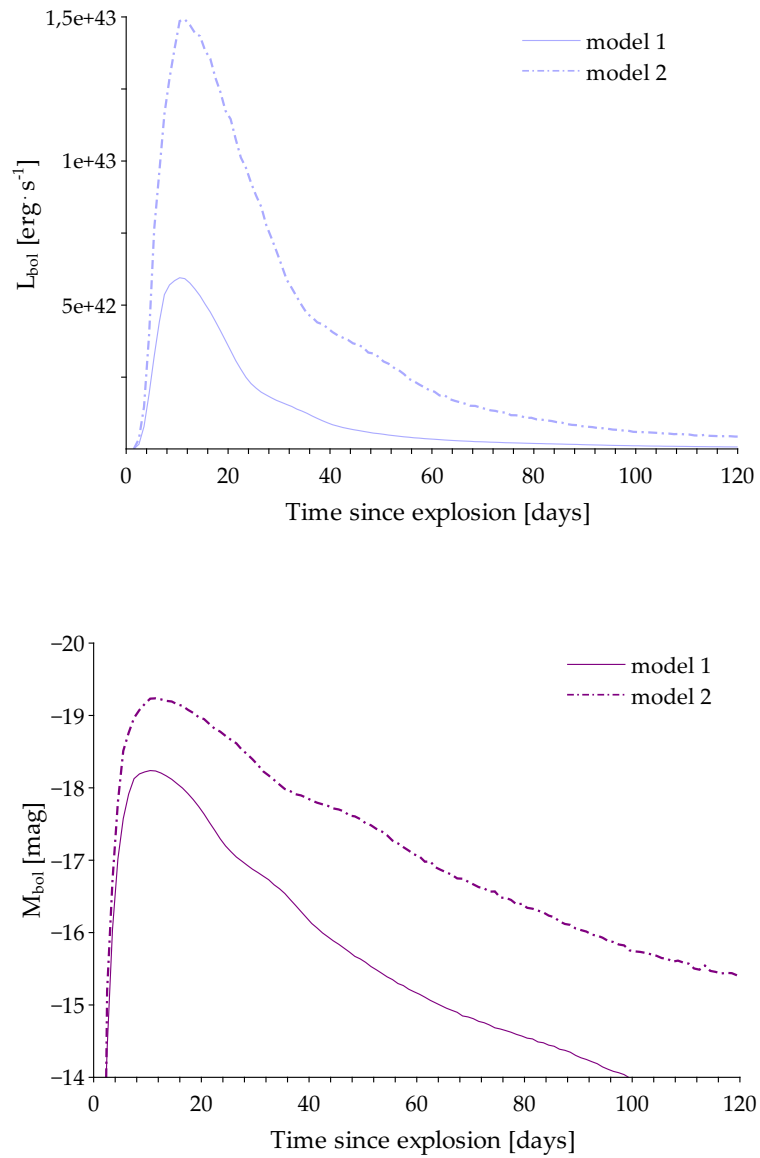


Figure 7.20: SN Type Ic model bolometric light curves. Parameters are listed in the table 7.5

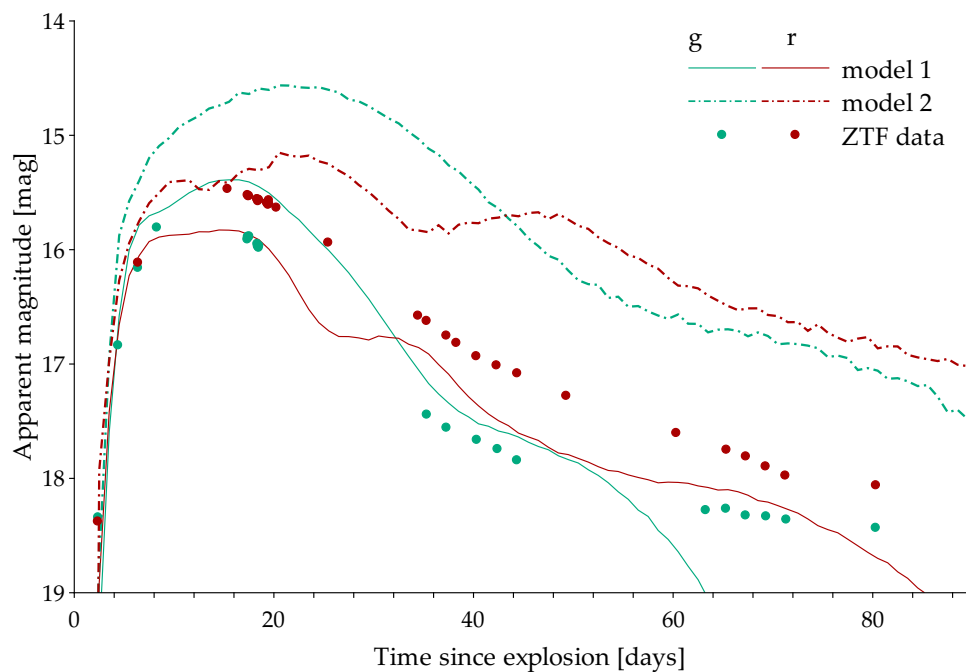


Figure 7.21: Observed data and the model light curves for SN2025oq.

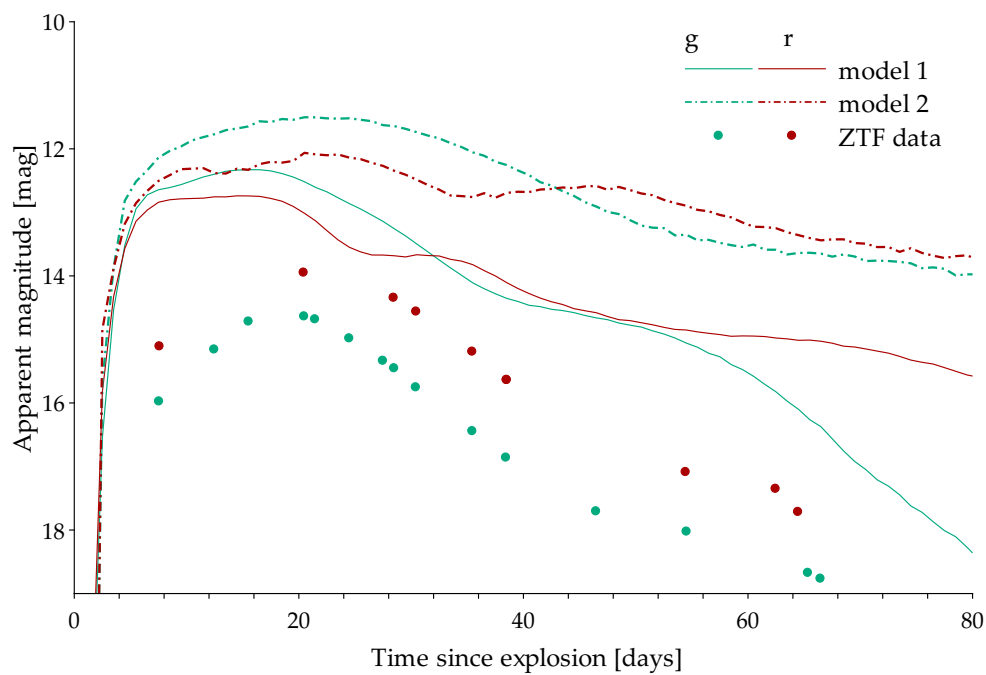


Figure 7.22: Observed data and the model light curves for SN2024aecx.

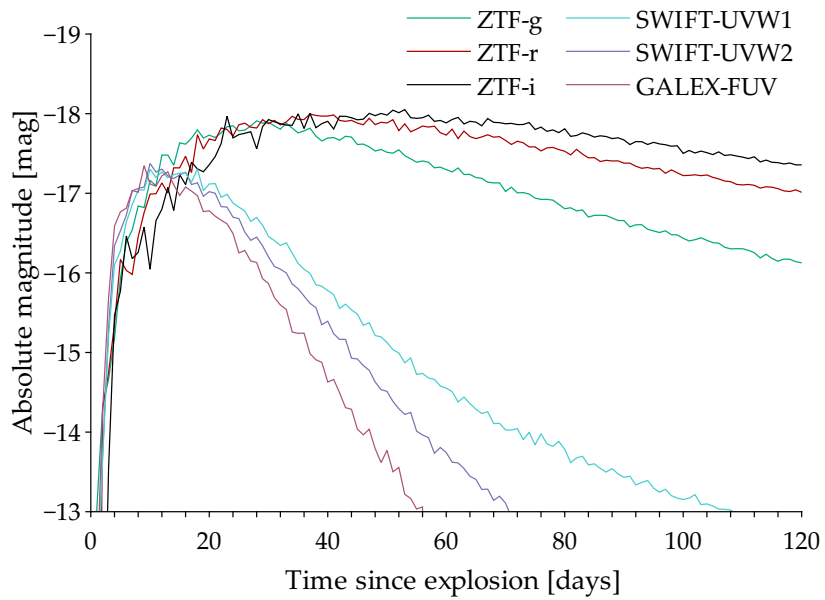


Figure 7.26: SN Type II with circumstellar medium model light curves in ZTF g , r , i filters and SWIFT and GALEX UV filters. Model parameters are described in the Section 7.3.

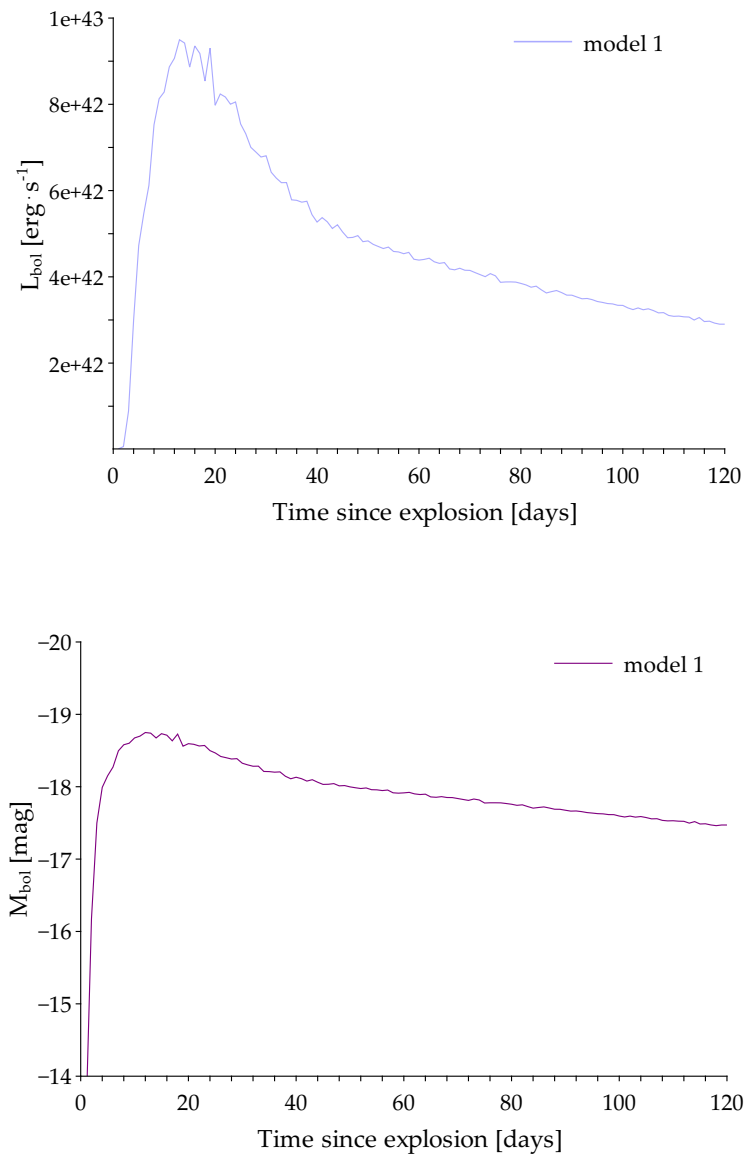


Figure 7.27: SN Type II with circumstellar medium model bolometric light curves. Model parameters are described in the Section 7.3.

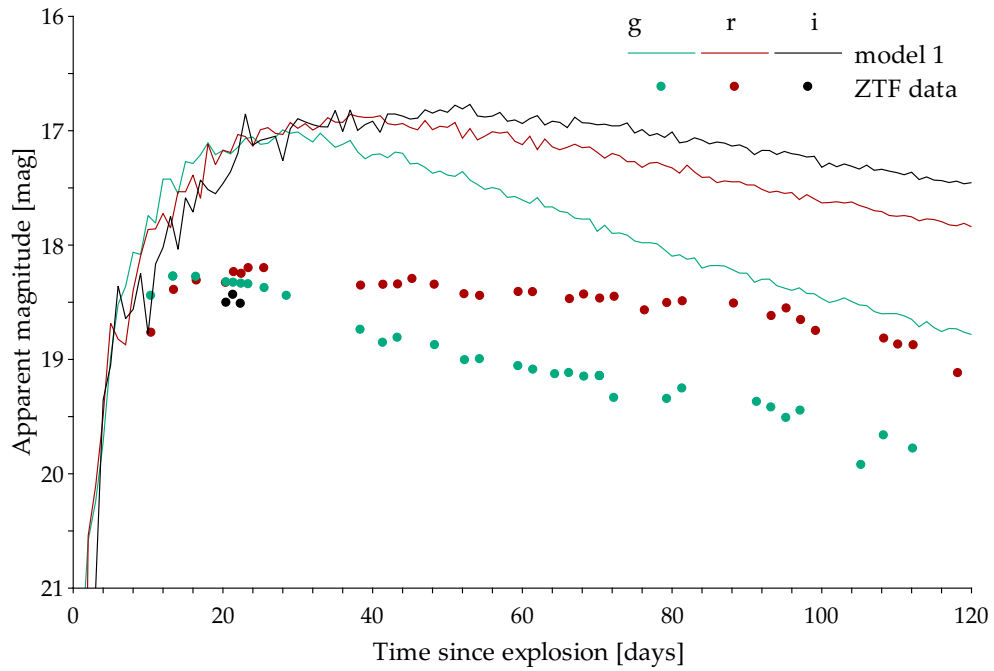


Figure 7.28: Observed data and the model light curves for SN2024vfo.

Chapter 8

Conclusions

Supernovae, multifarious subspecies of astronomical transients, are nowadays under the spotlight of many major observational surveys (e.g. ZTF, presented in chapter 4). The scientific significance of their photometric and spectroscopic measurements has important consequences and applications. For example, the use of standard SNe Ia as standard candles is essential for measuring cosmic distances (Chapter 2, Figure 2.3). Supernova nucleosynthesis is responsible for the chemical enrichment of galaxies with a multitude of heavy elements that are vital components of life as we know it.

The scientific contribution of this work is constituted by our observations of eight SNe from the turn of 2024 and 2025 (Chapter 6). The central focus of this study is presented in the final Chapter 7, wherein the outcomes of the modelling of SN light curves employing the SEDONA and CASTRO software are outlined. By comparing synthetic and observed light curves, we have obtained parameters for both the progenitor and the SN outbursts themselves. The discrepancy between the model and the observed light curves, post-accounting for the known distance of the SN, can be utilised as a metric to estimate interstellar or intergalactic extinction in its direction. This, in turn, can also provide information regarding the density of closer or more distant surroundings.

In addition to the visual part of the spectrum, we have included UV light curves in the model light curves of Type Ic and Type II SNe (Figures 7.19 and 7.26); their time course is significantly faster. Observations of the early-to-intermediate SN emission in the UV region are rare and of scientific importance. The observation of the explosion and subsequent interaction of SN and circumstellar medium (CSM) at these wavelengths can reveal valuable information regarding the explosion mechanism, its morphology and chemical composition. Observations in the UV region will facilitate the determination of the geometry and global properties of the CSM. Also the chemical composition of SN eruptions can be revealed through the use of FUV observations [59]. These and numerous other significant discoveries, not only in SN astrophysics, will be facilitated by the QUVIK space telescope. In the future, much more proper work in this field is necessary. However, the models obtained here appear to be a very good starting point to the orientation in this problematic and to set further direction in its investigation.

Chapter 9

Appendix

9.0.1 SN Ic model

Listing 9.1: Python skript, 1D model SNIc

```
import numpy as np
import h5py

#####
nx      = 100          # number of radial zones
mass    = 25.0         # mass [m_sun]
KE      = 1.0e51       # SN explosion energy [erg]
R0      = 7.e11        # progenitor radius [cm]
texp    = 5.0          # time since explosion [days]
vmax    = 1.0e9        # outer velocity [cm/s]
Mni     = 0.02         # mass of 56Ni [m_sun]
Tamb    = 1.e3         # ambient medium temperature [K]
name    = "1D_SNIc"   # name of the model
#####

# elements included
Z = [6,7,8,26,27,28]
A = [12,14,16,56,56,56]

# two stages of chemical composition
comp_ni = [ 0., 0., 0., 0., 0., 1.]
comp_C  = [0.75, 0.1, 0.15, 0., 0., 0.]

# fundamental physical_constants
pi      = 3.14159
m_sun   = 1.99e33
arad    = 7.5657e-15      # radiation constant (4*sigmaSB/c)

# pre-calculations
```

```

texp    = texp*3600.0*24  # time [s]
rmax    = vmax*texp      # initial outer ejecta radius [cm]
# progenitor escape velocity
v_e     = (KE/6/(mass*m_sun))**0.5
rho0    = mass*m_sun/8/pi/(v_e*texp)**3.0
nelems  = len(Z)        # number of elements
dv      = vmax/(1.0*nx)
# amount to reduce thermal energy by = R_ej/R0
# use R_ej ~ 3*v_e*t as rough outer edge of ejecta
adiabatic_factor = (3*v_e*texp/R0)**(-1.0)

v1d     = np.arange(dv,vmax*1.0001,dv)
t1d     = np.zeros(nx)
rho1d   = np.zeros(nx)
comp_1d = np.zeros((nx,nelems))

xx = v1d/v_e
Mime = 1.e-30
mfrac = 1 - 0.5*np.exp(-xx)*(xx**2 + 2*xx + 2)
mmid = 0.5*(Mni + Mime + Mni)/mass
mdel = Mime/mass/1.85
ximem = np.exp(-1.0*(mfrac - mmid)**6.0/mdel**6.0)

#####
# Make sedona 1D spherical model
#####

fout = open(name + "_1D.mod", "w")

rmin = 0.0
fout.write("1D_sphere standard\n")
fout.write(str(nx) + "\t" + str(rmin) + "\t"
+ str(texp) + " " + str(len(Z)) + " \n")

# write out elements
for xZ, xA in zip(Z,A):
    fout.write(str(xZ) + "." + str(xA) + " "),

# write out layer properties
for i in range(nx):
    v = (i+1.0)*dv
    vm = (i+0.5)*dv
    r = v*texp
    rho1d[i] = rho0*np.exp(-vm/v_e)
    Eth0 = 0.5*(0.5*rho1d[i]*vm**2.0)*adiabatic_factor

```

```
t1d[i] = (Eth0/arad)**0.25

line = "%10.4e %10.4e %10.4e %10.4e " %
(r,v,rho1d[i],t1d[i])

xime = ximem[i]
xni = 0
xco = 0

if (mfrac[i] < mmid):
    xni = 1 - xime
else:
    xco = 1 - xime

for j in range(nelems):
    comp_1d[i,j] = xni*comp_ni[j] + xco*comp_C[j]
    line = line + str(comp_1d[i,j]) + " "
    print(comp_C[j])
fout.write("\n")
fout.write(line)

fout.close()
```


Bibliography

- [1] ALeRCE ZTF Explorer, 2025. From: <https://alerce.science/services/ztf-explorer/> [cit. 2025-02-12].
- [2] Latest supernovae, Astronomy Section of the Rochester Academy of Sciences, David Bishop. 2025. From: <https://www.rochesterastronomy.org/supernova.html>. [cit. 2025-02-12] doi:10.1086/671483.
- [3] Jha, S.W. (2017). Type Ia Supernovae. In: Alsabti, A., Murdin, P. (eds) Handbook of Supernovae. Springer, Cham. https://doi.org/10.1007/978-3-319-20794-0_42-2
- [4] Hroch, F., Munipack. <https://munipack.physics.muni.cz/>
- [5] Townsley, D. M. & Bildsten, L. 2005, *apj*, 628, 395. doi:10.1086/430594 <https://iopscience.iop.org/article/10.1086/430594/fulltext/>
- [6] F. Paresce, R. Jedrzejewski (STScI) NASA/ESA. Online. 1994. From: <https://esahubble.org/images/opo9406c/>. [cit. 2025-04-11].
- [7] D. Kasen, R. C. Thomas, P. Nugent, *Time-dependent Monte Carlo Radiative Transfer Calculations for Three-dimensional Supernova Spectra, Light Curves, and Polarization*, *The Astrophysical Journal* **651** (2006) 366, <https://dx.doi.org/10.1086/506190>.
- [8] Kasen, D. *SEDONA Documentation*. https://dnkasen.github.io/sedona_documentation/, © 2018.
- [9] Kasen, D. *Sedona6 User Guide*. Oct 05, 2018. https://github.com/dnkasen/pubsed/blob/main/doc/Sedona6_UserGuide.pdf
- [10] Roth, N., Kasen, D., Monte Carlo radiation-hydrodynamics with implicit methods, *Astrophys. J. Suppl. Ser.* **217** (2015) 9, doi:10.1088/0067-0049/217/1/9.
- [11] K. Krisciunas, N. B. Suntzeff, P. Candia, J. Arenas, J. Espinoza, D. Gonzalez, S. Gonzalez, P. A. Höflich, A. U. Landolt, M. M. Phillips, S. Pizarro, *Optical and Infrared Photometry of the Nearby Type Ia Supernova 2001el*, *The Astronomical Journal* **125** (2003) 166–180, <https://doi.org/10.1086/344943>.

- [12] M. Stritzinger, P. A. Mazzali, J. Sollerman, S. Benetti, *Consistent estimates of Ni yields for type Ia supernovae*, *Astronomy & Astrophysics* **460** (2006) 793–798, <https://doi.org/10.1051/0004-6361:20065514>.
- [13] C. Balcon, *Transient Classification Report for 2024-09-22*, *Transient Name Server Classification Report* **2024-3653** (2024) 1, <https://ui.adsabs.harvard.edu/abs/2024TNSCR3653....1B>.
- [14] J. Johansson, S. Covarrubias, M. Chu, C. Fremling, *ZTF Transient Classification Report for 2024-10-15*, *Transient Name Server Classification Report* **2024-4026** (2024) 1, <https://ui.adsabs.harvard.edu/abs/2024TNSCR4026....1J>.
- [15] M. Pursiainen, B. Warwick, J. Lyman, D. O’Neill, K. Ackley, M. Dyer, F. Jiménez-Ibarra, K. Ulaczyk, D. Steeghs, D. Galloway, V. Dhillon, P. O’Brien, G. Ramsay, K. Noysena, R. Kotak, R. Breton, L. Nuttall, E. Pallé, D. Pollacco, T. Killestein, A. Kumar, *GOTO Transient Classification Report for 2024-12-19*, *Transient Name Server Classification Report* **2024-4975** (2024) 1, <https://ui.adsabs.harvard.edu/abs/2024TNSCR4975....1P>.
- [16] M. Pursiainen, J. Lyman, M. Magee, B. Warwick, D. O’Neill, K. Ackley, M. Dyer, F. Jiménez-Ibarra, K. Ulaczyk, D. Steeghs, D. Galloway, V. Dhillon, P. O’Brien, G. Ramsay, K. Noysena, R. Kotak, R. Breton, L. Nuttall, E. Pallé, D. Pollacco, T. Killestein, A. Kumar, *GOTO Transient Classification Report for 2025-01-20*, *Transient Name Server Classification Report* **2025-278** (2025) 1, <https://ui.adsabs.harvard.edu/abs/2025TNSCR.278....1P>.
- [17] L. Li, Q. Zhai, J. Zhang, X. Wang, *LiONS Transient Classification Report for 2025-01-19*, *Transient Name Server Classification Report* **2025-259** (2025) 1, <https://ui.adsabs.harvard.edu/abs/2025TNSCR.259....1L>.
- [18] J. Andrews, D. J. Sand, K. A. Bostroem, S. Valenti, S. Jha, M. Lundquist, E. Hoang, M. Shrestha, Y. Dong, D. Janzen, G. Hosseinzadeh, J. Pearson, N. Meza, D. Metha, A. Ravi, A. Martas, B. Subrayan, *DLT40 Transient Classification Report for 2024-12-17*, *Transient Name Server Classification Report* **2024-4943** (2024) 1, <https://ui.adsabs.harvard.edu/abs/2024TNSCR4943....1A>.
- [19] J. Andrews, K. A. Bostroem, D. J. Sand, S. Valenti, S. Jha, M. Lundquist, E. Hoang, M. Shrestha, Y. Dong, D. Janzen, G. Hosseinzadeh, J. Pearson, N. Meza, D. Metha, A. Ravi, A. Martas, B. Subrayan, *DLT40 Transient Classification Report for 2024-12-19*, *Transient Name Server Classification Report* **2024-4974** (2024) 1, <https://ui.adsabs.harvard.edu/abs/2024TNSCR4974....1A>.
- [20] R. Leadbeater, *Transient Classification Report for 2025-02-01*, *Transient Name Server Classification Report* **2025-446** (2025) 1, <https://ui.adsabs.harvard.edu/abs/2025TNSCR.446....1L>.

- [21] M. Pursiainen, D. O’Neill, B. Warwick, J. Lyman, K. Ackley, M. Dyer, F. Jiménez-Ibarra, K. Ulaczyk, D. Steeghs, D. Galloway, V. Dhillon, P. O’Brien, G. Ramsay, K. Noysena, R. Kotak, R. Breton, L. Nuttall, E. Pallé, D. Pollacco, T. Killestein, A. Kumar, *GOTO Transient Classification Report for 2025-01-19, Transient Name Server Classification Report* **2025-258** (2025) 1, <https://ui.adsabs.harvard.edu/abs/2025TNSCR.258....1P>.
- [22] M. Pursiainen, J. Lyman, B. Warwick, K. Ackley, M. Dyer, F. Jiménez-Ibarra, K. Ulaczyk, D. Steeghs, D. Galloway, V. Dhillon, P. O’Brien, G. Ramsay, K. Noysena, R. Kotak, R. Breton, L. Nuttall, E. Pallé, D. Pollacco, T. Killestein, A. Kumar, D. O’Neill, *GOTO Transient Classification Report for 2025-02-05, Transient Name Server Classification Report* **2025-504** (2025) 1, <https://ui.adsabs.harvard.edu/abs/2025TNSCR.504....1P>.
- [23] M. Andrews, J. Farah, D. A. Howell, and C. McCully, *Transient Classification Report for 2024-09-12, Transient Name Server Classification Report* **2024-3471** (2024) 1, <https://ui.adsabs.harvard.edu/abs/2024TNSCR3471....1A>.
- [24] A. Singh and J. Sollerman, *Transient Classification Report for 2024-09-13, Transient Name Server Classification Report* **2024-3488** (2024) 1, <https://ui.adsabs.harvard.edu/abs/2024TNSCR3488....1S>.
- [25] D. Kasen, *Type Ia Supernova Radiation Transport Models*, Supernovae and Gamma-Ray Bursts Conference, KITP, University of California, Santa Barbara (2007), https://www.on.kitp.ucsb.edu/online/snovae_c07/kasen/pdf/Kasen_SnovaeConf_KITP.pdf.
- [26] C.-C. Ngeow, C.-D. Lee, P.-C. Yu, F. Masci, R. Laher, T. Kupfer, V. Z. Golkhou, and on behalf of the ZTF Collaboration, *Introducing the Zwicky Transient Facility and the Be star variability program: a progress report at the National Central University*, *J. Phys.: Conf. Ser.* **1231** (2019) 012010, <https://doi.org/10.1088/1742-6596/1231/1/012010>.
- [27] R. Kurucz and B. Bell, *Atomic Line Data*, Robert Kurucz CD-ROM **23** (1995), <https://ui.adsabs.harvard.edu/abs/1995KurCD..23.....K>.
- [28] NASA/IPAC Extragalactic Database, *NED Extinction Calculator*, https://ned.ipac.caltech.edu/extinction_calculator.
- [29] Wright, E. L., *A Cosmology Calculator for the World Wide Web*, *Publications of the Astronomical Society of the Pacific*, **118** (850), 1711–1715 (2006), doi10.1086/510102, <https://www.astro.ucla.edu/~wright/CosmoCalc.html>, accessed April 2025
- [30] Vinkó, J.; Szalai, T.; Könyves-Tóth, R. *The Purport of Space Telescopes in Supernova Research*, *Universe* **2023**, 9(6), 244. doi10.3390/universe9060244

- [31] Swinburne University of Technology. *Supernova Classification*. COSMOS - The SAO Encyclopedia of Astronomy. https://astronomy.swinburne.edu.au/cosmos/*/Supernova+Classification [Accessed: 1 May 2025].
- [32] Minkowski, R., "Spectra of Supernovae", *Publications of the Astronomical Society of the Pacific*, **53**, 224 (1941), doi: [10.1086/125315](https://doi.org/10.1086/125315).
- [33] Barbon, R., Ciatti, F., & Rosino, L., "Photometric properties of type II supernovae", *Astronomy and Astrophysics*, vol. 72, no. 3, pp. 287–292, 1979. [Online]. Available: <https://adsabs.harvard.edu/full/1979A%26A....72..287B>
- [34] Filippenko, A. V., "Supernova 1987K: Type II in Youth, Type Ib in Old Age", *The Astronomical Journal*, vol. 96, pp. 1941–1950, Dec. 1988. doi:[10.1086/114940](https://doi.org/10.1086/114940). [Online]. Available: <https://ui.adsabs.harvard.edu/abs/1988AJ.....96.1941F>
- [35] Branch, D., and Wheeler, J. C., *Supernova Explosions*. Astronomy and Astrophysics Library. Springer, Berlin, Heidelberg, 2017. doi:[10.1007/978-3-662-55054-0](https://doi.org/10.1007/978-3-662-55054-0)
- [36] Gal-Yam, A., *Observational and Physical Classification of Supernovae*, in: A. Alsabti and P. Murdin (eds), *Handbook of Supernovae*, Springer International Publishing, 2017, pp. 195–237. doi:[10.1007/978-3-319-21846-5_35](https://doi.org/10.1007/978-3-319-21846-5_35)
- [37] Jha, S. W., *Type Iax Supernovae*, in: A. Alsabti and P. Murdin (eds), *Handbook of Supernovae*, Springer International Publishing, 2017, pp. 375–401. doi:[10.1007/978-3-319-21846-5_42](https://doi.org/10.1007/978-3-319-21846-5_42)
- [38] McCully, C., Jha, S. W., Scalzo, R. A., Howell, D. A., Foley, R. J., Zeng, Y., Liu, Z.-W., Hosseinzadeh, G., Bildsten, L., Riess, A. G., et al., *Still Brighter than Pre-explosion, SN 2012Z Did Not Disappear: Comparing Hubble Space Telescope Observations a Decade Apart*, *The Astrophysical Journal*, 925(2), 138, 2022. doi:[10.3847/1538-4357/ac3bbd](https://doi.org/10.3847/1538-4357/ac3bbd)
- [39] Ritter, A., Parker, Q. A., Lykou, F., Zijlstra, A. A., Guerrero, M. A., Le Dû, P., *The Remnant and Origin of the Historical Supernova 1181 AD*, *The Astrophysical Journal Letters*, 918(2), L33, 2021. doi:[10.3847/2041-8213/ac2253](https://doi.org/10.3847/2041-8213/ac2253)
- [40] Rosswog, S. and Brüggen, M., *Introduction to High-Energy Astrophysics*, Cambridge University Press, 2007. Chapter: Supernovae, p. 115. Available online: <https://wiki.ubc.ca/Course:ASTR406>
- [41] Rosswog, S. and Brüggen, M., *Introduction to High-Energy Astrophysics*, Cambridge University Press, 2007. Chapter: 7 Gamma-ray bursts , p. 243. Available online: <https://wiki.ubc.ca/Course:ASTR406>

- [42] Darnley, M. J., Ribeiro, V. A. R. M., Bode, M. F., Hounsell, R. A., and Williams, R. P., 2012, *On the Progenitors of Galactic Novae*, *The Astrophysical Journal*, 746(1), 61. <https://doi.org/10.1088/0004-637X/746/1/61>
- [43] Brau, J., 2016, *Novae, Supernovae, and the Formation of the Heavy Elements*, *Astronomy* 122, University of Oregon, <https://pages.uoregon.edu/jimbrau/astr122/Notes/Chapter21.html>.
- [44] Dutta, A., Anupama, G. C., Chakradhari, N. K., & Sahu, D. K. (2022). Can the Violent Merger of White Dwarfs Explain the Slowest Declining Type Ia Supernova SN 2011aa? *The Astrophysical Journal Letters*, **938**(2), L22. [doi:10.3847/2041-8213/ac940d](https://doi.org/10.3847/2041-8213/ac940d).
- [45] Phillips, M. M. (1993). The Absolute Magnitudes of Type IA Supernovae. *The Astrophysical Journal Letters*, **413**, L105. [doi:10.1086/186970](https://doi.org/10.1086/186970).
- [46] Wikimedia Commons. *File:Comparative supernova type light curves.png* — *Wikimedia Commons, the free media repository*, 2024. https://commons.wikimedia.org/w/index.php?title=File:Comparative_supernova_type_light_curves.png&oldid=866701537. [Online; accessed 3-May-2025].
- [47] Swinburne University of Technology. *Luminosity-Divide Rate Relation* — *COSMOS, The SAO Encyclopedia of Astronomy*, 2024. <https://astronomy.swin.edu.au/cosmos/l/luminosity-divide+rate+relation>. [Online; accessed 3-May-2025].
- [48] Arnett, W. D. *On the theory of type I supernovae*. *The Astrophysical Journal*, **230**, L37–L38 (1979). [DOI: 10.1086/182957](https://doi.org/10.1086/182957). <https://ui.adsabs.harvard.edu/abs/1979ApJ...230L..37A>
- [49] Arnett, D., & Chevalier, R. *Supernovae and Nucleosynthesis: An Investigation of the History of Matter, from the Big Bang to the Present*. *Physics Today*, **49** (1996), [doi: 10.1063/1.2807808](https://doi.org/10.1063/1.2807808).
- [50] Heger, A., Fryer, C. L., Woosley, S. E., Langer, N., & Hartmann, D. H. *How Massive Single Stars End Their Life*. *The Astrophysical Journal*, **591**(1), 288–300 (2003). [doi:10.1086/375341](https://doi.org/10.1086/375341).
arXiv: <https://arxiv.org/abs/astro-ph/0212469>.
ADS: <https://ui.adsabs.harvard.edu/abs/2003ApJ...591..288H>.
- [51] Mikulášek, Z., & Krtička, J. *Základy fyziky hvězd*. Masarykova univerzita, Brno, 2005. <https://astro.physics.muni.cz/download/documents/skripta/F3080.pdf>.

- [52] Kurfürst, P. *Astrofyzika supernov*. Diplomová práce. Brno: Masarykova univerzita, Přírodovědecká fakulta, 2010. Dostupné z: <https://theses.cz/id/4iabwh/>.
- [53] Kurfürst, P., Pejcha, O., and Krtička, J., *Supernova explosions interacting with aspherical circumstellar material: implications for light curves, spectral line profiles, and polarization*, *Astronomy & Astrophysics*, **642**, A214 (2020), doi:10.1051/0004-6361/202039073, <https://ui.adsabs.harvard.edu/abs/2020A&A...642A.214K>.
- [54] Kurfürst, P., Zajaček, M., Werner, N., Krtička, J., *Red giant - jet collisions in galactic nuclei I: 3D hydrodynamical model of a few stellar orbits*, arXiv, 2024, <https://ui.adsabs.harvard.edu/abs/2024arXiv240917773K>.
- [55] NASA/CXC/SAO. *Tycho Supernova Remnant Image*. Image credit: NASA/CXC/SAO. https://www.nasa.gov/wp-content/uploads/2023/03/tycho_1.jpg [Accessed: 3 May 2025].
- [56] NASA, ESA, CSA, STScI, D. Milisavljevic (Purdue University), T. Temim (Princeton University), I. De Looze (University of Gent). *Webb Image of Supernova Remnant*. Release date: 11 December 2023. <https://esawebb.org/images/weic2330e/> [Accessed: 3 May 2025].
- [57] Mobeen, M. Z., Kamiński, T., Matter, A., Wittkowski, M., & Paladini, C. *The mid-infrared environment of the stellar merger remnant V838 Monocerotis*. *Astronomy & Astrophysics*, **655**, A100 (2021). doi:10.1051/0004-6361/202142297. <https://ui.adsabs.harvard.edu/abs/2021A&A...655A.100M>.
- [58] NASA and the Hubble Heritage Team (AURA/STScI). *V838 Monocerotis*. NASA Science. <https://science.nasa.gov/image-detail/idl-tiff-file-42/>.
- [59] Werner, N., Řípa, J., Thöne, C., Münz, F., Kurfürst, P., Jelínek, M., Hroch, F., Benáček, J., Topinka, M., Lukes-Gerakopoulos, G., Zajaček, M., Labaj, M., Prišegen, M., Krtička, J., Merc, J., Pál, A., Pejcha, O., Dániel, V., Jon, J., Šošovička, R., Gromeš, J., Václavík, J., Steiger, L., Segiňák, J., Behar, E., Tarem, S., Salh, J., Reich, O., Ben-Ami, S., Barschke, M. F., Berge, D., Tohuvavohu, A., Sivanandam, S., Bulla, M., Popov, S., & Chang, H.-K. *Science with a Small Two-Band UV-Photometry Mission III: Active Galactic Nuclei and Nuclear Transients*, (2024). <https://arxiv.org/abs/2306.15080>.

- [60] Krtička, J., Benáček, J., Budaj, J., Korčáková, D., Pál, A., Piecka, M., Zejda, M., Bakış, V., Brož, M., Chang, H.-K., Faltová, N., Gális, R., Jadlovní, D., Janík, J., Kára, J., Kolář, J., Krtičková, I., Kubát, J., Kubátová, B., Kurfürst, P., Labaj, M., Merc, J., Mikulášek, Z., Münz, F., Paunzen, E., Prišegen, M., Ramezani, T., Rievajová, T., Řípa, J., Schmidtobreick, L., Skarka, M., Szász, G., Weiss, W., Zajaček, M., Werner, N.,
Science with a Small Two-Band UV-Photometry Mission II: Observations of Stars and Stellar Systems, (2024).
<https://ui.adsabs.harvard.edu/abs/2024SSRv...220...24K>.
- [61] Zajaček, M., Czerny, B., Jaiswal, V. K., Štolc, M., Karas, V., Pandey, A., Pasham, D. R., Śniegowska, M., Witzany, V., Suková, P., Münz, F., Werner, N., Řípa, J., Merc, J., Labaj, M., Kurfürst, P., Krtička, J.,
Science with a small two-band UV-photometry mission III: Mission description and follow-up observations of stellar transients, (2024).
<https://ui.adsabs.harvard.edu/abs/2024SSRv...220...29Z>.
- [62] Vintrová, Petra. *QUVIK – první český vesmírný dalekohled*. Online. 2024. Dostupné z: <https://quvik.cz/> [cit. 2025-05-03].
- [63] Almgren, A. S., Beckner, V. E., Bell, J. B., Day, M. S., Howell, L. H., et al.,
CASTRO: A New Compressible Astrophysical Solver. I. Hydrodynamics and Self-gravity, (2010).
<https://ui.adsabs.harvard.edu/abs/2010ApJ...715.1221A>.
- [64] Metzger, B. D.
Kilonovae. *Living Reviews in Relativity*, **23**, 1 (2020).
<https://doi.org/10.1007/s41114-019-0024-0>.
- [65] Abbott, B. P., et al.
Multi-messenger Observations of a Binary Neutron Star Merger. *The Astrophysical Journal Letters*, **848**, L12 (2017).
<https://ui.adsabs.harvard.edu/abs/2017ApJ...848L..12A>.
- [66] Palomar Observatory / Caltech. The 48-inch (1.2-meter) Samuel Oschin Telescope. Online: <https://sites.astro.caltech.edu/palomar/about/telescopes/oschin.html>. [Accessed: 2 May 2025].
- [67] Bellm, E. C., Kulkarni, S. R., Graham, M. J., Dekany, R., Smith, R. M., Riddle, R., Masci, F. J., Helou, G., Prince, T. A., Adams, S. M., et al. (2019). The Zwicky Transient Facility: System Overview, Performance, and First Results. *Publications of the Astronomical Society of the Pacific*, **131**(995), 018002. [doi:10.1088/1538-3873/aaecbe](https://doi.org/10.1088/1538-3873/aaecbe).

- [68] Planck Collaboration, Ade, P. A. R., Aghanim, N., Arnaud, M., Ashdown, M., Aumont, J., Baccigalupi, C., Banday, A. J., Barreiro, R. B., Bartlett, J. G., Bartolo, N., *et al.*, *Planck2015 results: XIII. Cosmological parameters*, *Astronomy & Astrophysics*, **594**, A13 (2016). DOI: [10.1051/0004-6361/201525830](https://doi.org/10.1051/0004-6361/201525830).
- [69] Fitzpatrick, E. L., *Correcting for the Effects of Interstellar Extinction*, *Publications of the Astronomical Society of the Pacific*, **111**(755), 63–75 (1999). DOI: [10.1086/316293](https://doi.org/10.1086/316293).
- [70] Indebetouw, R., Mathis, J. S., Babler, B. L., Meade, M. R., Watson, C., Whitney, B. A., Wolff, M. J., Wolfire, M. G., Cohen, M., Bania, T. M., *et al.* The Wavelength Dependence of Interstellar Extinction from 1.25 to 8.0 μm Using GLIMPSE Data. *Astrophysical Journal*, **619**(2), 931–938 (2005). doi:[10.1086/426679](https://doi.org/10.1086/426679).
- [71] Foley, R. J., Challis, P. J., Chornock, R., Ganeshalingam, M., Li, W., Marion, G. H., Morrell, N. I., Pignata, G., Stritzinger, M. D., Silverman, J. M., *et al.* Type Iax Supernovae: A New Class of Stellar Explosion. *Astrophysical Journal*, **767**(1), 57 (2013). doi:[10.1088/0004-637X/767/1/57](https://doi.org/10.1088/0004-637X/767/1/57).
- [72] Magee, M. R., Kotak, R., Sim, S. A., Kromer, M., Rabinowitz, D., Smartt, S. J., Baltay, C., Campbell, H. C., Chen, T.-W., Fink, M., *et al.* The type Iax supernova, SN 2015H: A white dwarf deflagration candidate. *Astronomy & Astrophysics*, **589**, A89 (2016). doi:[10.1051/0004-6361/201528036](https://doi.org/10.1051/0004-6361/201528036).
- [73] Stritzinger, M. D., Valenti, S., Hoeflich, P., Baron, E., Phillips, M. M., Taddia, F., Foley, R. J., Hsiao, E. Y., Jha, S. W., McCully, C., *et al.* Comprehensive observations of the bright and energetic Type Iax SN 2012Z: Interpretation as a Chandrasekhar mass white dwarf explosion. *Astronomy & Astrophysics*, **573**, A2 (2014). doi:[10.1051/0004-6361/201424168](https://doi.org/10.1051/0004-6361/201424168).
- [74] McCully, C., Jha, S. W., Foley, R. J., Bildsten, L., Fong, W., Kirshner, R. P., Marion, G. H., Riess, A. G., Stritzinger, M. D. A luminous, blue progenitor system for the type Iax supernova 2012Z. *Nature*, **512**(7512), 54–56 (2014). doi:[10.1038/nature13615](https://doi.org/10.1038/nature13615).
- [75] McCully, C., Jha, S. W., Foley, R. J., Chornock, R., Holtzman, J. A., Balam, D. D., Branch, D., Filippenko, A. V., Frieman, J., Fynbo, J., *et al.* Hubble Space Telescope and ground-based observations of the Type Iax supernovae SN 2005hk and SN 2008A. *The Astrophysical Journal*, **786**(2), 134 (2014). doi:[10.1088/0004-637X/786/2/134](https://doi.org/10.1088/0004-637X/786/2/134).
- [76] González-Gaitán, S., Hsiao, E. Y., Pignata, G., Förster, F., Gutiérrez, C. P., Bufano, F., Galbany, L., Folatelli, G., Phillips, M. M., Hamuy, M., *et al.* Defining photometric peculiar Type Ia supernovae. *The Astrophysical Journal*, **795**(2), 142 (2014). doi:[10.1088/0004-637x/795/2/142](https://doi.org/10.1088/0004-637x/795/2/142).

- [77] McClelland, C. M., Garnavich, P. M., Galbany, L., Miquel, R., Filippenko, A. V., Bassett, B., Wheeler, J. C., Goobar, A., Jha, S. W., Sako, M., et al. The subluminous supernova 2007qd: A missing link in a family of low-luminosity Type Ia supernovae. *The Astrophysical Journal*, **720**(1), 704–716 (2010). doi:10.1088/0004-637x/720/1/704.
- [78] Milne, P. A., Brown, P. J., Roming, P. W. A., Holland, S. T., Immler, S., Filippenko, A. V., Ganeshalingam, M., Li, W., Stritzinger, M., Phillips, M. M., et al. Near-ultraviolet properties of a large sample of Type Ia supernovae as observed with the *Swift* UVOT. *The Astrophysical Journal*, **721**(2), 1627–1655 (2010). doi:10.1088/0004-637x/721/2/1627.
- [79] Kawash, A., Mróz, P., Kochanek, C. S., Shappee, B. J., Holoiien, T. W.-S., Stanek, K. Z., Britt, C. T., Vallely, P. J., Coppejans, D. L., Sokolovsky, K. V., et al. The Galactic Nova Rate: Estimates from the ASAS-SN and Gaia Surveys. *The Astrophysical Journal*, **933**, 184 (2022). <https://arxiv.org/abs/2206.14132>
- [80] Rector, T. A., Shafter, A. W., Schweizer, F., Henze, M., Bode, M. F., Hornoch, K., Ciardullo, R., Darnley, M. J., Galbany, L., Neill, J. D., et al. The Rate and Spatial Distribution of Novae in M31 as Determined by a Twenty-Year Survey. *The Astrophysical Journal*, **937**, 78 (2022). <https://arxiv.org/abs/2207.05689>
- [81] Scalzo, J., Wheeler, J. C. Astrophysical and Astrobiological Implications of Gamma-Ray Burst Properties. *The Astrophysical Journal*, **566**, 723–737 (2002). <https://arxiv.org/abs/astro-ph/9912564>
- [82] Blondin, S., Tonry, J. L. Determining the type, redshift, and age of a supernova spectrum. *The Astrophysical Journal*, **666**(2), 1024–1047 (2007). doi:10.1086/520494.

